POLITECNICO DI TORINO

Department of Mechanical and Aerospace Engineering (DIMEAS)

Politecnico di Torino

Master's Degree in Aerospace Engineering

Design of the Propulsion System for a Pressurized Lunar Rover

Supervisors:

Dr. Giuseppe Palaia
Dr. Rodolfo Azzara
Prof. Matteo Filippi

Candidate:

Elia Girodo

April 2026

Contents

List of Figures

List of Tables

List of Acronyms

AFC	Alkaline Fuel Cell
AM0	Air Mass Zero
AWG	American Wire Gauge
BED	Battery Energy Density (gravimetric)
BHJ	Bulk Heterojunction
BMS	Battery Management System
BOL	Begin-of-Life
BP	Bipolar Plates
CIC	Cell Interconnect Coverglass
CL	Catalyst Layer
CSA	Canadian Space Agency
DEC	Diethyl Carbonate
DMC	Dimethyl Carbonate
DP	Double Polarization
EC	Ethylene Carbonate
ECLSS	Environmental Control and Life Support System
ECM	Equivalent Circuit Model
EFBs	Embedded Function Blocks
EOL	End-of-Life
ESA	European Space Agency
EVA	Extravehicular Activity
FA	Fullerene Acceptor
GDL	Gas Diffusion Layer
GFC	Gas Flow Channels
GPHS-RTG	General Purpose Heat Source Radioisotope Thermoelectric Generator
HPs	Heat Pipes

ISRU	In-Situ Resource Utilization
ISS	International Space Station
IVA	Intravehicular Activity
JAXA	Japan Aerospace Exploration Agency
LFMP	Lithium-Iron-Manganese-Phosphate
LFP	Lithium-Iron-Phosphate Battery
LHPs	Loop Heat Pipes
LIB	Lithium-Ion Battery
LMB	Lithium Metal Battery
MCFC	Molten Carbonate Fuel Cell
MEA	Membrane-Electrode Assembly
MEG	Multiple Exciton Generation
MEM	Meteoroid Engineering Model
MHW-RTG	Multi-Hundred Watt Radioisotope Thermoelectric Generator
MIB	Magnesium-Ion Battery
MJSC	Multi-Junction Solar Cell
MLI	Multilayer Insulation
MMOD	Micrometeoroid and Orbital Debris
MMRTG	Multi-Mission Radioisotope Thermoelectric Generator
MPF	Mass Packing Factor
MPP	Maximum Power Point
MPPT	Maximum Power Point Tracker
NASA	National Aeronautics and Space Administration
NFA	Non-Fullerene Acceptor
NIR	Near-Infrared
OCV	Open Circuit Voltage
OSC	Organic Solar Cell
PAFC	Phosphoric Acid Fuel Cell
PCMs	Phase Change Materials
PD	Partial Discharge

PEM	Proton Exchange Membrane
PEMFC	Proton Exchange Membrane Fuel Cell
PEO	Polyethylene Oxide
PLC	Piecewise Linear Circuit
PSC	Perovskite Solar Cell
PV	Photovoltaic
QDs	Quantum Dots
ROSA	Roll-Out Solar Array
RTG	Radioisotope Thermoelectric Generator
SDM	Single-Diode Model
SEI	Solid Electrolyte Interphase
SIB	Sodium-Ion Battery
SOA	Safe Operating Area
SOC	State of Charge
SOFC	Solid Oxide Fuel Cell
SoH	State of Health
SSB	Solid State Battery
SVD	Single Void Discharge

List of Symbols

Symbol	Name	Units
A	Shepherd exponential zone amplitude constant	V
A_c	Conductor cross-sectional area	cm^2
A_i	Insulator layer area	cm^2
A_s	Sheath layer area	cm^2
A_{pack}	Battery pack exponential zone amplitude constant (Shepherd model)	V
A_{active}	Solar array active area	m^2
A_{array}	Effective solar array area	m^2
$A_{surf,pack}$	Battery pack surface area	m^2
A_{surf}	Battery cell surface area	m^2
B	Shepherd inverse exponential zone time constant	Ah^{-1}
B_{pack}	Battery pack inverse exponential zone time constant (Shepherd model)	Ah^{-1}
Bi	Biot number	-
C	Cable sizing constant (SVD method)	cm
C_p	Specific heat capacity	J/(kg·K)
C_{case}	C-rate case	-
C_{ref}	Reference C-rate	-
C_{th}	Thermal capacitance	J/K
E_0	Shepherd open-circuit voltage	V
E_r	Required battery pack energy	Wh
$E_{0_{pack}}$	Battery pack open-circuit voltage (Shepherd model)	V
I_0	Reverse saturation current of the diode	A
I_m	Maximum power current	A
I_{pv}	Photocurrent	A
K	Shepherd polarisation constant or polarisation resistance	Ω or V/Ah
K_d	Solar cell lifetime degradation factor	-
K_s	Void shape factor	-
K_t	Solar cell temperature coefficient	-
K_{ill}	Solar cell illumination coefficient	-
K_{pack}	Battery pack polarization constant (Shepherd model)	Ω or V/Ah
L	Total cable length	m
PF	Solar array packing factor	-
P_0	Theoretical specific power output of the solar cell	W/m^2
P_0	Actual specific power output of the solar cell	W/m^2

$P_{delivered}$	Delivered battery power	W
P_{loss}	Battery power losses	W
P_r	Required power	W
P_{useful}	Battery useful power	W
Q	Battery cell capacity	Ah
Q_d	Total heat dissipation	W
Q_g	Total generated heat	W
Q_r	Required battery pack capacity	Ah
Q_{conv}	Total convective heat	W
Q_{eff}	Effective battery capacity	Ah
Q_{exp}	Capacity at end of exponential zone	Ah
Q_{irr}	Irreversible heat	W
Q_{nom}	Capacity at end of nominal zone	Ah
Q_{rad}	Total radiative heat	W
Q_{rev}	Reversible heat	W
Q_{tot}	Total heat accumulated	W
R	Internal resistance	Ω
R_c	Contact resistance	Ω
R_s	Series resistance	Ω
R_{sh}	Shunt resistance	Ω
R_{pack}	Battery pack internal resistance (Shepherd model)	Ω
SOC_t	State of charge target	%
SOC_{lim}	State of charge limit	%
T_r	Rover surface temperature	K
T_{amb}	Ambient temperature	K
T_{int}	Internal temperature	K
T_{op}	Solar array operating temperature	K
$T_{ref,b}$	Battery cell reference temperature	K
$T_{ref,c}$	Solar cell reference temperature	K
T_{surf}	Surface temperature	K
U	Battery cell equilibrium potential	V
V_T	Solar cell thermal voltage	V
V_m	Maximum power voltage	V
V'_m	Minimum discharge inception voltage	V
V_p	Peak voltage	V
V_{bay}	Rover subsystem bay volume	m^3
V_{bus}	Bus voltage	V
V_{cell}	Battery cell voltage	V
V_{exp}	Voltage at end of exponential zone	V
V_{full}	Battery cell maximum charge voltage	V

V_{max}	Maximum voltage	V
V_{nom}	Battery cell nominal voltage	V
W_b	Battery cell mass	kg
W_{cell}	Solar array cell mass	kg
W_{pack}	Battery pack mass	kg
Δt	Integration step	s
α	Sun angle	deg
α_v	Minimum breakdown voltage of air	V
$\bar{m}_i$	Insulator mass per unit length	kg/m
$\bar{m}_s$	Sheath mass per unit length	kg/m
η_g	Powertrain efficiency	%
η_{cell}	Solar cell efficiency	%
$\eta_{converter}$	Converter efficiency	%
η_{el}	Battery electrical efficiency	%
$\eta_{inverter}$	Inverter efficiency	%
η_{motor}	Electric motor efficiency	%
κ	Thermal conductivity	W/(m·K)
π	Pi constant	-
ρ	Battery cell material density	kg/m^3
ρ_c	Cable conductor density	kg/m^3
ρ_i	Cable insulator density	kg/m^3
ρ_s	Cable sheath density	kg/m^3
σ_{SB}	Stefan-Boltzmann constant	W/(m^2·K^4)
τ	Time constant of the first-order filter	s
ε	Surface emissivity	%
ε_b	Solar array back surface emissivity	%
ε_f	Solar array front surface emissivity	%
a	Solar cell ideality factor	-
a_r	Absorptance of the rover external layer	%
a_t	Absorptance of the solar cell	%
d_c	Conductor diameter	cm
d_s	Battery cell diameter	m
$degr$	Solar cell degradation rate per year	%
h	Battery pack height	m
h_c	Convective heat transfer coefficient	W/(m^2·K)
h_s	Battery cell length	m
i	Battery current	A
i^*	Filtered current	A
i_s	Current for Shepherd model parameters extraction	A
it	Actual battery charge	Ah

k_B	Boltzmann constant	J/K
l	Battery pack length	m
m	Battery modules in parallel	-
m_c	Conductor mass per unit length	kg/m
m_{cable}	Cable total mass per unit length	kg/m
m_{cell}	Battery cell mass	kg
n_s	Battery pack cells in series	-
p_k	Peukert's coefficient	-
q_d	Total heat dissipation flux	W/m^2
q_g	Internal heat generation flux	W/m^2
q_{conv}	Convective heat flux	W/m^2
q_{rad}	Radiative heat flux	W/m^2
r_c	Cable conductor radius	m
t	Time	s
t_i	Cable insulation thickness	m
t_r	Operating time	s
t_s	Cable sheath thickness	m
tot_{cells}	Total battery pack cells number	-
w	Battery pack width	m
y	Rover lifetime	years

Abstract

This thesis, carried out within the Space It Up! program, focuses on the development of physics-based models for the sizing of the propulsion system of a pressurized lunar rover. The topics addressed begin with an in-depth study of the state of the art of batteries, solar cells, fuel cells, and more complex technologies such as Radioisotope Thermal Generators, also providing an outlook on the future of these technologies by highlighting expected progress, not only in terms of performance, but also from a sustainability perspective. A general overview of the lunar environment, in which the rover will operate, is presented together with possible technological solutions to the documented critical issues of this environment.

The discussion then proceeds with a detailed study of battery based propulsion, identifying a mathematical model to simulate the physics of the propulsion system from both electrical and thermal perspectives, validating the obtained results with experimental references available in the literature. The presence of solar arrays as an additional on-board energy source for the pressurized lunar rover is also modeled. The results account for power train losses, environmental conditions, and intrinsic losses of the technologies.

This work provides a preliminary assessment tool for the study of a battery based lunar pressurized rover, offering considerations on advantages and disadvantages depending on the operational profile, and opening the way for future developments to further deepen the addressed topics and extend the evaluation to more propulsion solutions.

1 Introduction

Space exploration has its roots in the improvement of Galileo Galilei's telescope, through which he was the first to conduct systematic astronomical observations in 1609, providing strong support to the heliocentric model previously proposed by Nicolaus Copernicus. From that moment onward, the universe began to be regarded as an observable physical system rather than an abstract philosophical construct. Building on Tycho Brahe's data, Johannes Kepler formulated the laws of planetary motion, later physically explained by Isaac Newton through the law of universal gravitation, establishing the foundations of classical and celestial mechanics.

The possibility of reaching space emerged with Konstantin Tsiolkovsky's rocket equation (1903), which defined the principles of propulsion and highlighted the importance of mass ratio and exhaust velocity. Further developments by Walter Hohmann and Hermann Oberth identified efficient orbital transfer strategies. However, the desire to directly explore this new environment was reached only in 1957 with the launch of the first artificial satellites and, later, with the Apollo 11 mission in 1969, which saw the first human setting foot on the Moon, becoming a milestone in the history of astronautics.

At the end of the Apollo program, National Aeronautics and Space Administration (NASA) began searching for a reusable system capable of providing access to space while reducing launch costs. This objective was pursued through the development of the Space Shuttle, completing its first orbital flight in 1981.

With the end of the Cold War, the global aerospace scenario experienced a significant transformation characterized by the cooperation of several space agencies such as NASA, Roscosmos, European Space Agency (ESA), Japan Aerospace Exploration Agency (JAXA), and Canadian Space Agency (CSA) in the realization of the International Space Station. Building on the operational experience gained through the Shuttle-Mir program, the launch of the first International Space Station (ISS) module in 1998 marked a turning point for human presence in orbit.

Today, this legacy evolves: the exploration of deep space and the establishment of permanent habitats on the Moon and Mars represent the most complex technological frontier of the modern era. In this scenario, robotic mobility serves as an essential precursor to human expansion. The Soviet Union inaugurated mobile exploration with the Lunokhod program. Lunokhod 1, which landed on the Moon in November 1970 aboard the Luna 17 probe, was the first remote-controlled robot to move on another celestial body, introducing fundamental engineering solutions for modern rover design [51]. However, as scientific objectives extended toward the outer Solar System, the technical legacy of Lunokhod had to undergo a transition toward a design that accounts for operation in hostile environments without constant supervision, leading to the development of autonomous navigation systems and subsystem compartmentalization [51].

Subsystems represent a division of functionalities within rovers, which are highly interconnected and mutually dependent. To operate, a power source is required to be appropriately converted into the desired energy type (such as mechanical, thermal and electrical) via the power subsystem.

The power subsystem relies on diverse energy architectures, managed according to the mission's environmental constraints. Chemical energy conversion, typically achieved through electrochemical redox reactions in batteries or fuel cells, remains a primary method for providing high power density. While both technologies share similar physical principles, fuel cells differ in their external management of reactants (fuel and oxidant). This mechanism has been widely exploited for a long time through the use of batteries with various chemical compositions from nickel to lithium. Solar radiation can also be exploited via the photovoltaic effect, generating current by inducing charge separation within semiconductor materials, thereby removing depen-

dency on sources directly stored within the rover and reducing weight and volume; batteries and solar arrays are extensively used in various space missions, powering satellites and exploratory rovers both on the Moon and Mars, such as the Mars Exploration Rovers (Spirit and Opportunity) or the Sojourner.

More advanced solutions are represented by Radioisotope Thermoelectric Generators (RTGs), which convert the decay heat of radioisotopes into electricity via the Seebeck effect, as demonstrated in several missions such as Curiosity, Perseverance and the Voyager probes. More advanced studies have already confirmed the feasibility of using nuclear fission reactors, though they face substantial challenges regarding radiation shielding and international regulatory frameworks for space nuclear power sources.

The importance of on-board energy source regeneration is a crucial theme, given the lack of a supply chain like that on Earth; therefore, various ways to use the extraterrestrial environment to one's advantage are being studied, such as In-Situ Resource Utilization (ISRU) and space mining, retrieving necessary elements from the soil and atmosphere. Selecting the correct architecture is driven by requirements such as power in Watts, energy expressed in Watt-hours to quantify power delivery duration, gravimetric and volumetric densities, and the constraints introduced by the typical operational characteristics of each solution. These include the management of byproducts (such as heat or reaction waste), the necessity of shielding components from radioactive sources, or the fact that some solutions inherently require high-power operation, making them unsuitable for direct scaling to low-power applications.

From these perspectives, batteries offer high energy density, resulting in more compact applications and high efficiency; however, they fall short in terms of reusability, being limited to non-rechargeable primary batteries or secondary batteries with a finite lifespan that must be coupled with power generation systems like solar arrays. Fuel cells are characterized by higher power densities (or energy density when considering external tanks), offering the possibility of regenerative solutions to cover both eclipse and daylight periods. They essentially operate like an engine at high efficiency (not being limited by the Carnot cycle efficiency), but are better suited for high-power missions, requiring a larger total volume compared to batteries for low-power needs, though they become more advantageous for extended durations of use.

Solar arrays are an excellent resource, enabling the realization of lightweight and compact systems; they serve as the primary power generation source for most inner-planet missions, though they necessitate secondary energy storage (batteries) to sustain operations during eclipse periods or dust storms; the downside lies in their total dependence on the Sun and constant exposure to environmental agents making them excellent as a secondary or backup energy source for high-power missions.

For long-duration missions, RTGs represent an exceptional resource, ensuring independence from external energy sources for years and allowing exploration in regions with little to no illumination. However, they suffer from severely limited system-level power density and low efficiency, requiring numerous additional components for overall management.

The deployment of pressurized rovers further complicates mission planning by introducing additional subsystems such as the Environmental Control and Life Support System (ECLSS) and Extravehicular Activity (EVA) support, enabling exit and entry operations. Consequently, the power requirements increase significantly, and the design of the rover must account for the presence of the crew in addition to overall efficiency, ensuring sufficient levels of redundancy to enhance safety and reliability. In the future, programs such as ARTEMIS foresee human exploration of the Lunar and Martian surfaces. In this scenario, it will be crucial to establish permanent or semi-permanent lunar bases as hubs for multi-day excursions and to exploit ISRU to sustain long-term operations.

1.1 Objectives

The objective of this thesis is to develop a parametric model of the propulsion system of a pressurized lunar rover, investigating currently adopted solutions and future advancements, based on a battery pack supported by solar arrays. The advantages and disadvantages of the investigated solution will therefore be evaluated by proposing mathematical models at both the electrical and thermal levels in order to predict the achievable performance, also in view of technological advancements, while considering the impacts of the lunar environment, in particular from significant temperature variations and illumination conditions. The proposed models will be validated by comparing the obtained results with experimental data available in the literature, and will subsequently be used in several proposed mission scenarios to assess the feasibility of specific missions by varying the input parameters. Specifically, the steps of the thesis are:

- Research on the state of the art, identifying both established and next-generation technologies;
- Define the mission requirements, ambient constraints, and specifications of the propulsion system;
- Identification of the most suitable electric and thermal models, and their validation;
- Sizing and simulation of the candidate propulsion architectures in different configurations;
- Simulate realistic mission scenarios, highlighting the advantages and limitations introduced by the power sources.

1.2 Thesis overview

This thesis is organized into five chapters.

Chapter 1 introduces the problem by providing an extensive overview of the state of the art, establishing the basis for understanding the underlying physical principles, along with the current performance of such solutions, and offering considerations on the expected technological advancements. Particular attention is devoted to battery technologies and photovoltaic cells.

Chapter 2 describes the operational environment of the rover, addressing the various challenges to be considered during the design phase. It also proposes technological solutions to mitigate the adverse effects of such conditions on the subsystems, with particular emphasis on the propulsion system.

Chapter 3 focuses on the methodologies adopted to model the electrical and thermal behavior of batteries and solar arrays. In particular, the Shepherd model is thoroughly discussed, including an extension to the battery pack level and its validation. This is followed by a discussion on cable selection using the Single Void Discharge (SVD) method and the associated losses along the power train. The thermal modelling evaluates the impact of ambient temperature on electrical parameters and introduces a cell-level 0D thermal model to quantify heat generation and temperature evolution, which is subsequently validated and extended to the battery pack. This enables the identification of operating conditions that ensure optimal electro-thermal performance. A solar cell model, based on the Single-Diode Method (SDM), is then presented

to evaluate cell performance and scaled to an array configuration, exploring different operating conditions and quantifying associated losses.

Chapter 4 presents the overall architecture of the propulsion system, defining different operational phases that are analysed individually. Subsequently, two sizing scenarios are introduced to determine the required technical specifications, ensuring compliance with environmental constraints and the adopted models.

Chapter 5 presents the validation of the adopted methodology, highlighting the results obtained and how the proposed objectives have been achieved. A brief section is also included, providing indications on how to further develop this tool to make it more comprehensive and suitable for broader assessments of propulsion system choices.

1.3 State of the art

This section presents the relevant information regarding the various state of the art design options currently available for powering lunar rovers. Particular attention will be given to the mission requirements and operational constraints, due to the presence of a crew and the challenges of operating in the lunar environment. All of this information is essential for identifying, in the following chapters, the most advantageous configurations to consider in the design of the propulsion system. The most significant studies on the development of pressurized rovers are reported in Table 1.1.

Table 1.1: Pressurized rovers from literature.

Model	Crew	Mass [ton]	Range [km]	Power [kW]	Propulsion
MOLAB [51]	2	4.3	80	8.7	Fuel cell and solar arrays
Lunar Sortie Vehicle [11]	6			3.5	Radioisotope Thermal Generator
Pressurized Lunar Rover [7]	4	7	2000	8.5	Dynamic Isotope Power System
Mars Pressurized Rover [51]	2	16.5	500	10	Dynamic Isotope Power System
Daylight Rover [51]	2	25	1000	10	Regenerative Fuel Cells
Lunar Polar Mission Rover [51]	3	6.08	100	6	Fuel Cells
Habot [11]	6	10		100-300	Solar arrays and Follower Nuclear Reactor Rover / Space Solar Power Satellite

Following the identification of the candidate propulsion technologies, each technology is examined individually to assess its most advantageous characteristics and to compare them with one another.

1.3.1 Batteries

The use of batteries as the main energy source is the simplest to implement, requiring few additional components, typically having low costs, being lightweight, and demanding minimal maintenance. A battery pack consists of multiple cells connected in series or parallel. Within each cell, a redox reaction takes place and it is possible to identify three main components: the anode, which is the negative electrode where oxidation occurs, the cathode, which is the positive electrode where reduction occurs and the electrolyte, typically a liquid, which acts as the conductor allowing the transfer of ions between the electrodes as illustrated in Figure 1.1.

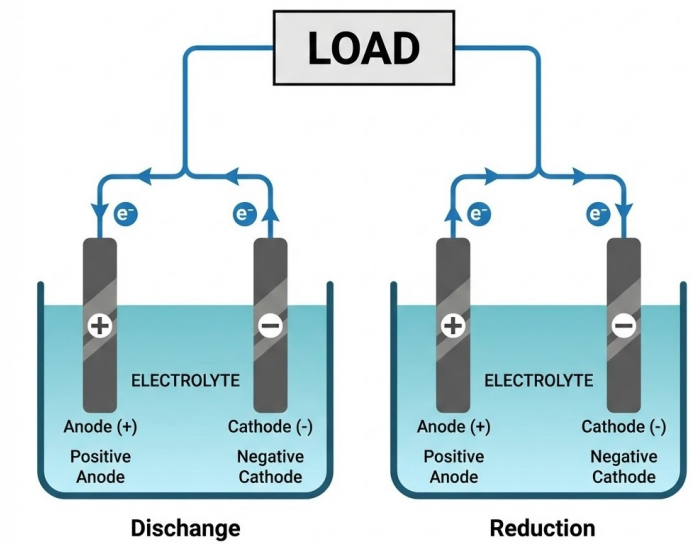

Figure 1.1: Cell working principle.

The materials for the electrodes are chosen based on their lightness and the highest achievable voltage and capacity. The standard potential (or theoretical voltage expressed in V) of the cell is determined by the type of active material and is measured experimentally. The theoretical capacity, on the other hand, is determined by the amount of active material in the cell and, measured in Ah, represents the total quantity of electricity produced by the reaction per unit of time. The theoretical energy produced by the cell is the product of the standard potential and the theoretical capacity, measured in (Wh); only a fraction of this energy is usable due to internal losses. When the energy density (Wh/kg) is evaluated, the components that do not participate in the reaction must be considered, as they also impact the overall mass and cost of the battery. Batteries (or cells) can be divided into three main categories:

- **Primary:** non-rechargeable, low-cost, lightweight, with a good storage life and high energy density at low discharge rates. Those are commonly used in everyday life, primary batteries are small, single-cell cylindrical cans (AAA-D size) and flat button batteries [28];
- **Secondary:** rechargeable by circulating current in the opposite direction of discharge; they act as accumulators and are typically connected to and kept charged by a primary energy source, delivering energy to the load to supplement the main power system; they can also serve as the main energy source in case power demands exceed the capacity of a primary battery or where life cycle costs are favorable compared to primary cells [28];

- **Reserve:** these are essentially primary batteries, but with separated active components, which will irreversibly interact when power delivery is required, effectively eliminating self-discharge and allowing long-term storage. The reserve battery designs replace both primary and secondary cells where extreme environments or prolonged storage are encountered, such as in missiles, torpedoes, and other weapon systems [28].

In general, the theoretical energy density of a primary cell does not exceed $1500\,Wh/kg$ [28] but, the practical specific energy delivered under optimal discharge conditions is significantly lower and usually does not exceed $600\,Wh/kg$ [28]. Rechargeable systems are more negatively impacted than primary batteries, due to the restricted set of electrode materials that can sustain efficient reversible electrochemical reactions and the need for designs to facilitate recharging and cycle life [28].

The main losses within the cells are due to polarization effects, which occur when a load current i, accompanying the electrochemical reactions, flows through the electrodes. These losses include (1) activation polarization, which drives the electrochemical reaction at the electrode surface, and (2) concentration polarization, which arises from the concentration differences of the reactants and products at the electrode surface and within the volume of the electrolyte and the electrode, as a result of mass transfer [28]. The internal impedance of the cell (a measure of resistance to electrical current flow) is another important factor that strongly affects performance causing a voltage drop during operation, which also consumes part of the useful energy as waste heat. The total internal impedance of a cell is the sum of the ionic resistance of the electrolyte (within the separator and the porous electrodes); the electronic resistances of the active mass, the current collectors and electrical tabs of both electrodes; and the contact resistance between the active mass and the current collector. These are ohmic resistances, following Ohm's law, with a linear relationship between current and voltage drop [28].

Cells typically operate in a range from $1\,V$ to $5V$ and must therefore be connected in series to provide the necessary voltage and in parallel to provide sufficient capacity to meet the mission requirements, as seen in Subsection 3.1.3. To guarantee proper power delivery, a Battery Management System (BMS) must be integrated to prevent overcharging and overdischarging, to allow every cell to be at the same potential and State of Charge (SOC) and to maintain the voltage within operational limits for rechargeable batteries. This involves constantly monitoring the state of charge, together with thermal control, to prevent the battery pack from operating at temperatures that could degrade its performance [28].

The highest-performing batteries in terms of specific energy and resistance to very low temperatures are lithium-based batteries. Specifically, for primary batteries, solutions such as Li/SO_2, $Li/SOCl_2$, Li/CF_x and Li/MnO_2 are used. There are also combinations such as $Li/CF_x - MnO_2$, which increase the discharge current at low temperatures compared to Li/CF_x cells alone, although this reduces the high specific energy typical of carbon fluoride cells [28]. For secondary batteries, the most performant ones are those made of lithium-ion.

In a Li-ion cell, the electrolyte is formulated to react during the initial cycles with the graphite surface, forming a Solid Electrolyte Interphase (SEI) layer that largely passivates the electrode against further reactions in subsequent cycling [28]. Although a fraction of the active material is consumed in this process, careful optimization of the initial cycling conditions, together with the appropriate selection of additives and electrolyte components, limits this consumption and promotes the formation of a relatively stable and highly conductive (to lithium ions Li^+) SEI. None of this occurs for a Li metal negative electrode. New Li surfaces are created during plating in each cycle, which react with the electrolyte to generate a new SEI. Consequently, the greater the metallic surface area, the greater is extent of the reactions [28]. After extended cycling, the surface area of the Lithium increases significantly with a corresponding increase in the reactivity,

which degrades the thermal stability of the system with the result that cells become increasingly sensitive to thermal abuse as they are cycled [28]. Another phenomenon due to cycling is the formation of dendritic Li plating morphology (filaments), which generally results in rapid Li degradation [28]. In physical terms, during charging Li^+ ions reach the anode; however, if the operating conditions are not favorable (low temperature or an anode that is already nearly saturated), electrons reduce Li^+ ions to metallic lithium on the anode surface according to the reaction in Equation 1.1.

$$Li^+ + e^- \rightarrow Li^0 \tag{1.1}$$

The main consequences of this phenomenon are the formation of electrically isolated metallic lithium, the growth of dendritic or filamentary morphologies, continuous electrolyte consumption due to the formation of new SEI, an increase in internal resistance with irreversible capacity loss, and, in severe cases, a potential risk of internal short circuit [28].

For lithium-based cells, the ionic conductivity of cathode material is determined by the mobility of the lithium ions, which is in turn defined by the material's structure. Cobalt enhances the chemical and thermal stability of Lithium-Ion Batteries (LIBs), Nickel improves the energy density of the battery and has the advantages of low cost and good conductivity and Manganese is a more affordable alternative to cobalt and nickel for use in LIBs [23]. Graphite, having a capacity of $372\,mAh/g$, is a popular choice for anodes due to its abundance, good electrochemical stability, safety, and low expansion volume during charge and discharge [23]. Carbon-coated graphite and graphite-silicon anodes are often considered to be better alternatives because they experience less degradation and can hold more lithium ions. Silicon is considered a potential alternative to graphite as an anode material in LIBs. It is considered a safe and reliable option with a sufficient energy density for use in electric vehicles. Despite this, silicon anodes have some downsides, including a volume expansion of up to 300 percent during charge and discharge, which can cause unstable SEI formation, low electrical conductivity, and mechanical grinding of graphite caused by the Si expansion/contraction [23].

The dissolution of a lithium salt, like lithium hexafluro phosphate ($LiPF_6$) in an organic carbonate, such as Ethylene Carbonate (EC), Dimethyl Carbonate (DMC), or Diethyl Carbonate (DEC), constitutes the electrolyte liquid solution [23]. Fluoroalkyl phosphates promise advantages for high voltage cells, increasing the electrochemical stability of the electrolyte while also providing flame-retardant properties and enhanced thermal safety [46]. Additives could be used for liquid electrolytes to enhance safety, minimize the loss of capacity during the first charge-discharge cycle, avoid oxidation and prevent gas production by electrolysis. To achieve higher voltage cathodes, electrolyte additives play the role of stabilizing agents, retarding the thermal decomposition of $LiPF_6$ salt [23]. For applications requiring high energy, the most promising otions are carbon-chloride batteries and possible hybrids with manganese oxide to achieve more stable performance.

In Tables 1.2, 1.3 and 1.4 are reported the performance of primary, secondary and reserve battery respectively.

Table 1.2: Typical range for Li-ion primary cells [28].

Chemistry	Nominal tension [V]	Specific energy [Wh/Kg]	Energy density [Wh/L]
Li/SO_2	3.0	260	415
$Li/SOCl_2$	3.6	590	1100
Li/CF_x	3.0	360	540
Li/MnO_2	3.0	260	546
Li/CF_x-MnO_2	2.5	380	923

Table 1.3: Typical range for Li-ion secondary cells [28].

Chemistry	Nominal tension [V]	Specific energy [Wh/kg]	Energy density [Wh/L]
$Li_xC_6/Li_{i-x}CoO_2$	3.8	200	570
$Li(Al)/FeS_2$	1.7	180	350
Li/MnO_2	3.0	120	265

Table 1.4: Typical range for reserve cells [28].

Chemistry	Nominal tension [V]	Specific energy [Wh/kg]	Energy density [Wh/kg]
$Mg/CuCl$	1.3	60	80
Zn/AgO	1.5	30	75
Li/FeS_2	1.6 - 2.1	40	100

Future trends

The low maintenance, the relatively long cycle life, and the low self-discharge have cleared the way for Li-ion to be used in electric powertrains. On the other hand, the Lithium-Ion Battery (LIB) suffers from cyclic and calendar aging, SEI layer formation, lithium plating, electrolyte degradation, side reaction products, and current collector corrosion. This is the main reason that LIB are always incorporated with a BMS, ensuring a high degree of protection.

Research efforts for batteries are focused on materials for the electrodes and electrolytes, the configuration and composition of the electrodes, the arrangement of the cells (in pouch, cylindrical, and prismatic shapes), the material and thickness of the separator [23]. Battery generations are classified according to the cathode material, anode material, type of electrolyte, and cell chemistry [23]. Current trends in battery technology involve the utilization of electrodes with higher capacities, such as sulfur ($1675\,mAh/g$), silicon ($4200\,mAh/g$), and lithium metal ($3863\,mA/g$), as well as the increase in single-cell voltage [23]. These developments collectively enhance the overall energy density of the battery; the primary approach is to elevate the cell's voltage up to $5\,V$ by incorporating high-voltage electrode materials (as current materials typically reach $4.2\,V$). However, achieving a stable electrolyte for sustained cycling poses a significant

challenge. An alternative is to increase the storage capacity of the battery in terms of weight or volume, which can be achieved by increasing the faradic capacity of the electrodes (mAh/g) [23]. Despite ongoing research into lithium-metal batteries (LMBs) and post-lithium technologies; it is evident that Lithium Metal Batteries, especially Solid-State Batteries (SSBs), represent a highly promising technology capable of significantly enhancing energy density and reducing hazardous effects typical of liquid electrolytes. Lithium-sulfur batteries (LiSBs), with lower environmental impact, better depth of discharge) and sodium-ion batteries are serious alternatives to lithium-ion batteries. Metal-air batteries (such as lithium-air batteries) promise theoretically specific energy comparable to gasoline [23].

In Table 1.5 the batteries technologies are listed by generations.

Table 1.5: Evolution of battery technologies and electrode materials [23].

Battery Generation	Electrode Active Materials	Cell Chemistry/Type	Implementation Date/Forecast	Market Deployment
Gen 1	*Cathode:* LFP, NCA, LCO *Anode:* Carbon / Graphite	Lithium-Ion	1991	Commercial
Gen 2a	*Cathode:* NMC111, LMO *Anode:* Carbon / Graphite	Lithium-Ion	1994	Commercial
Gen 2b	*Cathode:* NMC532, NMC622 *Anode:* Carbon / Graphite	Lithium-Ion	2005	Commercial
Gen 3a	*Cathode:* NMC622, NMC811 *Anode:* Graphite + 5-10% Si	Lithium-Ion	2020	Early mass deployment
Gen 3b	*Cathode:* High-Energy NMC, High-Voltage Spinel (~5 V) *Anode:* Silicon / Carbon	Optimized Lithium-Ion	2025	Emerging
Gen 4a	*Cathode:* NMC *Anode:* Silicon / Carbon Solid Electrolyte	Solid-State Lithium-Ion	2025	Pilot / Pre-commercial
Gen 4b	*Cathode:* NMC *Anode:* Lithium Metal Solid Electrolyte	Solid-State Lithium-Metal	>2025	R&D / Early pilot
Gen 4c	*Cathode:* High-Energy NMC, High-Voltage Spinel *Anode:* Lithium Metal Solid Electrolyte	Advanced Solid-State	~2030	R&D
Gen 5	Li-O_2 (Li-Air / Metal-Air) Li-S (Lithium-Sulfur) New ion-based systems (Na, Mg, Zn, Al)	Metal-Air / Li-S / Beyond-Li	>2030	Research

Liquid electrolytes in lithium-ion batteries (LIBs), composed of lithium salts dissolved in organic solvents, pose safety risks related to toxicity, leakage, and flammability. Solid-state batteries overcome these limitations by offering higher energy density, improved safety, reduced manufacturing costs, and longer shelf life [23].

The shift from Si/C anodes (Gen. 4a) to lithium-metal anodes (Gen. 4b and Gen. 4c) enables an increase in specific energy from over 400 Wh/kg and 800 Wh/L to beyond 500 Wh/kg and 1000 Wh/L [23]. However, solid-state systems still face challenges, including limited ionic conductivity, high interfacial resistance, interfacial instability, and the need for revised manufacturing processes [23].

Lithium-metal batteries employ a lithium-metal anode, insertion-type cathodes, and solid electrolytes such as polyethylene oxide (PEO). Lithium metal provides a much higher theoretical capacity than graphite (3860 mAh/g vs. 372 mAh/g), but PEO electrolytes suffer from limited voltage stability ($> 4\ V$) and require controlled operating temperatures. Consequently, their application is mainly restricted to LFP-based chemistries, while LFMP (lithium-iron-manganese-phosphate) cells paired with graphite anodes can charge up to 4.25 V, combining high power capability and excellent cycling performance [23].

The metal-air battery utilizes the electrochemical principle that involves a metal negative electrode (for example Zn, Al, Li, Mg and Ca) and an oxygen-reducing cathode made of mesoporous carbon (a porous carbon material whose characteristic pore diameters lie between about 2 nm and 50 nm) [23]. Metal-air batteries have a high amount of energy stored compared to their weight. Besides the lithium-air type, with a nominal voltage of 2.91 V, the metal-air batteries could include zinc-air, aluminum-air, magnesium-air, and calcium-air [23].

Lithium-sulfur batteries (LiSBs) use lithium metal as an anode, sulfur composite as a cathode, and organic liquid as an electrolyte. They exhibit high theoretical gravimetric capacity (1675 mAh/g) and high theoretical specific energy (2600 Wh/kg) [23]. Furthermore, the low cost, high abundance of sulfur, and absence of critical materials make LiS batteries a promising option for future energy storage applications. This type of battery has less environmental impact, as sulfur may be sourced from recycled materials [23]. The nominal voltage of a LiSB cell is 2.1 V. The battery has the potential to reach a deeper depth of discharge than the LIB, with the LiSB reaching 100% compared to LIB's 80% while maintaining his properties without major drawbacks and a longer lifespan estimated at 10 years [23]. LiS batteries suffers from the shuttle effect, which involves the undesired migration of lithium polysulfides between the cathode and anode; this phenomenon reduces capacity, energy efficiency, and shortens the cycle life of the battery [23].

The goal is to eventually replace lithium-based batteries with more sustainable and affordable light metals such as sodium. The main challenge lies in developing stable, high-energy electrodes with fast charge/discharge rates. Among various chemistries (Na, Mg, Zn), sodium-ion batteries (SIBs) are promising due to low cost, abundance, and similarity to LIBs, though they have lower energy density (around 90 Wh/kg) and shorter cycle life due to the difficult insertion of sodium ions into the anode and cathode [23].

Current sodium-based batteries include high-temperature systems, using liquid electrodes and ceramic solid electrolytes to maintain sodium in a liquid state and improve conductivity [23]. Sodium-Nickel-Chloride (NaCl) and Sodium-Sulfur (NaS) batteries operate at round 270 and 350 $°C$ and 300 to 340 $°C$, with energy densities of 120 Wh/kg and 220 Wh/kg, nominal voltages of 2.58 V and 2 V, and long lifetimes (up to 4500 cycles and more than 15 years of shelf life), but suffer from high-temperature operations, thermal losses, and low efficiency [23]. All-solid-state, room-temperature sodium-ion batteries are expected after 2030, with anticipated energy densities from 380 up to 700 Wh/kg, calendar life exceeding 30 years, and cycle life of

6000 to 12,000 cycles. Magnesium-ion batteries (MIBs) offer high specific energy and power, low cost, safety, and environmental benefits, but are not yet commercially available [23].

1.3.2 Solar arrays

Solar radiation as an energy source is already widely used on satellites and provides a radiative flux of approximately $1367 W/m^2$, referred to as Air Mass Zero (AM0). This radiation consists of photons, which are the elementary particles of light, each carrying quantized energy. Photons with sufficient energy are absorbed by suitable semiconductor materials, and the transfer of this energy creates an electron and a hole pair [47]. The energy of the photons must be higher than the energy gap of the semiconductor in order to be absorbed. The bandgap is the energy difference between the valence band and the conduction band of the semiconductor and represents the minimum photon energy required for absorption. Only photons with energy greater than or equal to the bandgap can contribute to photovoltaic conversion, as expressed in Equation 1.2.

$$h\nu \geq E_g \tag{1.2}$$

where h is Planck's constant (6.626×10^{-34} J s), ν is the photon frequency expressed in hertz (Hz, or s^{-1}), and E_g is the semiconductor bandgap energy, typically expressed in electronvolts (eV), where 1 eV = $1.602176634 \times 10^{-19}$ J.

In a photovoltaic device, however, a built-in asymmetry is present, which pulls the excited electrons away before they can relax and feeds them into an external circuit [47]. The excess energy of the excited electrons generates a potential difference, or electromotive force. Electrons are driven toward the negatively charged (n-type) region of the semiconductive material, while holes, representing the absence of electrons, are driven toward the positively charged (p-type) region of the semiconductor [47]. Electrons then pass through the external circuit via selective electrical contacts, producing electrical power. Figure 1.2 describes the physical basis of the photovoltaic effect in the solar cell where it is depicted a photovoltaic array simplified as a semiconductor with a p-type silicon layer and an n-type silicon layer. In the p-type region, silicon is positively doped with atoms acting as electron acceptors, while the n-type region is negatively doped with atoms acting as electron donors. Between these two regions lies the p-n junction, where the photovoltaic effect occurs [47]. When a load is connected to the cell terminals, electrons flow through the external circuit, generate electrical power, lose their energy, and circulate back to the holes in the p-type region. Different materials can be selected to act as a p-type or n-type as well for the p-n junction.

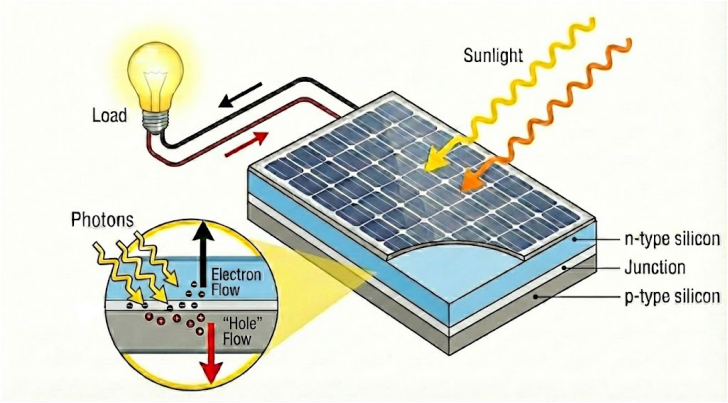

Figure 1.2: Photovoltaic effect. In the *p*-type region, silicon is positively doped with atoms acting as electron acceptors, while the *n*-type region is negatively doped with atoms acting as electron donors. Between these two regions lies the *p*-*n* junction, where the photovoltaic effect occurs when a load is connected to the cell terminals allowing electrons to flow through the external circuit, generate electrical power, lose their energy, and circulate back to the holes in the *p*-type region [47].

The efficiency of a solar cell depends on how many incident photons generate useful electrons: some photons have energy below the bandgap and are not absorbed, some have excess energy which is lost as heat, some of the generated electrons recombine with holes before being collected, and resistive losses in the material and at the contacts further reduce the extracted electrical power [47]. Its conversion efficiency must be as high as possible to allow a more compact array for the same power output. Currently, this efficiency reaches average values (i.e., averaged over the beginning and end of life) of around 30%.

This power solution necessarily requires the use of secondary batteries to store energy and supply it during the night, while during the day the batteries can absorb power peaks. In simple terms, a solar array for space applications consists of a substrate on which the solar cells are placed, and a Cell Interconnect Cover glass (CIC) for environment protection. Arrays can be mounted directly on the structure or designed in a deployable and rotatable configuration to optimize array orientation and, consequently, energy production. Being an external structure, it interacts directly with the space environment; therefore, it must withstand the typical temperature and radiation conditions of space. For lunar applications, it is necessary to consider the risk of micrometeorite impacts and dust deposition on the arrays, which can reduce performance.

Comparing the solutions of solar cells available on the market, depending on the technology and materials used, Table 1.6 is produced.

Table 1.6: Highest-efficiency commercially available solar cell technologies for different materials.

Technology	**Efficiency [%]**	**Producer**
CdTe Thin Film	21.5	First Solar [15]
CIGS / CIS Thin Film	23.35	Solar Frontier [41]
Si Heterojunction (HJT)	26.81	LONGi [30]
GaInP/GaAs/Ge (III-V Triple-Junction)	32.2	SpectroLab [43]

Since their introduction, crystalline silicon solar cells have dominated the photovoltaic market. However, traditional crystalline silicon cells have a major limitation, having a thick light-absorbing layer, consuming large amounts of silicon to be manufactured preventing significant cost reduction [31]. Silicon-based thin-film solar cells, including crystalline, amorphous, and microcrystalline types, require only a few micrometers of absorbing layer while achieving comparable or even higher efficiencies. Crystalline silicon thin-film cells retain the advantages of high efficiency, low toxicity, and wide raw material availability, while reducing silicon consumption and manufacturing costs [31]. Amorphous silicon cells, a direct bandgap semiconductor with broad light absorption and about 1 μm thickness, are inexpensive and simple to produce, though their infrared efficiency is limited. Microcrystalline silicon combines the advantages of amorphous silicon deposition technology with larger crystal sizes ($> 100\ \mu m$) to improve stability and efficiency on low-cost substrates [31].

CIGS ($CuIn_xGa_{1-x}Se_2$) thin-film cells offer high efficiency (over 20%), strong light absorption, and stable power generation. They can be fabricated on flexible substrates, making them suitable for building integration and space applications [31]. However, CIGS solar cells employ a Cadmium Sulfide (CdS) buffer layer (as a n-type semiconductor), which introduces environmental and health concerns due to the toxicity of cadmium. The buffer layer is a intermediate semiconductor layer placed between the absorber layer (p-type) and the window layer as shown in Figure 1.3 as an example.

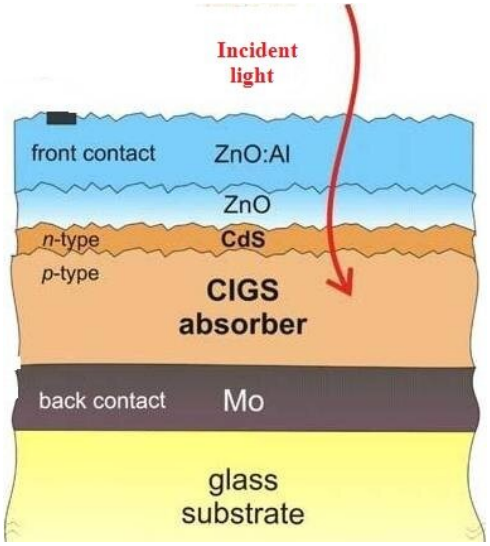

Figure 1.3: Typical CIGS solar cell stratification [40].

CdTe thin-film solar cells have been successfully industrialized and are known for high theoretical efficiency, high absorption coefficient, low temperature sensitivity, and low production costs. Their simple manufacturing process and inexpensive raw materials allow lower component costs than crystalline silicon cells. However, cadmium toxicity restricts their broader application and market expansion [31].

GaAs thin-film solar cells achieve the highest efficiencies with values above 30%, and are ideal for space applications due to their wide bandgap and high-temperature resistance over 400 K. They are expensive and rely on scarce materials, limiting large-scale civilian production [31].

Traditional PV cells are limited by the Shockley-Queisser limit which is the maximum theoretical efficiency of a solar cell using a single p-n junction giving a maximum efficiency of 30% at 1.1 eV [2]. However, new alternatives have emerged that surpass this constraint; one

such innovation is heterojunction cells, which combine different semiconductor materials to overcome previous limitations and utilize the benefits of both materials [2]. A specific type of these cells is multi-junction cells, which enhance the heterojunction concept by incorporating multiple junctions within a single cell, this enable the cell to surpass the Shockley-Queisser limit, theoretically, for an infinite number of layers, up to 68.7% for normal sunlight, or 86.8% using concentrated sunlight [2]. First developed in the 1980s, these cells use multiple semiconductor layers to capture a wider range of sunlight, thereby improving energy conversion efficiency compared to traditional single-junction cells. Early studies underscored the promise of III-V semiconductor materials, which facilitated the development of the first practical multi-junction solar cells (MJSCs) [2]. Typically, MJSCs consist of multiple layers of semiconductor materials, each possessing distinct bandgaps. The topmost layer is characterized by the highest bandgap, tailored to absorb high-energy photons, while the underlying layers have progressively lower bandgaps to capture photons with less energy. This layered configuration enables the cell to absorb and convert a broader spectrum of sunlight into electricity, resulting in higher overall efficiency [2]. MJSCs are commonly made of $GaInP/GaAs/Ge$ stratification for triple-junction solar cells, Gallium Indium Phosphide (GaInP) is used as the high-bandgap top layer for absorbing high-energy photons, Gallium Arsenide (GaAs) serves as the middle layer providing efficient absorption and favorable electronic properties, and Germanium (Ge) is employed as the substrate or bottom layer to absorb lower-energy photons transmitted through the upper layers [2].

Future trends

Recent advancements in PV technology have been largely driven by innovative materials such as perovskites, multi-junction cells improvements, quantum dots and organic photovoltaic cells.

Pervoskite based materials

Perovskite solar cells are a disruptive technology in the field of photovoltaics, showing an exceptional increase in power conversion efficiency during the last decade [38]. The perovskite crystal structure, a highly versatile and widely studied framework in materials science, as shown in Figure 1.4, is characterized by a cubic lattice, with large spheres representing the cations on the corners of that cube, smaller spheres indicating the internal cations, and the core sphere representing the central atom [2]. Oxygen anions occupy the vertices of the lattice, forming octahedra around the B-site cations. This configuration is critical to the unique electronic, optical, and catalytic properties of perovskite materials. The flexibility of the perovskite structure allows for the substitution of various cations at both the A and B-sites, enabling a wide range of compositions and functionalities.

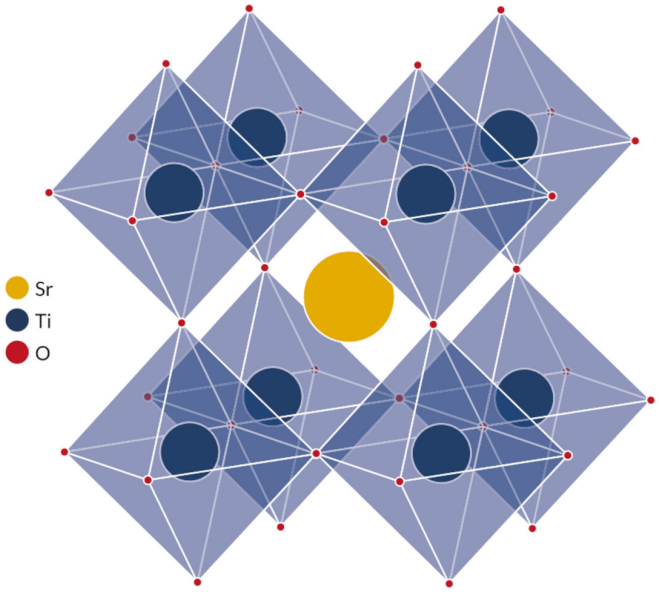

Figure 1.4: Perovskite cubic lattice [35].

Perovskite Solar Cells (PSCs) have demonstrated significant efficiency gains, with some studies reporting efficiencies exceeding 25% due to their adjustable bandgaps and ease of manufacturing [2]. Recent research projects have been centered on tackling the main limiting factors of PSCs, including long-term stability under real environmental conditions (humidity, oxygen, and thermal stress) as well as toxicity arising from lead-based perovskites [38]. Encapsulation techniques, compositional engineering, and the investigation of new lead-free perovskite material have been proposed to enhance stability [38].

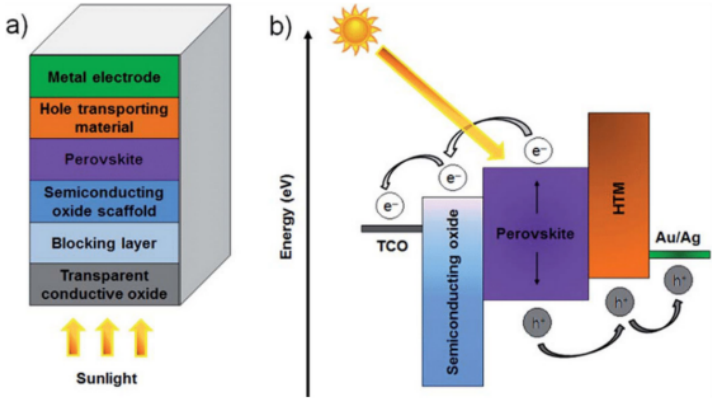

Figure 1.5: (a) Structure and (b) operational mechanism of a typical PSC [6].

Multi-junction improvements

The approach used for multi-juncion solar cells has been instrumental in achieving high efficiencies, with laboratory examples demonstrating efficiencies exceeding 46% under concentrated sunlight conditions [2][17]. While III-V semiconductors are the preferred choice due to their direct bandgap properties and high efficiency, their production costs and the complexities involved in manufacturing pose significant challenges. Research continues to explore alternative materials that could potentially lower costs, while maintaining or even improving efficiency

levels by, for instance, replacing traditional Germanium substrates with silicon which has been proposed as a cost-effective strategy without severely compromise performance [2].

Quantum Dots solar cell

Quantum dots (QDs) are a distinct category of semiconductors, consisting of nanocrystals formed from periodic series of II-VI, III-V, or IV-VI materials, capable of confining electrons through quantum confinement [2]. Quantum dots (QDs) exhibit discrete energy levels with an energy gap and level spacing that depend on their size, specifically the radius of the dot [2]. The effect of quantum confinement becomes significant as the size of a quantum dot approaches the exciton Bohr radius[1] of the material, and the levels of electron energy transition from a continuous band to discrete energy levels. The energy band gap enlarges as the size of the quantum dot diminishes. As the size of a quantum dot increases, its absorption peak is redshifted due to a reduction in its bandgap which can be optimized for specific applications in photovoltaics and other optoelectronic devices [2]. The tunable bandgap of quantum dots facilitates the development of nanostructured solar cells capable of capturing a greater portion of the solar spectrum. QDs possess substantial intrinsic dipole moments, potentially resulting in swift charge separation. QDs can emit up to three electrons per photon due to multiple exciton generation (MEG), in contrast to the single electron emitted by conventional crystalline silicon solar cells. Theoretically, this could enhance solar power efficiency from 20% to as much as 65% [2].

Organic solar cell

Another solution explored for solar cell are carbon-based materials which make up for the active layer of organic solar cells (OSCs) [38]. OSCs generally have an active layer situated between two transport layers that facilitate the movement of holes or electrons, along with two electrodes (cathode and anode) [2]. These substances are pliable and lightweight and can be manufactured cheaply via standard roll to roll printing methods. For the active material itself, OSCs are built up by a bulk heterojunction structure from a blend of organic electron-donating and electron accepting molecules. Excitons (comprised of a bound electron-hole pair) are formed within the donor material upon light absorption. These excitons are subsequently dissociated at the donor-acceptor interface and form separated charge carriers. These free carriers are then transported to the associated electrodes, where they create an electric current [38]. Organic solar cell are more flexible and lightweigth than common III-V based solar cells, and allow for diverse applications, including integration into building materials and portable devices; on top of that they can also be produced using environmentally friendly materials and processes, such as non-halogenated solvents, which improves their sustainability [2]. Recent developments have achieved power conversion efficiencies (PCEs) exceeding 19% [2], but more work is needed to allow OSCs to be more competitive versus more efficient solutions.

Although both effective donor and effective acceptor components are required for high-performance organic solar cells (OSCs), the development of new donors has received more attention than that of new acceptors over the past decade [49]. Most OSCs have used fullerene acceptors (FAs), that form bulk heterojunctions (BHJs) in devices, and advances in donor materials have led to single-junction donor. FAs exhibit robust charge percolation pathways, high electron mobilities, suitable electron affinities for charge separation with various donors (although, to some extent, this is because many donors have been designed for use with FAs),

[1] the average distance between an electron and a hole pair; the electron and hole pair is called ”exciton”

and the ability to form interpenetrating networks with donors [49]. However, FAs suffer from limited tunability of electron affinities, weak absorption in the visible and near-infrared regions, thermal and photochemical instability, limited applicability in high-voltage tandem sub-cells, and the need for time-consuming purification, which contributes to high costs, especially for more strongly absorbing fullerene (C_{70}) derivatives [49]. Organic non-fullerene acceptors (NFAs), such as perylene-based materials, offer the possibility of addressing these deficiencies through tunable chemical structures and electron affinities, increased visible and near-infrared (NIR) absorption, and in some cases easier synthesis; on the downside, 2D planar conjugated organic building blocks tend to exhibit inherently anisotropic crystal structures and electron transport, which may complicate the formation of effective electron-extraction pathways [49]. Ideally, NFAs should exhibit strong absorptions in regions of the visible and NIR spectrum that are complementary to those in which the available donors absorb, favourable morphologies for charge separation and forming percolation pathways, and good thermal and photostability [49]. Non-fullerene acceptors (NFAs) have emerged as a notable advancement in organic solar cells (OSCs), particularly in achieving power conversion efficiencies (PCEs) exceeding 20%. This progress is largely attributed to the unique properties of NFAs, which offer greater tunability and flexibility compared to traditional fullerene-based acceptors [38]

1.3.3 Fuel Cell

This solution has been conceived as a less polluting and more efficient alternative to conventional internal combustion engines, by reacting the fuel (such as hydrogen, methanol, formic acid, or hydrides that can also be used to produce hydrogen through chemical reaction) in an electrochemical cell.

A fuel cell is a galvanic device that continuously converts the chemical energy of a fuel and an oxidant directly into electrical energy. In Figure 1.6 a simple configuration is reported, where two catalyzed electrodes immersed in an electrolyte (in this case H_2SO_4 acid) and separated by a gas barrier to prevent the mixing of fuel and oxidant but permitting the ionic transport. The fuel, here hydrogen, is supplied to the surface of one electrode, while the oxidant, usually oxygen from ambient air, is supplied to the other electrode; both the fuel and the oxidant are supplied in their gaseous form.

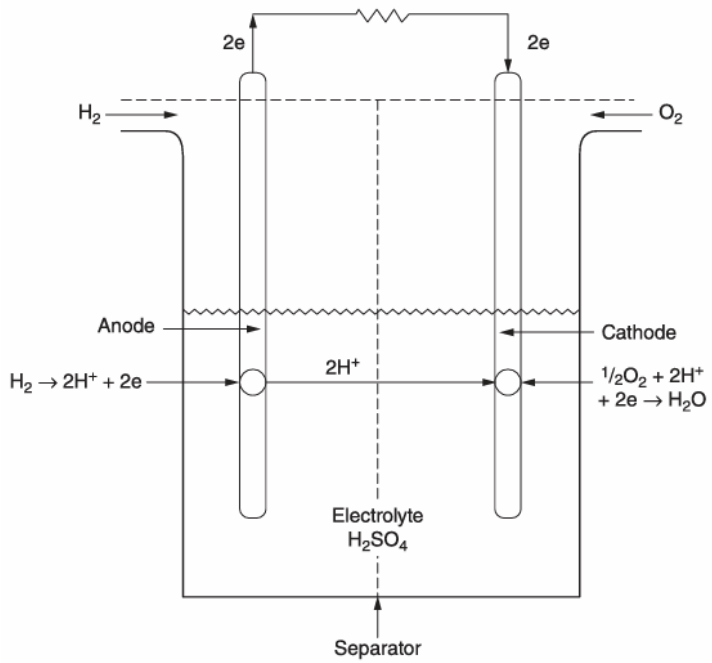

Figure 1.6: Example of a Fuel Cell working principle [28].

When the electrodes are electrically connected to an external load, the following processes take place [28]: First, hydrogen molecules dissociate on the catalytic surface of the fuel electrode, generating hydrogen ions and electrons, the hydrogen ions migrate through the electrolyte and the gas barrier to the catalytic surface of the oxygen electrode. At the same time, the electrons flow through the external circuit, delivering electrical power. Finally, oxygen, hydrogen ions, and electrons react on the cathode catalytic surface to form water as a reaction product [28].

The net exothermic reaction (Equation 1.3) is that hydrogen and oxygen produce water and electrical energy [28].

$$H_2 + \tfrac{1}{2}O_2 \rightarrow H_2O \tag{1.3}$$

Like batteries, this system directly converts electrochemical energy into electrical energy. Therefore, unlike heat engines whose Carnot efficiency expressed in Equation 1.4

$$\eta_{\text{Carnot}} = 1 - \frac{T_c}{T_h} \tag{1.4}$$

is strictly limited by the temperatures of the hot (T_h) and cold (T_c) sources, the fuel cell efficiency can theoretically approach unity and its efficiency can be estimate via Equation 1.5 [53].

$$\eta_{\text{FC}} = \frac{\Delta G}{\Delta H} \tag{1.5}$$

where:

- ΔG (Gibbs Free Energy): Represents the maximum available electrical work;
- ΔH (Enthalpy): Represents the total chemical energy available in the fuel [53].

The fuel cell depends exclusively on the electrochemical properties of the reacting species. However, the main difference with batteries lies in the fact that the substances at the anode and

cathode are supplied from an external source, providing advantages in terms of performance stability, since no chemical or physical changes occur at the electrodes [28]. The elements of the fuel cell are the same as in a battery, namely *anode, cathode, and electrolyte*.

Fuel cells can be classified into two main categories:

- **Direct Fuel Cells:** in which the fuel reacts directly within the fuel cell;
- **Indirect Fuel Cells:** in which the fuel is converted into a hydrogen-rich mixture and then supplied to the anode.

In addition to this classification, several types of Fuel Cells can be identified based on the type of electrolyte used [28]:

- **Solid Oxide Fuel Cell (SOFC):** These cells use a solid oxygen-ion-conducting metal oxide electrolyte and operate at temperatures between $700\,°C$ and $1000\,°C$, with an efficiency of up to 60%, slow start-up, and a large amount of excess heat once in operation. The anode, cathode, and overall reactions are as follows:

$$\begin{aligned} \text{Anode:} \quad & H_2 + O_2 \rightarrow H_2O + 2e^- \\ \text{Cathode:} \quad & \tfrac{1}{2}O_2 + 2e^- \rightarrow O^{2-} \\ \text{Overall:} \quad & H_2 + \tfrac{1}{2}O_2 \rightarrow H_2O \end{aligned}$$

- **Molten Carbonate Fuel Cell (MCFC):** These cells use a mixed alkali-carbonate molten-salt electrolyte and operate at temperatures around $650\,°C$, delivering high power from 100kW up to MW-level outputs. The anode, cathode, and overall reactions are as follows:

$$\begin{aligned} \text{Anode:} \quad & H_2 + {CO_3}^{2-} \rightarrow H_2O + CO_2 + 2\,e^- \\ \text{Cathode:} \quad & \frac{1}{2}\,O_2 + CO_2 + 2\,e^- \rightarrow {CO_3}^{2-} \\ \text{Overall:} \quad & H_2 + \frac{1}{2}\,O_2 + CO_2 \rightarrow H_2O + CO_2 \end{aligned}$$

- **Phosphoric Acid Fuel Cell (PAFC):** The electrolyte is concentrated phosphoric acid imbedded in a solid matrix such as SiC or polybenzimidazole (PBI) membrane. They Operate at lower temperatures, around $200\,°C$, with high overall efficiency up to 85% (45% in electricity and 40% in heat). The anode, cathode, and overall reactions are as follows:

$$\begin{aligned} \text{Anode:} \quad & H_2 \rightarrow {}_2H^+ + 2\,e^- \\ \text{Cathode:} \quad & \frac{1}{2}\,O_2 + 2\,H^+ + 2\,e^- \rightarrow H_2O \\ \text{Overall:} \quad & H_2 + \frac{1}{2}\,O_2 \rightarrow H_2O \end{aligned}$$

- **Alkaline Fuel Cell (AFC):** Used in the Apollo missions and to supply power to the Space Shuttle orbiter, they use circulated aqueous potassium hydroxide solution as the alkaline electrolyte. perform well at temperatures above $70\,°C$. The anode, cathode, and overall reactions are as follows:

$$\begin{aligned} \text{Anode:} \quad & H_2 + 2\,OH^- \rightarrow 2H_2O + 2\,e^- \\ \text{Cathode:} \quad & \frac{1}{2}\,O_2 + 2\,e^- + H_2O \rightarrow {}_2OH^- \\ \text{Overall:} \quad & H_2 + \frac{1}{2}\,O_2 \rightarrow H_2O \end{aligned}$$

- **Proton Exchange Membrane Fuel Cell (PEMFC):** These cells use a perfluorinated sulfonic acid ion-exchange membrane, operate efficiently at temperatures above $80\,°C$ and are characterized by rapid start-up. Electrodes consist of Catalyst layer (CL) which facilitate electrochemical reactions, providing pathways for both reactant transport and electron/proton conduction and a Gas Diffusion Layer (GDL) which conducts electrons, transports gas reactants and manages water. MEA is placed between two bipolar plates (BP) where gas flow channels (GFC) are placed [32]. The reactions at the anode, the cathode, and overall are the same as those in PAFCs. PEMs are typically based on Nafion, which remains widely used despite its high cost of approximately $2000\,\$/m^2$ [24]. This category also includes Direct Methanol Fuel Cells (DMFC) because DMFCs typically also use proton-exchange membranes, with the advantage of not requiring external processing since methanol has more favorable storage characteristics compared to previous solutions. The anode, cathode, and overall reactions are as follows:

$$\begin{aligned} \text{Anode:} \quad & CH_3OH + H_2O \rightarrow CO_2 + 6\,H^+ + 6\,e^- \\ \text{Cathode:} \quad & \frac{3}{2}\,O_2 + 6\,H^+ + 6\,e^- \rightarrow 3H_2O \\ \text{Overall:} \quad & CH_3OH + 6\,H^+ \rightarrow CO_2 + 2\,H_2O \end{aligned}$$

A summary of the Fuel Cell types is represented in Figure 1.7

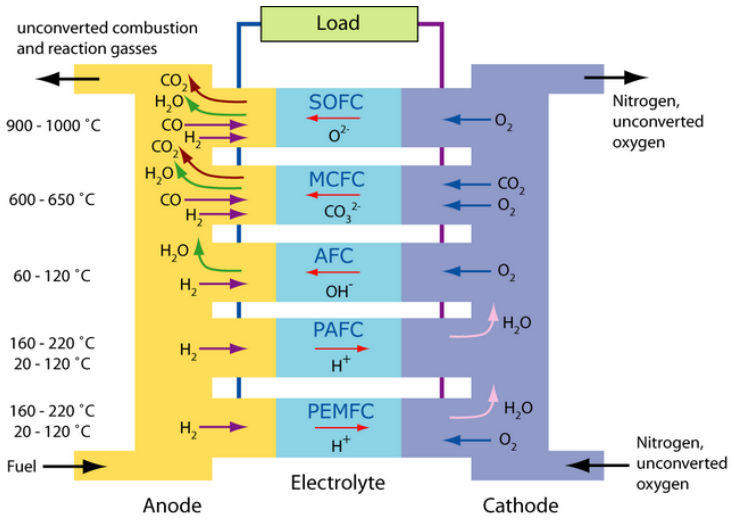

Figure 1.7: Different Fuel Cell types [14].

The voltage generated by the discharge of a fuel cell ranges from 0.4 V to 0.8 V, therefore multiple cells are connected in series to achieve the desired voltage. The most common configuration is the bipolar stack, in which each cell interfaces with the next through a bipolar plate that provides electron conduction and distributes the active components (gaseous hydrogen and oxygen) so that they do not mix and excessive heat does not accumulate inside as seen in Figure 1.8 [28].

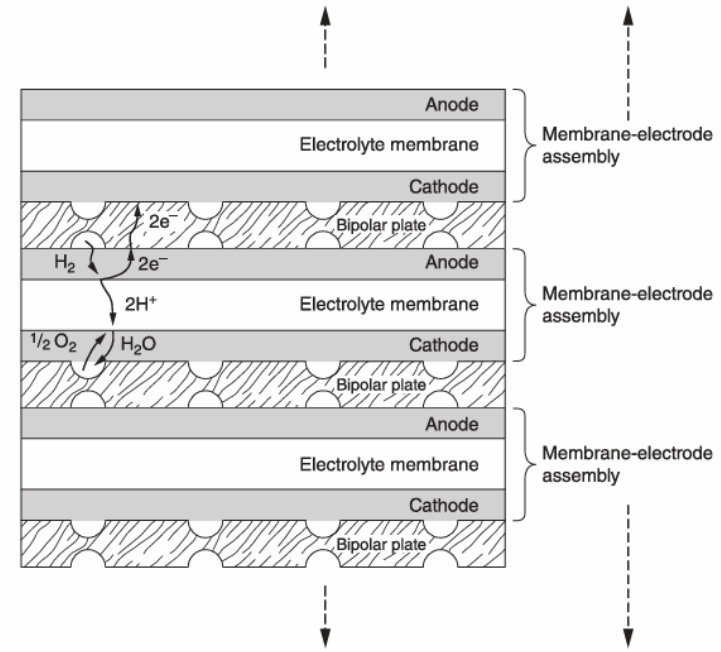

Figure 1.8: PEMFC stack with bipolar plates [28].

To reduce the overall volume and weight, a monopolar configuration can be used, in which the cells are arranged in a side-by-side configuration such that the electronic current is edge-collected at one electrode and passed on to the opposite electrode of the adjacent membrane-electrode assembly (MEA) [28]. The current can be increased either by enlarging the cell's active area (represented by the electrodes area), or by connecting multiple monoplanar "strips" in parallel as shown in Figure 1.9.

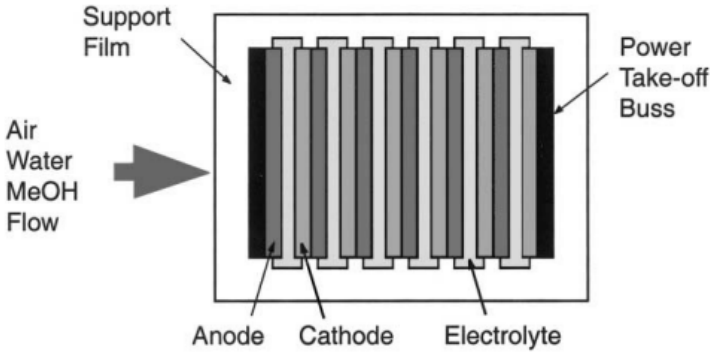

Figure 1.9: Strip cell concept [5].

A fuel-cell power generation system requires multiple subsystems and is generally more complex than a solution based solely on batteries, as it is necessary to manage the distribution of fuel and oxidant, as well as the heat generated; moreover, a device capable of supplying the energy required to initiate the reaction is needed [28]. To evaluate the performance of the fuel cell in a way that is directly comparable with batteries, the analysis considers the entire system, including the storage tanks. This allows the use of units in Wh/kg instead of W/kg, since the operation of a fuel cell necessarily requires external tanks to store both fuel and oxidant. Fuel cells can be coupled with solar arrays and batteries to reduce the size of the latter, in fact, in this configuration, the fuel cell provides continuous power, while the solar arrays supply renewable

energy during sunlight periods and the batteries compensate for transient power demands. The presence of the fuel cell could reduce the reliance on batteries for long-duration energy storage, allowing a trade-off in battery capacity, mass, and volume since it is no longer required to supply the entire power demand, but only to operate as a support system.

In Table 1.7 the performance of Fuel Cells compared by hydrogen source are reported.

Table 1.7: Net energetic characteristics of H_2/O_2 fuel cells [28].

H_2 Source	**Fuel storage**	**Specific energy [Wh/kg]**	**Energy density [Wh/L]**
Metallic hydrides	Metal-alloy powders	164	426
Chemical hydrides	Alkaline metal powders	592	-
Methanol (MeOH)	Liquid	289-805	141-385

For long-use power sources, advantages arise from the high energy density typical of fuel cells, which compensate for the drawbacks due to their relatively high weight, whereas batteries represent an excellent solution for short-duration or limited-use applications; this behaviour can be seen in Figure 1.10.

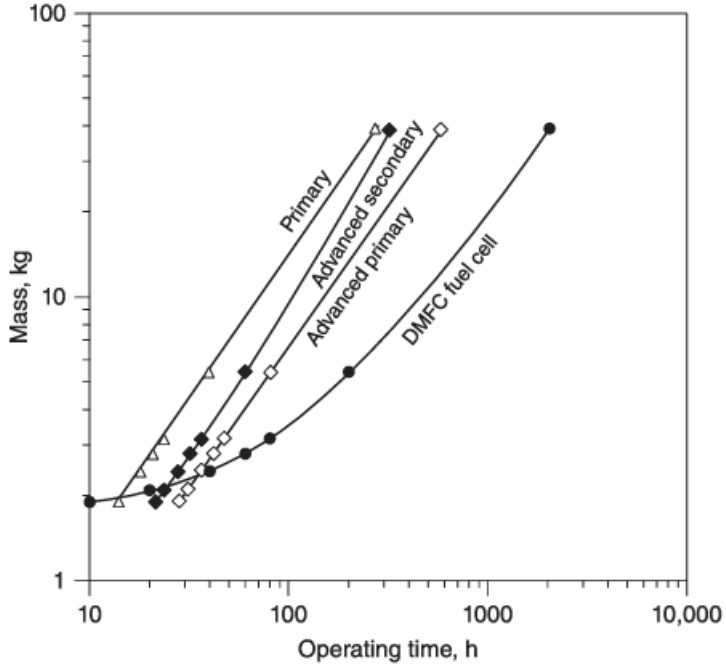

Figure 1.10: Comparison of electrochemical syatems-mass versus service time (based on 20 W output and the following specific energies: primary, 145 Wh/kg; advanced primary, 300 Wh/kg; advanced secondary, 225 Wh/kg [28]).

Future trends

Among the various fuel cell technologies, SOFC and PEMFC stand out as the most promising for future applications. SOFCs have been observed to display 60-80% higher conversion efficiency and longer durability compared to other types of fuel cells [32]. In addition, they are highly versatile, capable of utilizing a wide range of fuels, including hydrocarbons, methane, biogas, carbon monoxide, and natural gas [32] and the ability to operate at reactant pressure [18]. On

the other hand, PEM fuel cells offer advantages such as maintaining efficiency when downsized, providing high power density, being suitable for direct electrical power supply, and offering large energy capacity. Together, these properties make SOFC and PEMFC the leading candidates for next-generation fuel cell applications [32]. Both have advantages and limitations, with specific properties making each more suitable for particular applications. SOFCs operate at higher temperatures and are ideal for large-scale power generation, especially when heat dissipation is either not a concern or can be utilized for other purposes, while PEMFCs operate at lower temperatures and are preferred in applications where portability is critical [32].

The performance of PEMFCs relies on the seamless integration of the GDL with the flow-field structure [24]. This optimization strategy focuses on shortening the reactant transport pathways and reducing the overall thickness of the membrane electrode assembly (MEA), thereby decreasing both electrical resistance and mass transport limitations by rising the pressure drop generated within the structure compared with conventional MEAs, which promotes a more uniform distribution of reactants [24]. An example of unified MEA architecture, in which graphene foam simultaneously serves as the GDL and as the flow-field layer, improving fuel cell performance across a wide range of current densities [24]. To address both economic and performance limitations, several alternative membrane materials have been developed, including polybenzimidazole (PBI)-based membranes, sulfonated aromatic polymers such as polyphenylsulfone and Sulfonated poly(ether ether ketone), phosphonic-based membranes, polyphosphazene-based membranes, and polystyrene sulfonic acid (PSSA) with the properties of Nafion membranes, but with lower processing experiences and a simpler fabrication method [24]. Noble metal electrocatalysts are crucial in PEMFCs for their ability to accelerate the electrochemical reactions while ensuring long-term operational stability [24]. Among them, platinum remains the standard material for both the hydrogen oxidation reaction at the anode and the oxygen reduction reaction at the cathode, owing to its excellent catalytic activity and strong resistance to degradation. However, scarcity and cost drive research toward Pt-alloys (combining Pt with transition metals like cobalt (Co), iron (Fe) or, nickel (Ni)), core-shell nanostructures in which a thin layer of noble metal is coated over a non-precious metal core reducing noble metal usage while maintaining high performance [24].

To highlight the future trends of SOFC technologies, the work of Green *et al.* [18] emphasizes several unique advantages of this technology (on single cell level) in the context of producing the reactants required for energy generation directly from extraterrestrial environments. The capability to operate at reactant pressures below atmospheric levels may offer important advantages, particularly in environments where resources are available at near-vacuum conditions (such as the Moon) or at very low pressures (such as the Martian atmosphere, approximately 1% of Earth's atmospheric pressure). Operating under lower pressures could reduce subsystem requirements, for example by lowering the power needed to pressurize captured CO_2, or by decreasing structural and sealing demands for the electrolyzer due to the smaller pressure difference between the pressurized stack and the ambient environment [18]. The capability to process feedstocks with less-than-high purity may also reduce the hardware requirements for the purification of water ice eventually extracted from regolith sources. When only water is available (such as on the Moon, where ice deposits exist near the poles in permanently shadowed regions), solid oxide cells can operate in electrolysis mode to produce oxygen and hydrogen according to the overall reaction in Equation 1.6.

$$\mathrm{H_2O} \rightarrow \mathrm{H_2} + \tfrac{1}{2}\mathrm{O_2} \tag{1.6}$$

Solid oxide cells may be particularly advantageous because they potentially tolerate impurities present in water extracted from lunar regolith. Additionally, unlike low-temperature

electrolyzers such as PEMFC or AFC, they do not involve two-phase flow and offer improved thermal management as well as better compatibility with in situ water extraction processes on the Moon [18]. Furthermore, solid oxide cells generally operate more efficiently in electrolysis mode compared with low-temperature PEM or alkaline electrolyzers, mainly due to their lower thermoneutral voltage [18].

1.3.4 Radioisotope Thermoelectric Generator (RTG)

RTGs are included here for completeness, as they represent a viable power generation technology. However, a detailed discussion of RTGs will not be pursued and the following informations are only to acknowledge their existence, and potential applicability in crewed mission, without in-depth analysis.

A RTG operates by exploiting the energy emitted as radiation from an atomic nucleus with excess energy; the atom emitting this energy is therefore called a radioisotope [42]. A radioisotope is identified by the type of atom (symbol Z) and its mass number A. An atom that emits radiation during radioactive decay releases energy in the form of electromagnetic radiation and most of this energy is dissipated as heat. The working principle of RTGs rely on the heat generated and exploited by thermoelectric materials, which when in contact and in the presence of a temperature gradient, produce an electrical voltage called the Seebeck Voltage [42]. When two metallic conductors, materials 1 and 2 in Figure 1.11, of different natures are coupled and a temperature gradient is present, electrons tend to migrate from one conductor to the other, generating an electrical potential difference in an effect similar to an electrochemical cell [42]. This effect is known as the Seebeck Effect. The resulting electromotive force is directly proportional to the temperature difference between the hot and cold sides and to the physical properties of the materials [42].

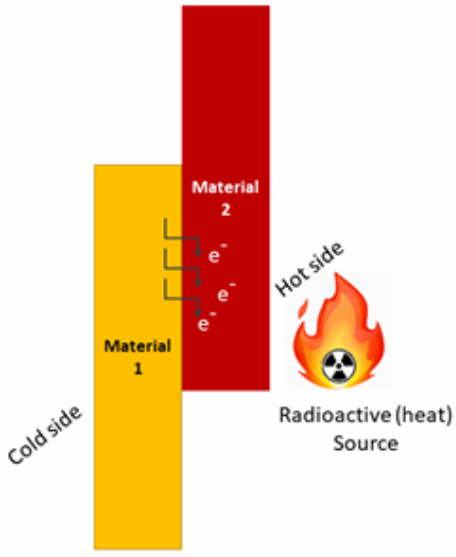

Figure 1.11: Seebeck effect [42].

After crossing the thermoelectric elements, the heat is transferred to the outer casing, which often has fins to dissipate unused heat to the external environment through irradiation and/or convection. Thermoelectric elements are usually arranged on the sides of the capsule that contains the radioactive material. One of its sides is in contact with the ”hot” source (capsule of radioactive material) and the other side is facing the ”cold” side. There must be a

temperature difference between the two sides of the thermoelectric elements so that the heat can be transformed into electric current. In principle, the greater the temperature difference between the sides, the greater the efficiency [42]. As the operation efficiency depends on the heat flow, the heat generated by the radioactive material must be removed from the device as efficiently as possible. Any amount of heat generated by the radioactive material that does not pass through the thermoelectric elements is wasted energy that contributes to lowering the efficiency of the device. Thus, the design of an RTG must be optimized to ensure that most of the heat generated is used by thermoelectric elements and that the temperature difference between the hot and cold sides is suitable for the material used [42].

The time it takes for a single atom to decay is unpredictable; however, by observing a sample of an isotope, it is possible to see that the number of decays follows a statistical law, which states that he number of decays in a time interval dt is proportional to the number of atoms N present [42]. A decay constant is therefore defined as

$$\lambda = \frac{\ln 2}{T_{\frac{1}{2}}} \tag{1.7}$$

derived from the half-life $T_{\frac{1}{2}}$, i.e., the time it takes for half of the radioactive nuclei in any sample to radioactively decay. After two half-lives, there will be a quarter of the original sample, after three half-lives, one-eighth of the original sample, and so on [42]. To describe the decay, a function f is used:

$$f = \lambda dt \tag{1.8}$$

The change in the number of atoms decaying over time is then given by

$$dN = -\lambda N(t) dt \tag{1.9}$$

or

$$\frac{dN}{dt} = \dot{N}(t) = -\lambda N(t) \tag{1.10}$$

This is a first-order differential equation whose solution governs the radioactive decay of the considered atom:

$$N(t) = N_0 e^{-\lambda t} \tag{1.11}$$

where N_0 represents the initial number of atoms. It can therefore be stated that the operational lifetime of an RTG is directly linked to the half-life of the radioisotope used.

However, there are three main disadvantages:

- Low efficiency;
- Weight proportional to the power output;
- High costs and maintenance requirements.

Additionally, adequate shielding is required for electronic devices and crew, which further increases the system's weight. To generate heat for conversion into electrical energy, radioisotopes that produce at least $0.1, W_{th}/g$ (W_{th} = thermal power produced) are reported in Table 1.8.

Table 1.8: Candidate heat sources for RTGs [3].

Radioisotope	Chemical form used	Thermal power [W_{th}/g]	Half-life [years]
^{244}Cm	CmO_2	2.27	18.11
^{238}Pu	PuO_2	0.49	87.74
^{90}Sr	$SrTiO_3$	0.46	28.8
^{241}Am	Am_2O_3	0.1	432.6

Curium (^{244}Cm) provides the highest specific power for a given mass, but its half-life is the shortest, resulting in a halving of power every 18 years. Strontium (^{90}Sr) has both a short half-life and low specific power, making it unsuitable compared to sources with higher half-lives and specific powers. Additionally, it emits β radiation, requiring heavier shielding.

In Europe, Americium (^{241}Am) has been chosen as the preferred isotope for radioisotope systems, mainly due to the scarcity and high cost of Plutonium (^{238}Pu). Meanwhile, in the United States, plutonium production resumed in 2015 specifically for space missions [3].

The thermoelectric generator is mounted on the surface of the heat source and consists of a material with electrons as the main carriers (n-type) and a material with holes as the main carriers (p-type). Historically, tellurium-based materials were used, particularly lead telluride (PbTe), with an operating temperature range of $300 - 800\,K$. At these high temperatures, inert gases such as argon or helium are needed to prevent sublimation of the thermoelectric material, which reduces efficiency. Over time, silicon-germanium alloys (SiGe) were chosen for their higher efficiency and higher operating temperatures without the need for inert gases, reducing the overall system weight. This led to the development of Multi-Hundred Watt RTGs (MHW-RTG) and General Purpose Heat Source RTGs (GPHS-RTG) with higher specific powers, respectively $4\,W_{th}/kg$ and $5.1\,W_{th}/kg$ [3]. Another configuration is the Multi-Mission RTG (MMRTG), which uses PbTe as n-type and segmented TAGS/PbSnTe as p-type, where TAGS refers to a material composed of Tellurium (Te), Silver (Ag), Germanium (Ge), and Antimony (Sb). The MMRTG configuration allows operation both in vacuum and in environments with an atmosphere. This duality results in lower specific power compared to SiGe systems; therefore, in a lunar environment with essentially no atmosphere, MMRTGs are more suitable than SiGe-based generators [3]. There is also an improved version of MMRTGs, called enhanced MMRTGs (eMMRTG), which use synthetic skutterudite (replacing arsenic in the natural $CoAs_3$ mineral with antimony $CoSb_3$, making it less toxic) instead of TAGS. This provides better performance at higher temperatures (TAGS deteriorate above 800 K), increasing efficiency [3]. For applications requiring americium oxides as the heat source, a solution using bismuth telluride (Bi_2Te_3) thermoelectric materials has been developed. These operate at lower temperatures with very low degradation over time ($\sim 1\%$) [3].

The energy conversion efficiency is expressed by the equation:

$$\epsilon = \frac{\Delta T}{T_H} = \frac{\sqrt{zT}}{\sqrt{zT+1} + \frac{T_C}{T_H}} \tag{1.12}$$

where T is the average temperature, T_H is the temperature of the hot side of the generator, T_C is the temperature of the cold side, $\Delta T = T_H - T_C$, and zT is the figure of merit of the thermoelectric material used to assess the efficiency of the material in converting thermal energy into electrical energy

$$zT = \frac{S^2}{k\rho}T \tag{1.13}$$

where S is the Seebeck coefficient $[V/K]$, ρ is the electrical resistivity $[\Omega \cdot m]$, and k is the thermal conductivity [W/m·K]. In Table 1.9 zT values for different materials are reported, where higher values are associated to higher performance.

Table 1.9: Figures of merit of thermoelectric materials [3].

Material	**Maximum** zT	**Temperature** $[K]$
$PbTe$	1.2-1.5	600-900
$SiGe$	0.7-0.9	> 1200
Bi_2Te_3	0.6-1	300-500

2 Context

2.1 Lunar environment

To identify mission requirements, it is important to analyse the operational environment, which presents additional constraints compared to Earth. The following sections discuss the characteristics of the lunar environment in agreement with the work of Grant H. Heiken *et al.* [20].

2.1.1 Terrain

Most of the lunar surface is composed of a thick layer of regolith, with craters ranging in size from $0.3\,m$ to over $1\,km$, and mountains up to $5.5\,km$ high, characterized by slopes of up to 45°. In general, avoiding grooves, fresh craters, and obstacles, traversing the lunar surface does not present major difficulties. There are two major types of geological regions on the Moon; Maria, the visibly darker regions on the Moon; and Highlands that are the lighter sections [52]. Whilst similar in nature, these regions differ in mineral and elemental concentrations affecting the dynamic of the regolith in these regions. Due to meteorite impacts that occur on the moon, the fractured layer of Lunar regolith is primarily made up of glassy shards and other various minerals comprising largely of oxides [52]. There are various forms of Lunar regolith. The dust portion is roughly 20% of the regolith weight and is defined by any particle size less than $20\mu m$. Regolith is a sand-like material, characterized by low electrical conductivity, which allows electrostatic charge accumulation when exposed to UV rays. This property causes regolith to adhere to surfaces, potentially damaging them [20]. Regolith dust also represents a human health risk, as it contains reactive particles, a significant portion of which fall within the respirable range [20].

2.1.2 Temperature

Temperatures vary significantly depending on the region. Generally, the average temperature ranges between $220\,K$ and $256\,K$, with fluctuations over the year of $\pm 140\,K$. Shadowed areas can reach temperatures as low as $40\,K$ [20]. Such variable temperatures impose critical design choices for both thermal control and propulsion selection, as batteries are highly sensitive to very high or very low temperatures.

2.1.3 Atmosphere

The lunar atmosphere is considered almost nonexistent, with a particle density 14 orders of magnitude lower than that of Earth. In a vacuum environment, heat transfer mechanisms differ significantly from those on Earth. Without a medium for convection, heat transfer relies primarily on radiation. This reliance creates distinct thermal challenges: spacecraft exposed to sunlight absorb substantial thermal energy on their sun-facing sides, while the shaded sides experience extreme cooling. This temperature disparity leads to significant thermal gradients across the spacecraft structure, potentially impacting material integrity and component performance [50].

The absence of an atmosphere leads to phenomena such as cold welding, a solid-state process in which two metallic surfaces bond without melting. This condition introduces risks of mechanism failure in space applications, where joints and moving components may unintentionally adhere due to vacuum conditions.

Additionally, outgassing occurs when gases trapped within materials under atmospheric pressure are released upon exposure to vacuum conditions [50]. In a vacuum, all materials

experience mass loss through evaporation or desorption processes. This effect is particularly relevant for organic polymers, which often contain low-molecular-weight additives originating from the polymerization process. These compounds diffuse to the material surface and subsequently desorb, although evaporation remains limited due to the low vapor pressure of polymers at nominal operating temperatures [50]. Outgassing poses several risks; it can contaminate sensitive surfaces, such as optical lenses, resulting in performance degradation [50]. It can also cause electrical arcing in high-voltage devices, thereby affecting their reliability [50]. Materials including composite structures, such as graphite/epoxy, may contain microscopic gas inclusions that are released when the ambient pressure decreases in space [50].

The atmospheric constituents include Neon, Hydrogen, Helium, and Argon, mainly derived from solar winds, while Argon is produced by the decay of ^{40}K (Potassium-40). Composition can vary significantly depending on the time of measurement, as the likelihood of contamination from human activity is very high.

2.1.4 Micrometeorites

Micrometeorites are natural solid bodies with diameters smaller than 1 mm. These bodies have velocities between 13 and 18 km/s, with a higher frequency on the side facing the direction of Earth's motion, due to Earth's gravitational attraction. To prevent damage from micrometeorites, shields are required to protect structures exposed for prolonged periods. The extent of damage depends on the impacted component and the size of the impacting object; for example, a body of 10^{-6} g produces a crater approximately 500 μm in diameter and a comparable or greater depth depending on the material's fragility. Critical components must therefore avoid being impacted.

2.1.5 Ionizing Radiation

The absence of a lunar magnetic field implies that the lunar surface is exposed to various types of ionizing radiation. These radiations are primarily composed of electrons and protons, with the presence of heavier chemical species depending on the type of radiation. Three main sources of radiation can be distinguished:

- Solar radiation;
- Cosmic rays;
- Secondary radiation.

In addition to the continuous flux of radiation from the solar wind, the Sun can produce sporadic high-intensity fluxes associated with solar eruptions, whose intensity depends on the solar cycle. During these events, mainly protons and He^{2+} ions are emitted with energies between 20 and 80 MeV, with peaks up to the GeV range. Cosmic rays originate from outside the solar system, with energies ranging from 10^9 to 10^{13} eV, with peaks up to 10^{20} eV, consisting of protons, alpha particles, and about 1% of atomic species with $Z > 2$. Cosmic ray flux is reduced during periods of high solar activity. Secondary radiation is produced by the interaction of cosmic rays and solar radiation with the regolith, causing spallation processes, elastic scattering, and neutron capture, which generate gamma rays, neutrons (predominantly), and nuclear fragments. In general, the products depend on the intensity of the incident radiation and the local regolith composition. The greatest risk is associated with solar radiation, while cosmic rays are considered a chronic exposure roughly 100 times higher than on Earth.

The characteristics of the lunar environment are summarized in Table 2.1.

Table 2.1: Lunar environment properties compared with Earth.

Property	Moon	Earth
Gravity at equator	$1.62\,m/s^2$	$9.81\,m/s^2$
Average surface temperature	-153°C ÷ 107°C	22°C
Maximum temperatures	-233°C ÷ 123°C	-89°C ÷ 58°C
Solar heat flux	$1361\,W/m^2$	$1000\,W/m^2$

2.2 Technological solutions

Terrain

Due to the Lunar environment, mitigation against the fine portion of the regolith, known as lunar dust, cannot be achieved with many terrestrial techniques such as water spray systems. Therefore researchers have opted to use new active methods, ranging from brushes and electro-dynamic methods for surface modifications. Most current technologies focus on removing dust from a surface, while little focus is on dust mitigation before the charged dust particles accumulate on sensitive equipment or infrastructure [52].

Several cleaning methods with demonstrated effectiveness on Earth will not work on the Lunar surface due to the drastically different environment. Even tests completed within a high vacuum may not prove to be as effective when implemented on the Moon due to the difference in weathering, radiation, and vacuum conditions [52].

There are two primary forms of dust mitigation techniques; active and passive techniques [52]. Passive techniques are focused on the idea that a surface will mitigate dust buildup over time without any required input of power or human interference. One of the most common implementations of a passive technique is surface modification where properties aim to reduce adhesion onto the surface [52]. An example is hydrophobic surfaces commonly used for terrestrial applications. Active techniques require input from an external source such as a human or machine. This can range from vacuum cleaning systems, to the use of electrostatic particle manipulation [52]. Studies looked at countering the van der Waals forces by treating a range of materials such as Kapton and quartz within a lab environment. A review of these passive mitigation techniques recommended that the material should not be highly pliable, i.e. that the material should be stiff enough to prevent particles from being embedded [52].

Temperature

For space applications, Multilayer Insulation (MLI) represents the most widely adopted passive thermal control solution. It consists of a stack of typically 8-15 layers of double-sided polyester films vapor-deposited with aluminum to reduce radiative heat transfer between layers, separated by polyester net spacers that minimize conductive coupling. The outermost and innermost layers are often realized in aluminum-deposited polyimide, characterized by enhanced resistance to temperature, radiation, and ultraviolet exposure [50]. MLI is specifically designed for vacuum operation, as its thermal insulation performance is significantly reduced in the presence of atmosphere [50].

Radiators constitute the primary means of rejecting excess heat generated by onboard equipment and external sources. Their performance is governed by high thermal conductivity to

spread heat and high surface emissivity to enhance radiative dissipation. Materials such as aluminum and Kapton are commonly employed due to their favorable mass and temperature tolerance characteristics [50]. Surface finishes are selected to ensure low absorptivity and high emissivity, thereby minimizing absorbed environmental heat while maximizing infrared emission [50].

Heat pipes (HPs) are passive two-phase heat transfer devices that exploit the latent heat of vaporization to transport thermal energy without external power input, providing high effective thermal conductivity with reduced mass penalty [50]. Heat input at the evaporator increases vapor pressure, inducing phase change of the working fluid (e.g., water or ammonia). The vapor flows through the adiabatic section toward the condenser, where it releases latent heat to the sink and condenses. Capillary forces within the wick structure return the liquid to the evaporator, closing the cycle. The overall heat transport capability depends on working fluid properties, wick characteristics (pore diameter, porosity, permeability), geometry, and operating temperature [50].

Loop Heat Pipes (LHPs) extend this concept by separating the evaporator and condenser through liquid and vapor lines, enabling long-distance heat transport and flexible integration within the system architecture. Their operation is based on a pressure differential generated between liquid and vapor phases, which drives circulation of the working fluid [50]. In configurations involving isotope heat sources, thermal energy can be directed to specific structural regions for equipment heating under cold conditions, while during high thermal input phases the loop allows heat rejection through radiative elements [50].

Phase Change Materials (PCMs) are employed to stabilize temperature or reduce radiator sizing by storing thermal energy during peak loads and releasing it under lower load conditions [50]. Their operation relies on the absorption or release of latent heat during solid-liquid phase transition, enabling near-isothermal behavior over the transition interval. By integrating a PCM with a radiator, the latter can be dimensioned for average rather than peak thermal loads, as excess heat is temporarily stored and later radiated. PCMs are commonly hydrocarbon-based and can be tailored to different transition temperatures. When coupled with heat pipes, PCM volumes may be integrated within dedicated cavities to mitigate temperature fluctuations of sensitive components. Current developments focus on advanced formulations, including high-porosity metallic foams and microencapsulated PCMs, to address limitations related to low thermal conductivity, volumetric expansion during phase change, and leakage phenomena [50].

Atmosphere

The main disadvantage of essentially no atmopsphere are cold welding and outgassing. Cold welding occurs exclusively in metal-metal contacts; therefore, metallic interfaces shall be avoided whenever possible, and when unavoidable, appropriate prevention measures shall be implemented [22]. Grease represents an effective cold welding inhibitor; however, its use in metallic contacts presents two main limitations: it tends to outgas under vacuum conditions, and in separable interfaces it can increase adhesion due to grease stiction, reducing friction while increasing the separation force perpendicular to the sliding surface, resulting in a suction-like effect rather than true cold welding [22]. Non-metallic contacts are not known to join, as polymers and ceramics cannot form cold welds due to their physical nature, but their mechanical properties limit their applicability, since high loads typically exclude polymers and brittleness constrains ceramic components [22]. Polymeric coatings may represent a compromise solution, but smilar to greases, many polymeric materials, including coatings, are subject to outgassing in vacuum and therefore require dedicated evaluation for each space mechanism [22]. If metal-metal contact

cannot be avoided, coating of the contact areas becomes essential, preferably through surface treatments that enhance subsurface strength and create an interlayer between the surface and the bulk material [22].

Outgassing reduction in vacuum systems can be addressed through four principal aspects: material selection, cleaning and handling, surface treatments, and baking [19]. These approaches can be interpreted as either temporarily stimulating desorption prior to operation, in order to remove as many adsorbed molecules as possible, or creating a surface barrier that limits desorption and bulk diffusion during service [19]. The first method to reduce outgassing is the appropriate selection of materials during system design [19]. Outgassing rates vary significantly with material type, but other parameter are evaluated such as the ability to be machined/fabricated, strength, retention of properties such as elasticity/fluidity at extremes of temperature), thermal properties (vapour pressure, expansion), gas loading (non-porous/no surface features to trap material and cause virtual leaks) as well as the cost, magnetic permeability, reactivity/volatility, radiation and corrosion resistance [19]. In general, metals exhibit lower outgassing rates than polymers, elastomers, oils, or greases, which should therefore be avoided whenever possible in vacuum environments [19]. Among metals, stainless steel is widely employed due to its corrosion resistance, moderate cost, ease of manufacture, capability to withstand high-temperature bakeout ($> 1000\,\mathrm{K}$), and relatively low intrinsic outgassing rate [19]. Surface treatments are frequently applied either to reduce effective surface area by lowering roughness or to develop a surface layer that is impermeable to gases or chemically inert, thereby limiting outgassing and re-adsorption [19]. Mechanical polishing is typically an initial cleaning step and may include grinding, milling, filing, brushing, and buffing to remove gross contaminants. Mechanical polishing alone provides only a limited reduction in outgassing and should be combined with more refined techniques [19].

Oxidation represents another important process to create a barrier layer against diffusion and permeation from the bulk [19]. Oxide layers promote the formation of stable surface compounds characterised by low outgassing rates, particularly in stainless steel and aluminium. A common method is air bakeout, in which the surface is exposed to air at elevated temperatures between 100 and 250°C, typically for 2 to 5 hours. This treatment produces an oxide layer significantly thicker than that obtained on a simply cleaned surface and is particularly effective in reducing hydrogen outgassing, although it does not generally achieve outgassing rates as low as those obtained through vacuum bakeout [19].

Vacuum baking is employed to remove both adsorbed and dissolved gases [19]. At temperatures between 100 and 500°C, with approximately 150°C sufficient for most applications, baking removes water vapour, including chemisorbed water on stainless steel, as well as gases such as CH_4, CO, and CO_2. At higher temperatures, up to approximately 1000°C for stainless steel, the process primarily targets hydrogen dissolved within the bulk material. Care must be taken when baking at elevated temperatures to avoid undesirable modifications of the material's mechanical properties. Proper cleaning and handling procedures are essential throughout the process to minimise contamination and prevent re-adsorption prior to operation [19].

Micrometeoroids

Micrometeorite and orbital debris (MMOD) impacts represent a general hazard of the space environment, requiring the adoption of proven and reliable protection strategies. The classic MMOD shielding solution is the Whipple shield, composed of a thin sacrificial bumper and a rear wall separated by an interior spacing, typically constructed of aluminum. Upon impact, the bumper fragments the incoming projectile, dispersing its kinetic energy before it reaches the

rear wall. Assuming the use of aluminum Whipple shields for missions such as Artemis, this configuration allows estimation of the minimum projectile size capable of penetrating the shield [45].

The design and sizing of MMOD protection rely on accurate characterization of the meteoroid environment. Current lunar impact monitoring techniques employ complementary observational strategies, including topographic mapping through laser altimetry, detection of impact-induced optical flashes, temporal imaging of newly formed craters, and scaling from bolide detection on Earth. These methods have significantly improved understanding of the lunar impact environment, particularly for meteoroid sizes that produce detectable optical or morphological signatures, although substantial uncertainties remain in quantifying the present-day impact flux [45].

To support engineering risk assessments, NASA employs the Meteoroid Engineering Model version 3 (MEM 3), a physics-based model of the inner solar system meteoroid environment. For a user-specified, time-dependent trajectory, MEM 3 provides velocity-resolved and directional meteoroid fluxes, along with bulk-density distributions, for masses ranging from 10^{-6} to 10^{1} g, accounting for gravitational focusing and planetary shielding by bodies such as Earth and the Moon [45]. Model predictions have been validated against spacecraft impact records, showing agreement within a factor of two to three. Although MEM 3 is commonly applied to Earth-orbiting and interplanetary missions, its directional and velocity-dependent outputs can be applied to object in the lunar environment as well [45]. In this configuration, the model provides site-specific meteoroid fluxes as a function of local time and look direction, enabling penetration analysis and damage-risk assessment for MMOD shielding solutions [45].

Ionizing radiation

For space applications, the primary defense is shielding. Time of exposure enters into the calculations in the sense that, where feasible, one may choose to minimize time in lightly shielded areas compared to time spent in more heavily shielded accessible areas [45]. For example, in situations such as Extra Vehicular Activity (EVA) or surface excursions you may consider returning to successively more shielded regions as the radiation background gets or is reliably forecast to become more intense (from space suit to transport vehicle to habitat to storm shelter within habitat, for example) [45].

While shielding generally refers to the matter between the environment and the endpoint that is being protected, the use of shielding is part of a radiation risk management strategy that includes: approved limits based on understanding of the relative risks, an operations concept to ensure that astronauts do not exceed these limits; physical shielding adequate to meet the radiation limits throughout the various phases of mission operations through the trapped radiation belts, in deep space, and on the lunar or planetary surface in a shielded surface module, in a transport vehicle, and in a spacesuit; radiation environment monitoring and warning including dose and dose rate monitors, space environment observations, space weather forecast centers, and transport codes to convert external environment to risk measures, and a communications system connecting space environment and dosimetry observations, forecaster centers, mission operations, and astronauts [45].

The purpose of shielding is to reduce exposure so that the cumulative total is below permissible limits, ideally substantially below the limits in accordance with the philosophy "as low as reasonably achievable." As an incident particle interacts with material shielding it loses energy until ultimately it transits the shielding at lower energy or comes to a halt. Along the way, the energy it gives up is absorbed by the radiation shielding material or is transferred to

secondary energetic particles which, in turn, continue losing energy as they transit through the shielding [45]. Low atomic mass materials are the best particles for blocking heavy ions and high-energy protons (like H^+). Hydrogen is a desirable element for this reason, but also because it contains no neutrons which limits secondary neutron production. The ideal shielding material would be pure hydrogen. Since that is not realistic, in practice low Z material with appropriate structural strength can be employed where practical. Water and polyethylene are good examples of effective shielding material. Low Z composites, approved for spacecraft applications, can be used as substitutes for interior structural elements [45].

3 Methodology

This section aims to identify the current approaches for accurately modelling the behavior of the proposed propulsion solutions, with the goal of selecting a method that is efficient both in terms of result reliability and the required computational cost. The process starts with the simplest solution, a propulsion system based exclusively on batteries, then considers a photovoltaic solution.

3.1 Batteries

For this section, lithium-ion batteries are considered, because of their high energy and power density.

To simulate the behavior of a battery pack, the analysis starts from the single cell. The main parameters on which an efficient model is based are the knowledge of the SOC, SoH (State of Health), OCV (Open Circuit Voltage), as well as currents and voltages over time, since nonlinear physical effects in batteries strongly influence their lifetime. An accurate battery model allows, during the design phase, to consider several factors such as charging strategies or extreme operating conditions. The main difficulty in modelling lies in the need to keep models as simple as possible.

In the literature, numerous different modelling methods are available, which can be mainly classified into three categories:

- Electrochemical;
- Mathematical;
- Equivalent Circuit Models (ECMs).

Electrochemical models are the more accurate but also more complex. They consider the chemical reactions happening through the electrodes to estimate the external parameters and are useful especially to describe thermodynamic and kinetic phenomena occurring in the cell. Mathematical models can be further divided into two categories: empirical and stochastic. Among the stochastic models, the Shepherd model provides low complexity and fast simulation, making errors of the order of $5 - 20\%$ [9]. ECMs are developed by using resistors, capacitors, and voltage sources in various combinations such as the Rint model, the Thevenin model and the Double Polarization (DP) model. For the Shepherd and Rint models, the parametrization can be implemented using just the information from the manufacturer's datasheets; however, their accuracy is limited by the precision of the curves and parameters reported. On the other hand, the Thevenin model requires a costly test bench and time-consuming experimental tests for its parametrization; the advantage, in this case, is the possibility of having a perfect knowledge of measurement and parameter estimation uncertainties. For the early design stages of a battery-powered system, the Shepherd and Rint models gave adequate simulation results, proving to be suitable [9].

For this analysis, the Shepherd model will be used, which, unlike the Rint model, is more suitable for identifying an appropriate battery since the parameters required for the simulation can be directly extracted from the discharge characteristic curve provided in the datasheets.

3.1.1 Shepherd discharge model

To understand the dynamic behavior of a lithium-ion battery during discharge, it is useful to examine a typical discharge curve, in which key points can be identified as shown in Figure 3.1.

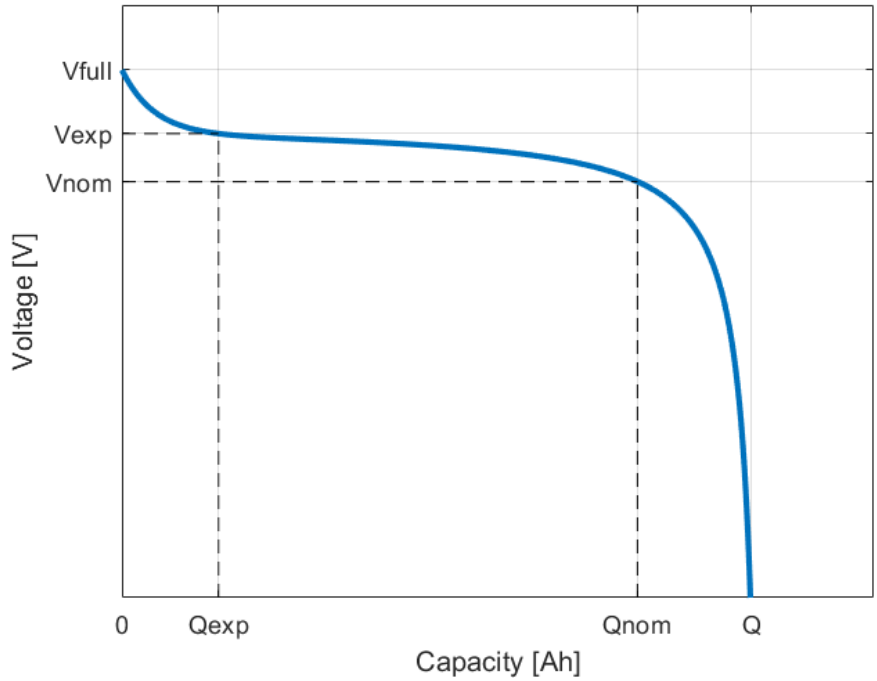

Figure 3.1: Typical Li-ion discharge curve [44].

The mathematical model implemented is represented in Figure 3.2.

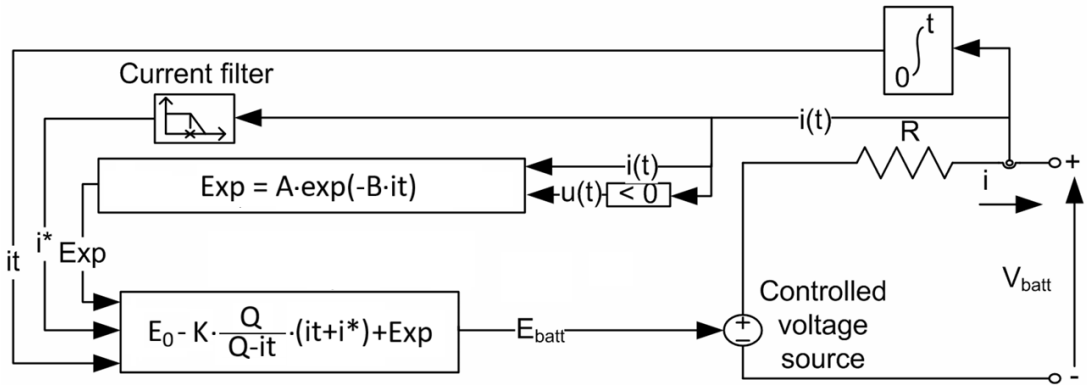

Figure 3.2: Shepherd discharge mathematical model [44].

The discharge phase is therefore described in Equation 3.1 and characterized by a current $i > 0$.

$$V_{\text{batt}} = E_0 - R \cdot i - \frac{K \cdot Q}{Q - it} \cdot it - \frac{K \cdot Q}{Q - it} \cdot i^* + A \cdot e^{-B \cdot it} \tag{3.1}$$

where $\frac{K \cdot Q}{Q - it} \cdot it$ is the *polarization voltage* and $\frac{K \cdot Q}{Q - it} \cdot i^*$ is the *polarization resistance* [44]; the other terms are described in Table 3.1.

Table 3.1: Parameters of the Shepherd battery model.

Parameter	Description	Unit
V_{nom}	Nominal voltage	V
E_0	Open circuit voltage	V
K	Polarisation constant or polarisation resistance	V/Ah or Ω
Q	Cell capacity	Ah
it	Actual battery charge	Ah
A	Exponential zone amplitude constant	V
B	Exponential zone time constant inverse	Ah^{-1}
R	Internal resistance	Ω
i	Battery current	A
i^*	Filtered current	A

For reference the actual charge parameter (it) is equal to zero when the battery is fully charged. The necessary input for the Shepherd's model are tipically found in batteries datasheet, and are:

- **R:** internal resistance;
- **Q:** battery capacity;
- V_{nom} **:** nominal voltage;
- V_{full} **:** maximum charge voltage.

Those quantities are necessary to derivate the full parameters set essential for the simulation, such as K , A , $E0$ and B which do not come with the battery datasheet and can be obtained through the definition of V_{exp}, Q_{exp} and Q_{nom}. To obtain the general parameters of the discharge model, it is necessary to set a discharge current i_s in order to simulate its behavior under optimal conditions. In terms of C-rate (described by equation 3.2), i_s is imposed at $0.2\,C$ to extract the parameters under optimal discharge conditions, which do not stress the cell by operating in high-current regimes or causing significant heating and polarization effects. The C-rate of a battery defines the charge or discharge current relative to its nominal capacity

$$\text{C-rate} = \frac{I_{\text{charge/discharge}}}{Q} \tag{3.2}$$

where $I_{\text{charge/discharge}}$ is the applied current [A].

Through several attempts, it was possible to identify definitions of these quantities that best adapt to different types of cells; hence, minor adjustments may be required depending on the specific battery under consideration.

V_{exp} is the voltage at the end of the exponential zone and is defined as:

$$V_{exp} = V_{full} \cdot 0.94 \tag{3.3}$$

Q_{exp} is the capacity at the end of the exponential zone and is defined as:

$$Q_{exp} = Q \cdot 0.015 \tag{3.4}$$

Q_{nom} is the capacity at the end of the nominal zone and is defined as:

$$Q_{nom} = Q \cdot 0.8 \tag{3.5}$$

B can be estimated via Equation 3.6 [44].

$$B = \frac{3}{Q_{exp}} \tag{3.6}$$

The others parameters can be obtained by known quantities [9]. First, some coefficients are defined:

$$C_{\text{exp}} = \frac{Q}{Q - Q_{\text{exp}}}\left(Q_{\text{exp}} + i_s\right) \tag{3.7}$$

$$C_{\text{nom}} = \frac{Q}{Q - Q_{\text{nom}}}\left(Q_{\text{nom}} + i_s\right) \tag{3.8}$$

$$E_{\text{exp}} = -V_{\text{exp}} - R \cdot i_s + (V_{\text{full}} + R \cdot i_s)e^{-B \cdot Q_{exp}} \tag{3.9}$$

$$E_{\text{nom}} = -V_{\text{nom}} - R \cdot i_s + (V_{\text{full}} + R \cdot i_s) \cdot e^{-B \cdot Q_{nom}} \tag{3.10}$$

Once these are known, we can finally estimate K , A and $E0$.

$$A = V_{\text{full}} - E_0 + R \cdot i_s \tag{3.11}$$

$$K = E_0 \cdot \frac{1 - e^{-B \cdot Q_{exp}}}{C_{\text{exp}}} + \frac{E_{\text{exp}}}{C_{\text{exp}}} \tag{3.12}$$

$$E_0 = \frac{E_{\text{exp}} \cdot C_{\text{nom}} - E_{\text{nom}} \cdot C_{\text{exp}}}{(1 - e^{-B \cdot Q_{\text{nom}}}) \cdot C_{\text{exp}} - (1 - e^{-3}) \cdot C_{\text{nom}}} \tag{3.13}$$

The particularity of this model is the use of a filtered current i^* flowing through the polarization resistance. In fact, experimental results show that, following a step change in current, the terminal voltage does not respond instantaneously but exhibits a slow dynamic behavior. Such dynamics are mainly associated with electrochemical polarization phenomena and charge redistribution processes. By filtering the current, the model is able to reproduce this delayed voltage response more accurately [44].

The filtered current $i^*(t)$ has been modeled using a first-order low-pass filter (Equation 3.14), which simulates an RC circuit as in Thevenin model.

$$i^*(t) = i_s(t) - \tau \frac{di^*(t)}{dt} \tag{3.14}$$

where:

- **dt** = integration step, it represents the precision of the filter and the simulation
- τ = time constant of the first-order filter for i^*, the smaller it is, the faster the change occurs

Typical values of τ for Li-ion batteries are between 1 and 10 seconds to achieve precise dynamic simulation. To evaluate the state of charge (SOC) Equation 3.15 is used.

$$SOC = 1 - \frac{1}{Q} \cdot \int_0^t i(t)\, dt \tag{3.15}$$

3.1.2 Shepherd charge model

To model the charging process inside the battery, the current has to change sign using $i < 0$. When the battery reaches the full charge, the voltage increases rapidly. This phenomenon is modeled by the polarization voltage term. In the charge mode, the polarization voltage increases until the battery is almost fully charged (it = 0). Above this point, the polarization voltage increases abruptly [44]. The polarization voltage is now given by equation 3.16.

$$Polarization\ Voltage = K \cdot \frac{Q}{Q - it} \cdot it \tag{3.16}$$

Experimental results have shown that the contribution of the polarization voltage is shifted by about 10% of the capacity of the battery [44], thus Equation 3.16 can be rewritten in Equation 3.17.

$$Polarization\ Voltage = K \cdot \frac{Q}{0.1 \cdot Q + it} \tag{3.17}$$

To describe the charging process Equation 3.18 is used.

$$V_{\text{batt}} = E_0 - R \cdot i - K \cdot \frac{Q}{0.1 \cdot Q + it} \cdot it - \frac{K \cdot Q}{Q - it} \cdot i^* + A \cdot e^{-B \cdot it} \tag{3.18}$$

3.1.3 Battery pack model extension

Once the model of the battery cell is completed, it is necessary to extent the simulation of a battery pack since the power needed to supply the rover could be reached only by using multiple battery cells.
To deliver power in the kilowatt range, it is necessary to use a high voltage for several reasons. The main reason is the need to limit the current so that smaller conductors can be used; the issue of cable size and weight will be analysed in Section 3.1.5. Achieving a high voltage requires connecting the cells in series to form a module (with n_s as the number of cells connected in series), according to the Equation 3.19

$$V_{bus} = \sum_{i=1}^{n_s} V_{cell_i} \tag{3.19}$$

V_{bus} has to be decided prior to the calculation, because is a design parameter. Since the cells are connected in series, only the voltage increases, while the capacity remains that of a single cell. To increase the capacity, the modules must be connected in parallel until the required capacity for the desired power is reached. To do so, it is required to know the necessary energy that needs to be delivered by the batteries. To determine the required energy, it is necessary to know the power profile, namely the power peak and the total delivery time $t_r = t_f - t_0$.

$$E(t) = \int_{t_0}^{t_f} P(t)\,\mathrm{dt} \tag{3.20}$$

In the case of a single constant power P_r or multiple constant power segments $P_{r,i}$, the total required can be calculated in Equation 3.21.

$$E_r = \sum_{i=1}^{N_P} P_{r,i} \cdot t_{r,i} \tag{3.21}$$

where $P_{r,i}$ and $t_{r,i}$ are the power and duration of the i-th segment, respectively, and N_P is the total number of segments.

Once the energy required is known it is possible to determine the necessary capacity via Equation 3.22

$$Q_r = \frac{E_r}{V_{bus}} \tag{3.22}$$

Finally it is possible to calculate the number of modules by dividng the required capacity Q_r by the capacity of the single cell Q_{cell}.

$$m = \frac{Q_r}{Q} \tag{3.23}$$

Having obtained the number of batteries to be connected in series (n_s) and in parallel (m), which are the data necessary to move from a single cell to the battery pack, the parameters governing the simulation are reported in Appendix A.

3.1.4 Validation

Cell

To validate this model, it's necessary to confront the simulation results with the experimental data present in literature [44]. For a given step current displayed in Figure 3.3 a voltage output is obtained and represented in Figure 3.4.

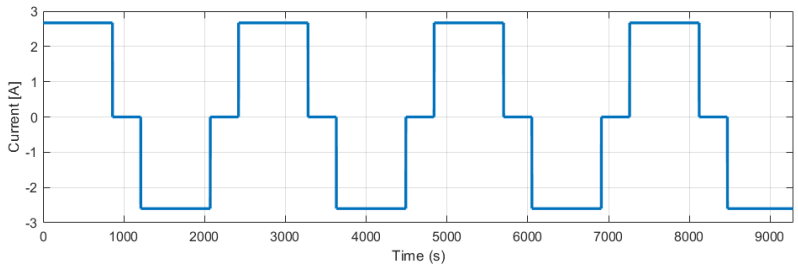

Figure 3.3: Current profile used for validating the battery cell model [44].

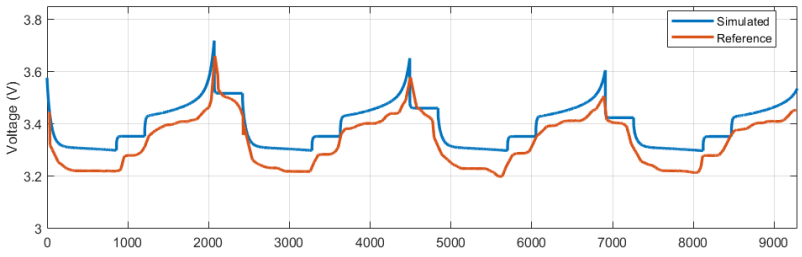

(a)

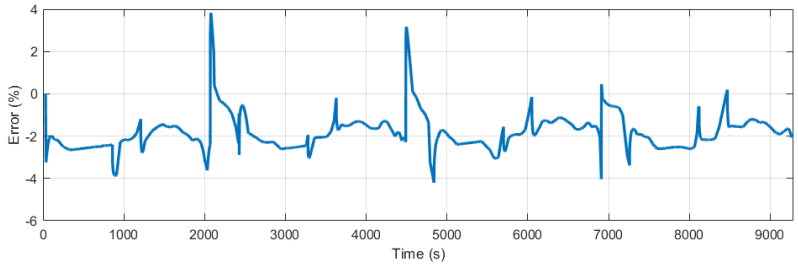

(b)

Figure 3.4: (a) Voltage output comparison bewtween the proposed model simulation and experimental as reference [44]; (b) percentual error of the simulated voltage.

This model exhibits an error between the real and simulated voltage within ±5% for SOC values above 20%, whereas below this threshold the error increases to approximately ±10% [44]. This level of accuracy is considered acceptable, since discharging Li-ion batteries beyond an 80% depth of discharge is generally not recommended.

Battery pack

Since the fundamental cell model has already been validated, the battery pack model is obtained through a direct series-parallel scaling of the individual electrochemical units. Therefore, the comparison with the results from Vratny *et al.* [48], who employ an Equivalent Circuit Model (ECM) to simulate the battery pack of a full-electric aircraft, serves as a system-level verification to ensure that the aggregated model correctly responds to high-power load profiles, rather than as a primary validation of the battery's internal dynamics.

By applying the same current profile as the reference (Figure 3.5), the resulting voltage, current, and SOC curves are obtained as shown in Figure 3.6.

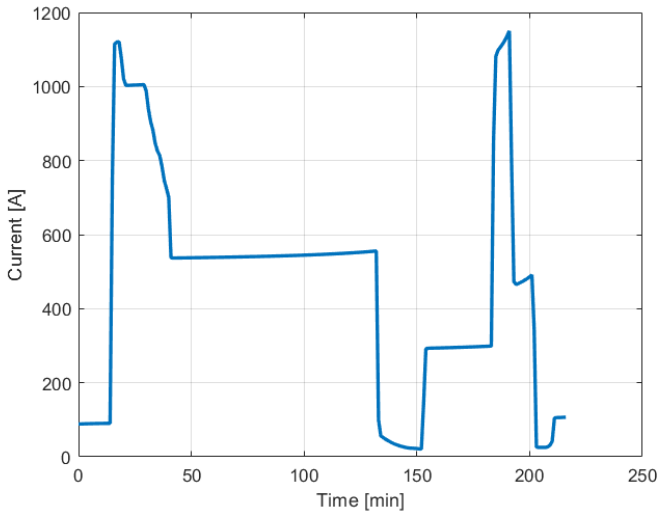

Figure 3.5: Current profile from Vratny C. *et al.* [48], used for validating the battery pack model.

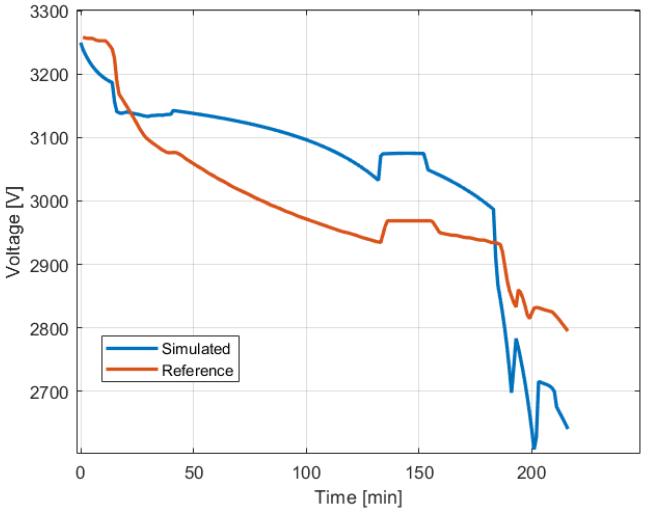

(a)

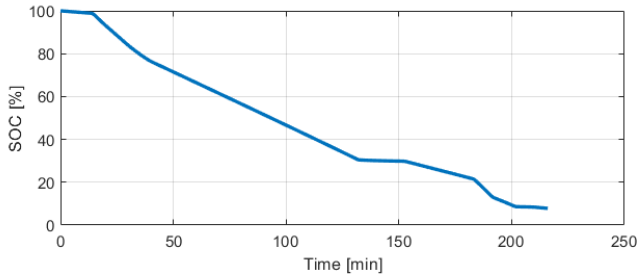

(b)

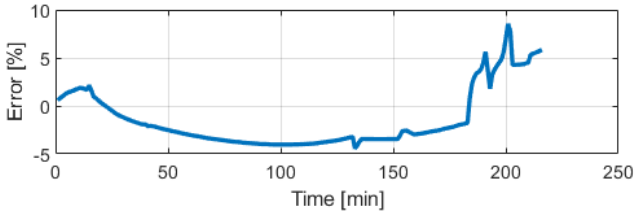

(c)

Figure 3.6: (a) Voltage output comparison bewtween the proposed model simulation and reference data [48], (b) State of Charge, (c) percentual error of the simulated voltage.

It is possible to observe some differences, mainly due to the use of different models for evaluating the battery voltage. In this work, the system input is based on a prescribed power demand profile; the corresponding current (Figure 3.5) is therefore derived by dividing the power request for the output voltage of the model, the battery voltage is therefore an output. Consequently, the key requirement is the model's ability to consistently capture voltage variations. The most significant differences concern the higher voltage drop highlighted by the reference [48], which cannot be fully replicated; this is due to the model used, which predicts a less steep but more contained discharge curve. Overall, the robustness of the model is confirmed by observing Figure 3.6c percentage variations around 5%, with a reduction in accuracy for SOC values below 20% as expected from the Shepherd model assumptions.

3.1.5 Cable sizing

A very important factor in the analysis of electric propulsion systems is the size, and therefore the weight, of the cables used to distribute power to the various subsystems. Since the power levels involved are very high, a greater cable mass can be expected compared to lower-power applications, making this a critical factor in overall mass estimation.

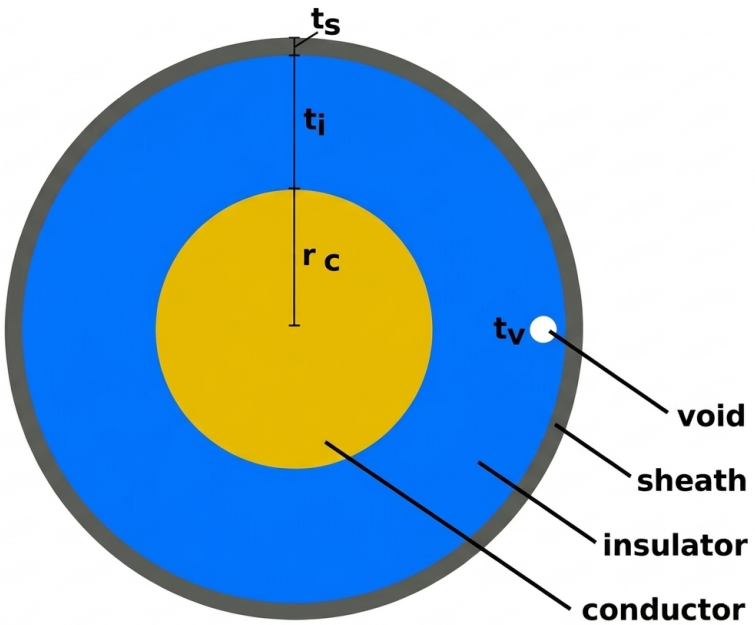

Figure 3.7: Cable section [4].

Figure 3.7 illustrates the cable structure adopted as reference for the cable sizing, where r_c is the conductor radius, t_i and t_s are the insulator thickness and the sheath thickness respectively. Since the insulation is typically made of a polymeric material, it can contains microscopic voids and defects within its structure due to their manufacturing process. These voids can locally reduce the effective dielectric strength of the material, diminishing its ability to withstand an applied potential difference without electrical breakdown [8]. Consequently, the presence of such voids should be taken into account during the modelling of the insulating component. The presence of voids is considered by introducing a defect in the insulator layer represented as t_v.

The thickness of the insulating layer is the key sizing parameter, as it depends directly on the conductor diameter and therefore on the operating current, as well as on the applied voltage [4].

$$t_i = f(K_s, V_{max}, t_v, \alpha_v, r_c) \tag{3.24}$$

Where K_s is the shape factor of the void defined by equation 3.29 which is assumed to be spherical to simulate the worst-case scenario. V_{max} is the maximum voltage delivered while operating, α_v is the minimum breakdown voltage of air in the cavity which is assumed to be $340\,V$ [4]. The mass-per-length is a function of the material densities and their thickness.

$$\bar{m}_{cable} = f(r_c, t_i, t_s, \rho_c, \rho_i, \rho_s) \tag{3.25}$$

Insulation thickness is computed using the Single Void Discharge (SVD) method described by Cheng [8], it is therefore assumed that only a single void is present in the cable. The most critical factor in sizing the insulator layer for solid power cable is the ionization in voids due to

partial discharge (PD) which lead to dielectric degradation and eventual cable failure [8]. Since the distribution of void is random, the worst case assumption that a void of maximum size is located at the conductor surface has to be made [8]. These methods do not depend on conductor material and it is assumed that they are valid for both copper and aluminum conductors [4].

The core of the SVD method is the calculation of the minimum discharge inception voltage $V_{m'}$. This is the lowest peak voltage at which a partial discharge can ignite within the worst-case void. For a spherical void at the conductor surface, it is given by equation 3.26 [8].

$$V'_m = \frac{\alpha_v \, r_c}{K_s \, t_v} \ln\left(\frac{r_c + t_i}{r_c}\right) \tag{3.26}$$

The fundamental design criterion to avoid damaging PD is that the peak operating voltage V_p must not exceed this threshold:

$$V_p \leq V'_m \tag{3.27}$$

For a solidly grounded system (Category A in IEC 60502-1:2021 standards), the peak phase-to-ground voltage is $V_p = V_{\max} \cdot \sqrt{2/3}$ [8]. By imposing the limit condition $V_p = V'_m$ and solving Equation 3.26 for t_i, it is possible to relate the insulation thickness to the system voltage, as reported in Equation 3.28 [8].

$$t_i = r_c \cdot \left(\exp\left(\frac{K_s \cdot V_{\max} \cdot \sqrt{2/3} \cdot t_v}{\alpha_v \cdot r_c}\right) - 1\right) + C \tag{3.28}$$

$$K_s = \frac{3 \cdot \epsilon}{1 + 2 \cdot \epsilon} \tag{3.29}$$

C is a constant with a value of $0\,cm$ for cables with voltages at or above $20\,kV$ and $0.1\,cm$ for cables with lower voltage and tv is assumed to be $0.0050\,cm$ (defined for a fresh extruded cable [10]) and ϵ is the dielectric permittivity of the material.
Cable mass-per-length can now be calculated as the summation of conductor, insulator, and sheath mass. Conductor mass-per-length, $\bar{m}_c$ is calculated in Equation 3.31 as the product of the conductor area A_c, defined in Equation 3.30, and the conductor density ρ_c [4].

$$A_c = r_c^2 \cdot \pi \tag{3.30}$$

$$\bar{m}_c = A_c \cdot \rho_c \tag{3.31}$$

Insulator mass-per-length, $\bar{m}_i$, is calculated by finding A_i, which is the area of the insulator, and multiplying by ρ_i, the density of the insulator material:

$$A_i = (t_i + r_c)^2 \cdot \pi - r_c^2 \cdot \pi \tag{3.32}$$

This reduces to:

$$A_i = \left(t_i^2 + 2 \cdot t_i \cdot r_c\right) \cdot \pi \tag{3.33}$$

$$\bar{m}_i = A_i \, \rho_i \tag{3.34}$$

Similarly, the sheath area is determined by assuming a sheath thickness t_s, typically on the order of 0.1 cm:

$$A_s = (t_s + t_i + r_c)^2 \cdot \pi - (t_i + r_c)^2 \cdot \pi \tag{3.35}$$

The sheath mass-per-length, $\bar{m}_s$, is a function of the sheath material density ρ_s:

$$\bar{m}_s = A_s \cdot \rho_s \tag{3.36}$$

Finally, cable mass-per-length is the summation of conductor mass-per-length, $\bar{m}_c$, insulator weight $\bar{m}_i$, and sheath mass-per-length $\bar{m}_s$.

$$\bar{m}_{cable} = \bar{m}_c + \bar{m}_i + \bar{m}_s \tag{3.37}$$

For insulation and sheath layers the polyimide is chosen due to its excellent physical, chemical and electrical properties on top of the very high thermal resistance between -200 and $+200\,°C$, while using copper for the conductor material.

Table 3.2: Cable materials.

Material	**Density** $[kg/m^3]$	**Dielectric permittivity**
Copper	8960	-
Polyimide	1430	3.4

The conductor radius estimate is based on the American Wire Gauge (AWG) standard, which provides the maximum current allowable for a given cable size, as reported in Table B.1 in Appendix B. It is therefore possible to predict how the conductor radius varies with the current and, consequently, with the voltage for a fixed power demand.

The conductor radius r_c is determined as a function of the bus voltage V_{bus} by imposing a constant power. For a given power P, the current is defined by Equation 3.38.

$$I(V_{bus}) = \frac{P}{V_{bus}} \tag{3.38}$$

Therefore, for fixed P, the current decreases hyperbolically with increasing bus voltage. Each AWG code corresponds to a specific conductor diameter, which in turn is associated with a maximum allowable current. The operating current is obtained from Eq. 3.38 and compared with the tabulated current ratings. Since the AWG table is populated by discrete values, the current-radius relationship is transformed into a continuous function by estimating intermediate, non-tabulated values through linear interpolation.

$$r_c(V_{bus}) = \frac{1}{2}\, d_c(I(V_{bus})) \tag{3.39}$$

This approach generates a continuous curve of r_c values (Figure 3.8), which provides a preliminary indication of the required equipment. However, commercially available r_c values are discrete, so the obtained results must be interpreted and compared with existing market solutions, or alternatively used to fabricate ad-hoc configurations. Since $I(V_{bus})$ decreases as V_{bus} increases, the interpolated diameter, and consequently r_c, are decreasing functions of V_{bus} for constant power. This reflects the physical scaling law whereby higher distribution voltages reduce current demand, enabling smaller conductor sections while maintaining the same transmitted power and respecting thermal current limits. The resulting dependence $r_c(V_{bus})$ is

therefore governed by the inverse proportionality between current and bus voltage under constant power operation as shown in figure 3.8.

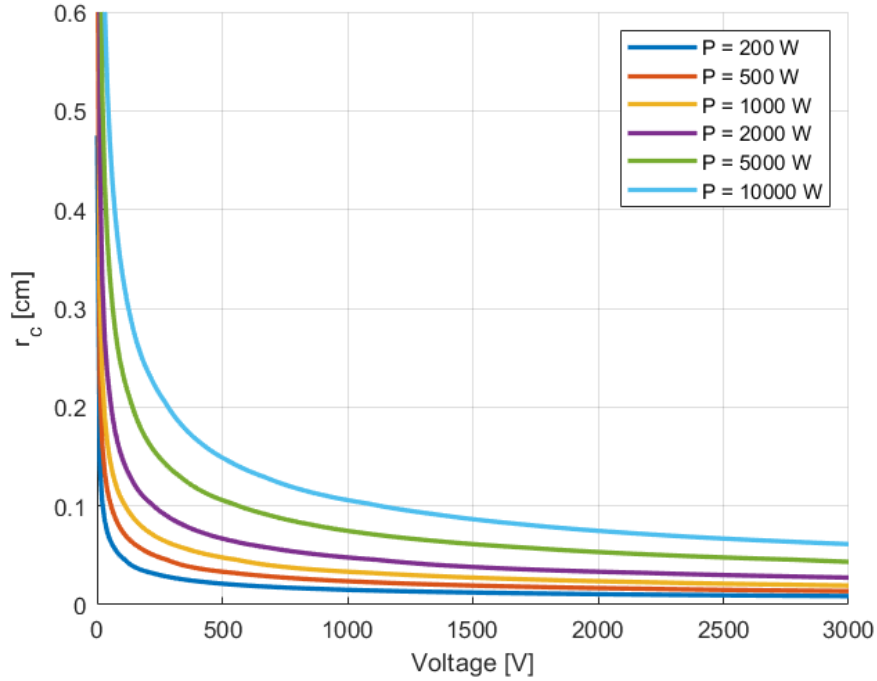

Figure 3.8: Conductor radius as a function of voltage and power.

While r_c decreases as the voltage increases, the insulation thickness increases to prevent PD damage.

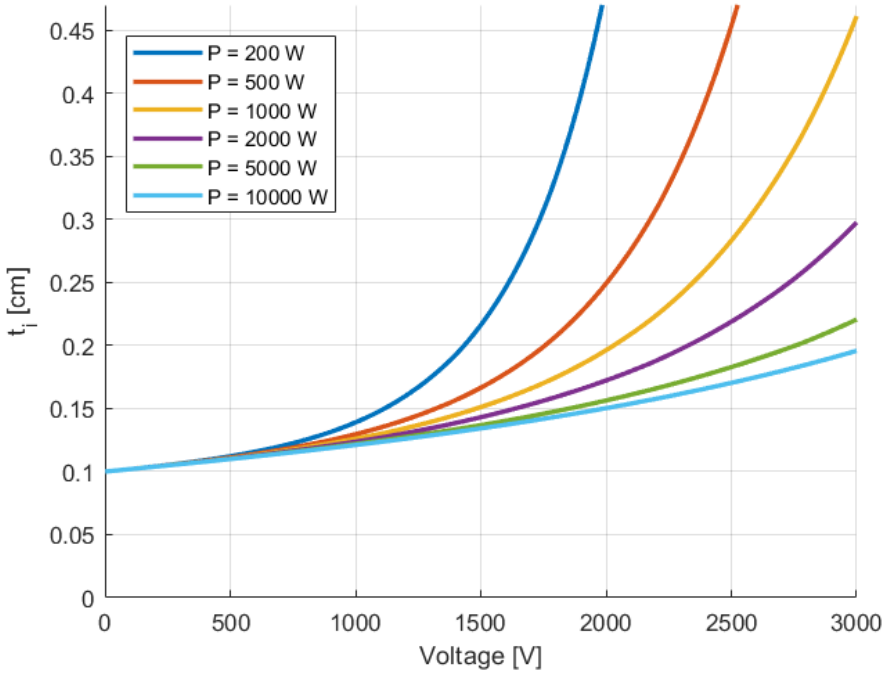

Figure 3.9: Insulation thickness as a function of voltage and power.

Figure 3.9 shows the insulation thickness as a function of voltage and power. For a fixed voltage, increasing the power implies a higher current, according to Equation 3.38. As the current increases at constant voltage, a larger conductor radius r_c is required to satisfy current density and thermal constraints.

From Eq. 3.28, it can be observed that r_c affects the insulation thickness in two different ways: it appears both as a multiplicative factor outside the exponential term and in the denominator inside the exponential term expressed in Equation 3.40.

$$exponential\ term = \left(\exp\left(\frac{K_s \cdot V_{\max} \cdot \sqrt{2/3} \cdot t_v}{\alpha_v \cdot r_c} \right) - 1 \right) \tag{3.40}$$

Therefore, variations in r_c do not produce a simple linear scaling of t_i. An increase in r_c simultaneously enlarges the prefactor and reduces the argument of the exponential, leading to a non-trivial combined effect on the resulting insulation thickness represented in Figure 3.9 where, for higher power, the required insulator thickness diminishes for a given voltage.

This effect can be more clearly visualized by comparing two configurations at different power levels in Figure 3.10. It can be observed that, at lower power, the exponential term maintain higher values than in the 10 kW case over the same voltage range.

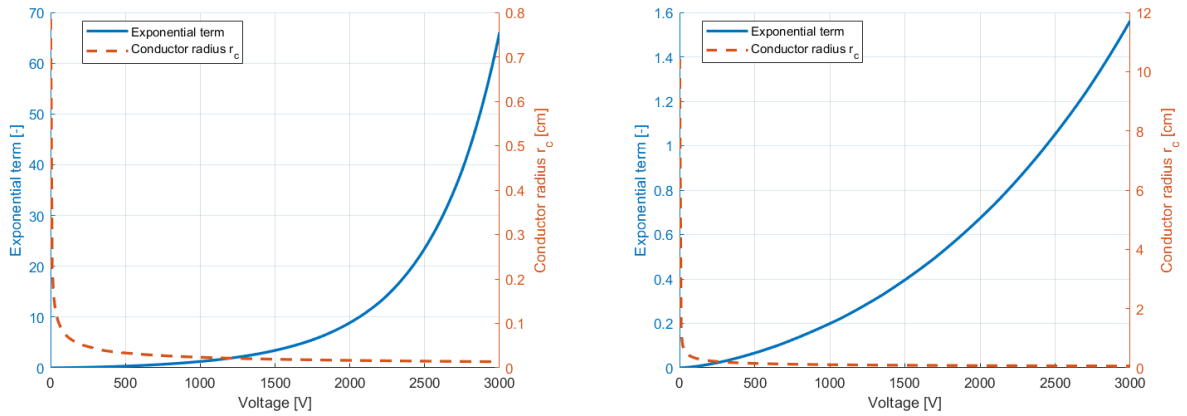

(a) P = 500 W **(b)** P = 10 kW

Figure 3.10: Exponential term and conductor radius as a function of voltage for two different power levels.

By neglecting the contribution of the coefficient C in Equation 3.28, the insulation thickness scales with the product $r_c \exp(\cdot)$. As the exponential term assumes higher values at lower power levels, the resulting insulation thickness becomes larger in the low-power configuration, as illustrated in Figure 3.10.

It is therefore possible to predict the mass-per-length ratio for a given power level as shown in Figure 3.11.

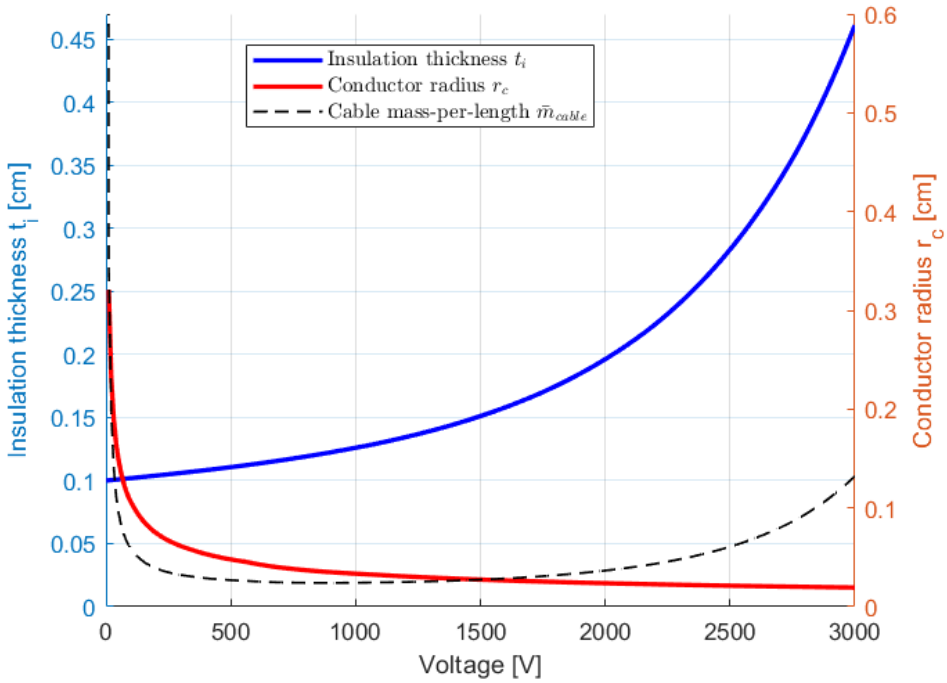

Figure 3.11: Example of conductor and insulator thickness and mass-per-length values for 1000 W.

Here it is possible to clearly see the correlation between the insulation layer and the conductor radius: the first increase rapidly with the voltage, while the latter decreases as the voltage increase, but very slowly for higher voltage. This reflects in a $\bar{m}_{cable}$ increase even if the density of the insulation layer is eight times smaller than the conductor. It is possible to localize a minimum voltage to minimize the required mass-per-length value for a certain power.

In Figure 3.12, this effect is progressively dampened as the power demand increases over the same voltage range.

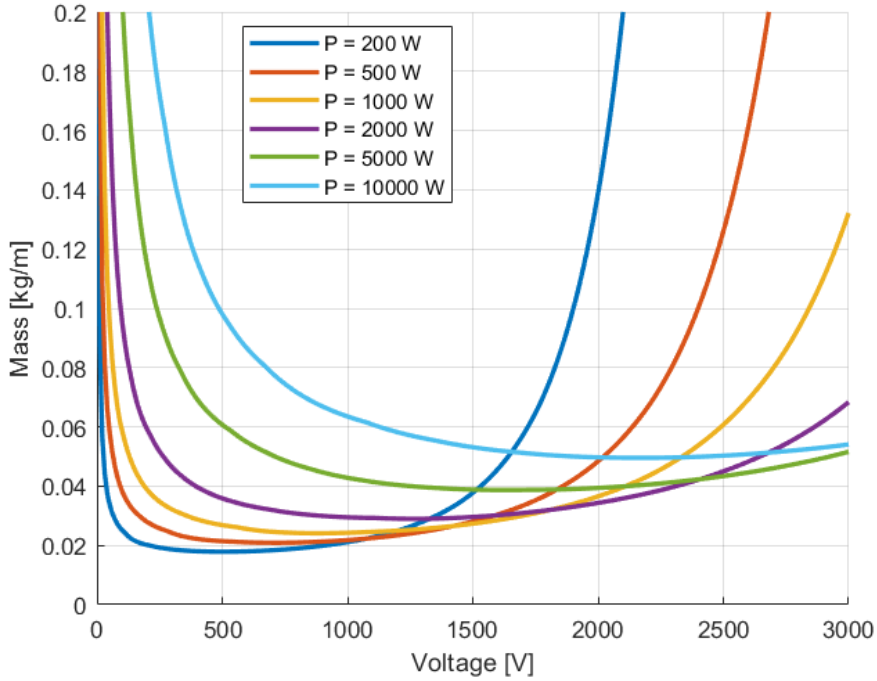

Figure 3.12: $\bar{m}_{cable}$ as a function of voltage and power.

To optimize the weights, a voltage between 500 and 1500 V proves to be the ideal option (for power levels on the order of kilowatts), allowing the use of a relatively low current for distribution. However, to avoid the formation of electric arcs, it would still be preferable to use the lowest possible voltage.

3.1.6 Real effects

To evaluate the battery pack performance more accurately, it is necessary to outline the complete powertrain and determine its overall efficiency by identifying the efficiency of each individual component. A typical powertrain for a battery-only electric propulsion system includes the battery pack, a $DC-DC$ converter to adjust the required voltage level, and a $DC-AC$ inverter to supply the electric motor, and the mechanical transmission that delivers torque from the motor to the driven wheels.

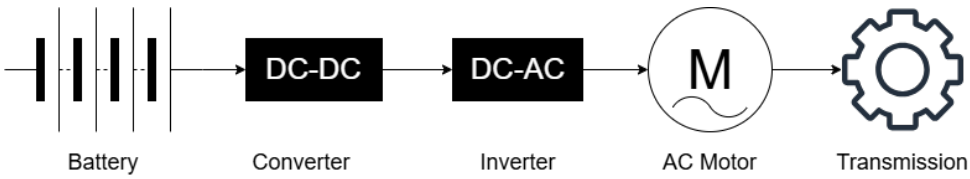

Figure 3.13: Battery power train.

Regarding the battery, the electrical efficiency is defined as

$$\eta_{el} = \frac{P_{\text{useful}}}{P_{\text{delivered}}} \tag{3.41}$$

The useful power is

$$P_{\text{useful}} = P_{\text{delivered}} - P_{\text{loss}} \tag{3.42}$$

and the losses are associated with heat generation

$$P_{\text{loss}} = Q_{gen} \tag{3.43}$$

For a given voltage, increasing the output power increases the current, which raises the ohmic losses and therefore reduces the efficiency. The typical range for a battery, therefore depends on the current, but it can be assumed to lie between 95 and 100% for a first evaluation; A more detailed value is discussed in Paragraph 3.1.9.1. For a converter, the minimum efficiency can be assumed to be around 90% [26]. The inverter efficiency, instead, is generally higher, ranging between 94 and 97% [26]. A generic electric motor has an efficiency higher than 92%, so the global efficiency before the transmission system can be estimated in Equation 3.44.

$$\eta_{\text{g}} = \eta_{\text{el}} \cdot \eta_{\text{converter}} \cdot \eta_{\text{inverter}} \cdot \eta_{\text{motor}} \tag{3.44}$$

It is possible to obtain a baseline for global efficiency as $\eta_{global} = 75\%$ and a maximum value of 90%

Other important parameters are:

- Gravimetric density;
- Volumetric density;
- Mass Packing Factor (MPF);
- End-of-Life (EoL) degradation.

The magnitude of these variables and how they affect the sizing process are now evaluated.

Mass Packing Factor

The Mass Packing Factor (MPF) can be estimated by analyzing the solutions currently available on the market and extrapolating an overall trend at different levels to project future values. A comprehensive study in this regard is presented by H. Löbberding *et al.* in [29], where an extensive analysis of system packing efficiency and cell types for battery electric vehicles is carried out, allowing the corresponding values to be derived and plotted. MPF is a fundamental parameter for assessing the structural efficiency of a battery system, since it expresses the ratio between the active cell mass and the total pack mass (including BMS for battery protection) and thus directly determines the effective utilization of the electrochemical material and the resulting system-level specific energy.

The relationship between the cell mass and the total system mass can be expressed as

$$\text{MPF} = \frac{m_{\text{cell}}}{W_{\text{pack}}} \tag{3.45}$$

where m_{cell} represents the mass of the battery cell and W_{pack} is the total mass of the battery system.

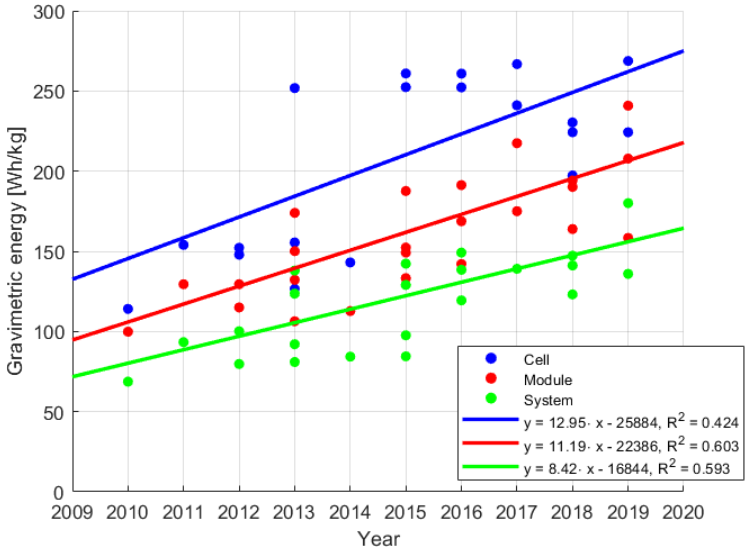

Figure 3.14: Development of the gravimetric energy density (Wh/kg) in the years between 2010 and 2019. Blue represents the development on cell level, red represents the module level, and green represents the system level [29].

From the values extracted from Figure 3.14, the linear gravimetric trends at cell and system level were obtained through regression analysis, yielding the following expressions: $Y_{\text{cell}}(x) = 12.95 \cdot x - 25884$ with $R^2 = 0.424$, and $Y_{\text{system}}(x) = 8.42 \cdot x - 16844$ with $R^2 = 0.593$, where x represents the temporal vector spanning the interval 2009-2030. The temporal gap is extended to the year 2030, extrapolating the values of Y_{cell} and Y_{system}. It is possible to express the MPF also via Equation 3.46, which defines the ratio between the gravimetric performance at cell level and that at system level. This formulation provides a better dimensionless indicator quantifying the gravimetric reduction occurring when moving from cell to system integration, thereby capturing the cumulative impact of packaging, structural components, thermal management, and auxiliary subsystems. Evaluating the MPF over the considered temporal horizon enables the assessment of how this integration penalty evolves with technological progress and whether the gap between cell and system performance tends to widen or narrow over time.

$$\text{MPF} = \frac{Y_{\text{cell}}}{Y_{\text{system}}} \tag{3.46}$$

The value tends to stabilize around 1.6 on average. However, in order to account for high-performance system solutions exhibiting improved gravimetric values as seen in figure 3.14, a correction margin of ±0.2 has been introduced around the mean value. This tolerance band allows the MPF to span a range representative of both conservative and optimized configurations. Consequently, a lower bound of approximately 1.4 is obtained, as shown in Figure 3.15.

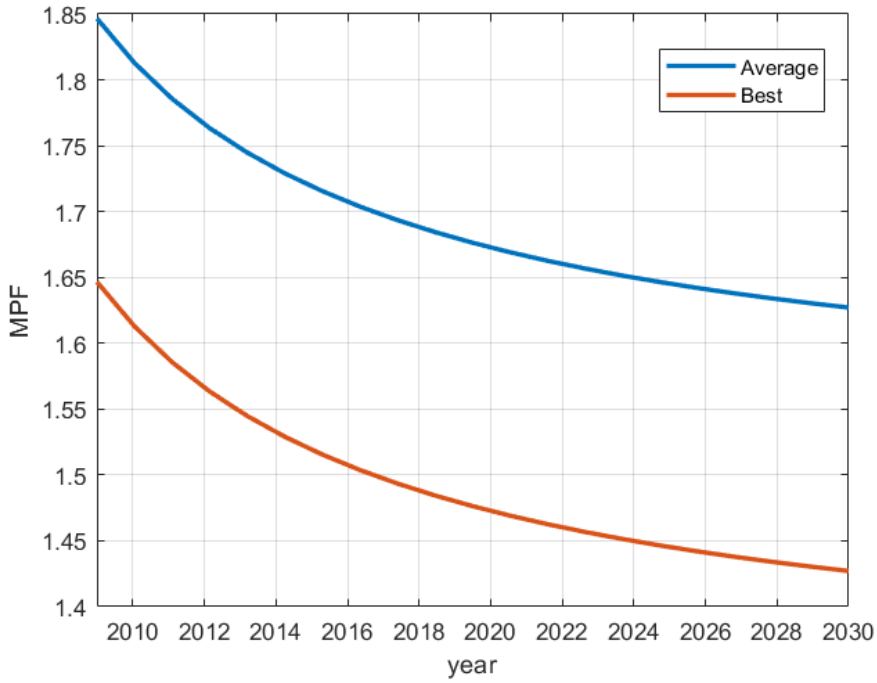

Figure 3.15: Trend of Mass Packing Factor (MPF) over time, showing the average curve representing typical system integration, and the best-case curve representing optimized architectures.

In terms of BED values, Figure 3.15 can be interpreted as an extension of Figure 3.14, incorporating the projected trends shown in Figure 3.16.

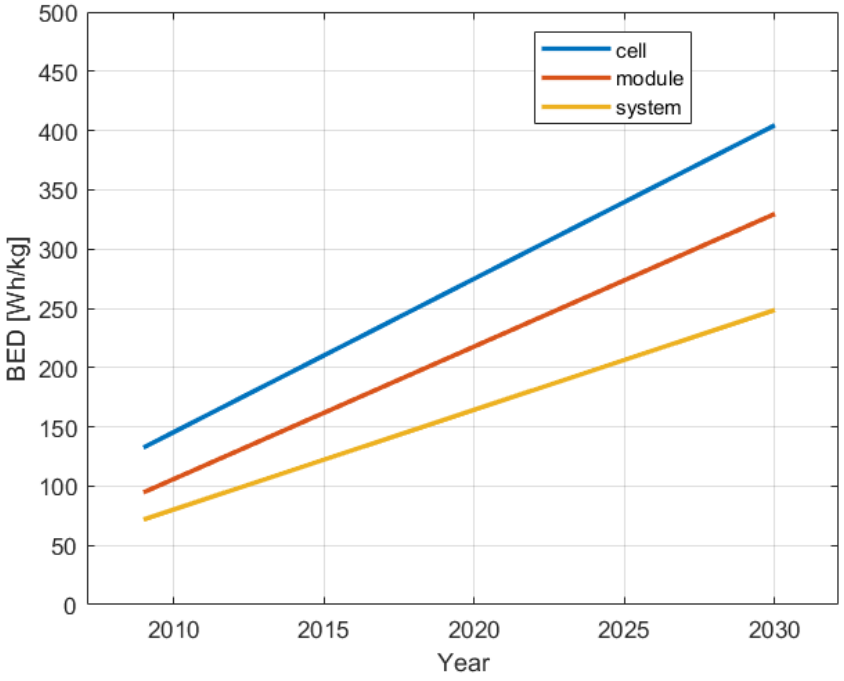

Figure 3.16: Trend of BED values at different power levels, over the expected technological progress.

Degradation

The primary cause of lithium-ion battery degradation is the occurrence of undesired side reactions that alter the chemical composition inside the cells, leading to a reduction in battery capacity. The reaction rate of such processes is highly dependent on battery temperature [33]. The Safe Operating Area (SOA) of a lithium battery in terms of temperature is typically from $-20\,°C$ to $60\,°C$, while the optimal battery temperature range is much more limited, going from $15\,°C$ to $35\,°C$. Indeed, at temperatures higher than $35\,°C$, the degradation of the Solid Electrolyte Interface (SEI) occurs. High temperature increases the loss of active material and accelerates the self-discharge, while, working at temperatures lower than $15\,°C$, the electrolyte viscosity increases, the ionic conductivity decreases and the charge transfer resistance increases.

Furthermore, at low temperatures, the rate of lithium plating increases involving an irreversible loss of active material that could also lead to dendrite formation and internal short circuits. In both cases, the battery capacity is reduced decreasing the battery pack performance [33]. The battery aging limits its energy storage and power output capability, as well as the performance of the vehicle including the cost and life span. The degradation occurs at a chemical level inside the cell involving the electrolyte, anode and cathode plates.

For the purpose of this thesis the degradation factors will not be analysed in details, but it is possible to estimate a degradation factor $degr$ of 10% for the stored energy as a first iteration [27]. A thermal model is therefore necessary to evaluate the battery behaviour, particularly in a harsh environment such as the Moon.

3.1.7 Thermal modelling

The need for reducing costs and high performances in battery systems is pushing for the use of large format cells and increasing the battery pack voltage beyond 800 V. Large battery format involves the reduction of hardware resources, and the use of high voltage will result in lighter cables (as seen previously), lower losses and faster charging speed for batteries. However, the use of large cells increases the need for robust electric safety and distributed thermal modelling [33]. Battery thermal models may be classified by several aspects, including physical meaning, spatial dimensions, and level of complexity. A general classification includes two main families:

- **Descriptive models**, where the model reproduces the physical phenomena occurring in the battery (high computational capacity required);
- **Behavioural models**, which treat the battery as a black box reproducing only the main thermal behaviour.

These models can also be divided into distributed models, where temperature and generated heat may vary continuously along the spatial dimensions, and lumped models, where the battery is decomposed in finite elements with a reference average temperature value. Both distributed and lumped models may be zerodimensional (0D) or multi-dimensional (1D, 2D, 3D), meaning that such models may contain the spatial information of temperature within the battery. The dominant mechanisms can be represented with their corresponding thermal quantities: q_g denotes the heat generation rate within the cell, q_{conv} the convective heat dissipation rate, and q_{rad} the radiative heat dissipation rate contribution [33]. The dissipation rate can be expressed as

$$q_d = q_{conv} + q_{rad} \tag{3.47}$$

These mechanisms collectively determine the internal thermal balance of the cell, which can be expressed in compact form in Equation 3.48.

$$\rho C_p \left(\frac{\partial T}{\partial t} + \mathbf{v} \nabla T \right) = \nabla \cdot (\kappa \nabla T) + q_g + q_d \tag{3.48}$$

where ρ is the cell material density, C_p the specific heat capacity, κ the thermal conductivity, T the temperature field, t the time and $\mathbf{v}$ the velocity of the liquid phase [33].

The term $\nabla \cdot (\kappa \nabla T)$ describes the transfer rate of thermal energy inside the battery due to temperature gradient, q_g accounts for the heat generation rate within the cell, while q_d denotes the heat dissipated toward the external environment. The term $\rho C_p \left(\frac{\partial T}{\partial t} \right)$ expresses the rate of heat accumulation inside the battery, and $\rho C_p \, \mathbf{v} \nabla T$ corresponds to the convective heat transfer rate associated with electrolyte motion. This convective contribution is generally considered negligible under typical operating conditions.

3.1.7.1 Ambient temperature influence on cell performance

For this analysis, the battery temperature will be assumed to be in equilibrium with the ambient temperature; therefore, heat generation and dissipation terms will not be considered. To evaluate the effects of ambient temperature on battery performance, it is necessary to identify the key parameters of the Shepherd model, namely E_0, K, and A. Once these parameters have been identified, they're analysed in order to determine how they vary as a function of temperature.

Here are visualized typical curves for each parameter:

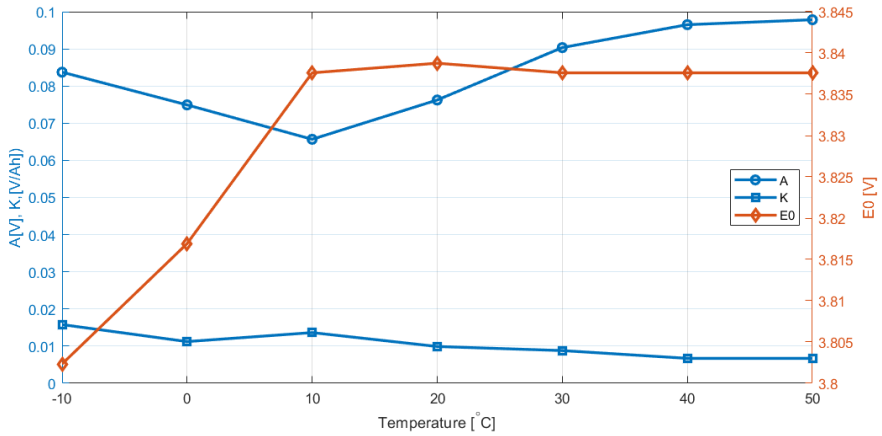

Figure 3.17: Main Shepherd's cell parameters variation [21].

From these values, assuming that these trends are generally valid for lithium-based batteries, the same curves can be defined for different batteries by shifting them according to the reference value measured at 25 $°C$. With these values, discharge curves at different temperatures can be plotted, allowing the battery performance to be evaluated. For this purpose, a generic li-ion cell will be used as a case study, whose characteristics have been derived from state of the art cells and are listed in Table 3.3.

Table 3.3: Case study cell characteristics.

Parameter	Value	Unit
V_{nom}	3.7	V
V_{full}	3.9	V
Q	2.5	Ah
R	0.03	Ω

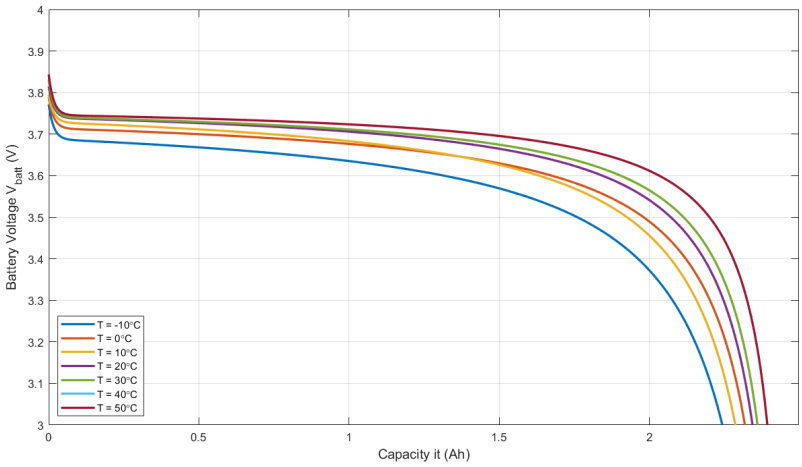

Figure 3.18: Discharge curves at different temperatures.

It can be observed that as the temperature decreases, the battery performance rapidly declines, whereas increasing the temperature leads to improvements. These effects are related to changes in the chemical processes occurring within the battery: lowering the temperature slows down these processes, while raising it accelerates them. High temperatures, however, while offering better performance, increase the rate of degrading processes, thus rapidly reducing the operational lifetime of the battery.

The optimal temperature for li-ion a battery $T_{ref,b}$ is around $20\,°C$; deviating significantly from this value compromises battery lifespan, so higher temperatures provide only short-term performance gains. It is possible to further extend the evaluation at lower temperatures, as expected on the Moon, with a linear extrapolation of the parameters curves as seen in Figure 3.19.

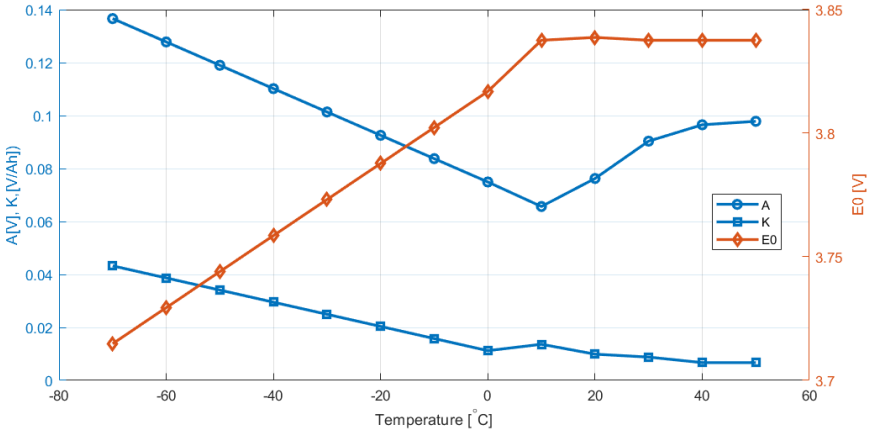

Figure 3.19: Main Shepherd's parameters linear interpolation.

As expected, for lower temperatures the parameters associated with polarization effects (A and K) increase, explaining the degrading effects displayed in Figure 3.20 and discussed in section 1.3.1, while open circuit voltage decrease.

It is now possible to visualize the effects on the discharge curves in Figure 3.20.

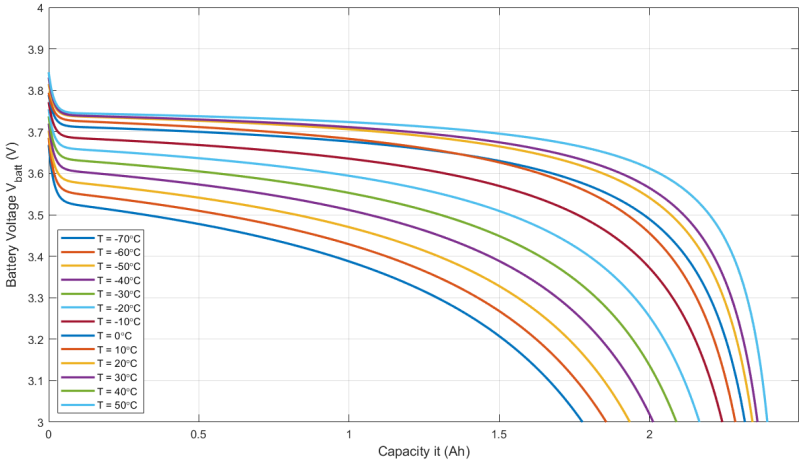

Figure 3.20: Discharge curves at lower temperatures.

As expected, the performance rapidly decrease reducing the capacity of about 30% at cut-off voltage ($V_{cut} = 3V$).

3.1.7.2 Cell thermal model

Knowing how the battery performance varies with external temperature, it is now important to evaluate how the battery heats up during its operation, in order to more accurately determine the operating temperature and, consequently, its performance. To determine which model is better to describe the thermal behaviour of a battery operating on a lunar environment is necessary to evaluate the expected temperature gradients, the characteristic heat transfer mechanisms, and the relevant spatial and temporal scales that govern heat generation and dissipation under such extreme conditions. When the internal temperature gradients are small, the battery can be modeled with a single internal heat capacitance, assuming a uniform internal temperature $T = T(t)$. This is defined as a zero-dimensional (0D) lumped thermal model [33].

A uniform internal temperature distribution can be assumed when

$$\mathrm{Bi} = \frac{h_\mathrm{c} \cdot L}{\kappa} \ll 1 \tag{3.49}$$

The Biot number Bi depends on the thermal conductivity of the sample κ, the sample dimension L, and the convective heat transfer coefficient of the surrounding fluid h_c. The condition $Bi \ll 1$ indicates that the internal conduction resistance is much smaller than the surface convection resistance, making internal temperature gradients negligible [33]. This method is therefore applicable because h_c on the Moon is neglectible since there's practically no atmosphere, thus the Biot number is $\ll 1$.

The thermal behaviour of the battery cell is described using a lumped-parameter 0D energy balance, under the assumption of spatially uniform temperature within the control volume. The governing equation reads

$$W_b \cdot C_p \frac{dT_{int}}{dt} = Q_g + Q_d \tag{3.50}$$

where W_b is the mass of the cell, C_p is the specific heat capacity at constant pressure, T_{int} is the internal temperature, Q_g represents the internally generated heat and Q_d accounts for heat dissipation toward the surrounding environment.

Introducing the equivalent thermal capacitance of the system,

$$C_\mathrm{th} = W_b \cdot C_p \tag{3.51}$$

the energy balance can be conveniently rewritten as

$$C_\mathrm{th} \frac{dT_{int}}{dt} = Q_\mathrm{tot}, \qquad Q_\mathrm{tot} = Q_g + Q_d \tag{3.52}$$

The internal heat generation term is expressed in Equation 3.53 according to the Bernardi formulation, which accounts for irreversible Joule losses and reversible entropic effects.

$$Q_g = i \left(E_0 - V_\mathrm{cell} + T_{int} \frac{dU}{dT} \right) + i^2 R_c \tag{3.53}$$

where i is the cell current (positive during discharge), E_0 is the open-circuit voltage, V_cell is the terminal voltage, $\frac{dU}{dT}$ is the reversible entropic heat of the cell (U is the equilibrium potential of the cell expressed in Volt, T is the internal temperature) and $i^2 R_c$ is the heat generation due to contact resistance. The reversible entropic heat contribution, represented by the term $i \cdot T_{int} \frac{dU}{dT}$ in the heat generation model is identified as a function of the state of charge (SOC) based on the work of Christophe Forgez *et al.* [16].

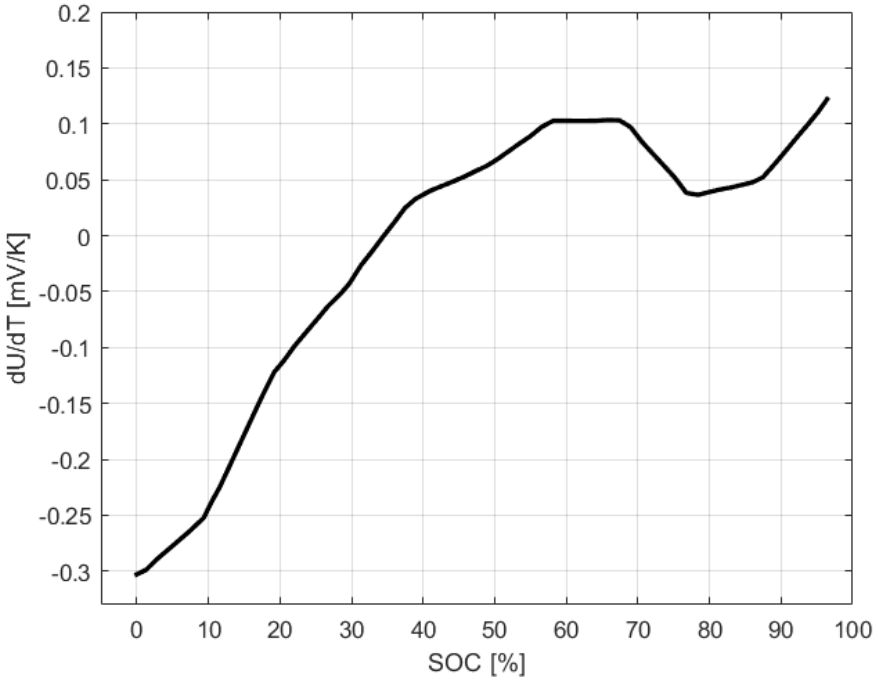

Figure 3.21: Reversible entropic heat contribution [16].

Heat dissipation toward the ambient environment is modeled by convective and radiative heat transfer mechanisms:

$$Q_d = -h_c A_{surf} \left(T_{\text{surf}} - T_{amb}\right) - \varepsilon \sigma_{SB} A_{surf} \left(T_{\text{surf}}^4 - T_{amb}^4\right) \tag{3.54}$$

where h_c is the convective heat transfer coefficient, A_{surf} is the external surface area of the cell, T_{surf} is the surface temperature, T_{amb} is the ambient temperature, ε is the surface emissivity, and σ_{SB} is the Stefan-Boltzmann constant. The value of h_c is set to zero because in lunar environment there's no atmosphere and despite the rover will be pressurized it is assumed thet the battery compartment is not, hence thermal convection is omitted in the output. Assuming a lumped thermal model with a Biot number $\text{Bi} \ll 1$, internal temperature gradients are negligible and the surface and internal temperatures can be considered equal.

$$T_{\text{surf}} \simeq T_{\text{int}} = T \tag{3.55}$$

Substituting the expressions of Q_g and Q_d into the energy balance yields the following non-linear ordinary differential equation governing the thermal dynamics of the cell:

$$C_{\text{th}} \frac{dT}{dt} = i \left(E_0 - V_{\text{cell}} + T \frac{dU}{dT}\right) + i^2 R_c - h A_{surf} \left(T - T_{amb}\right) - \varepsilon \sigma_{SB} A_{surf} \left(T^4 - T_{amb}^4\right) \tag{3.56}$$

The physical meaning of each term in the heat balance is summarized in Table 3.4.

Table 3.4: Thermal model governing equations at cell level.

Quantity	Equation
Reversible heat	$Q_{\text{rev}} = i\,T\,\dfrac{dU}{dT}$
Irreversible heat	$Q_{\text{irr}} = i\,(E_0 - V_{\text{cell}})$
Total heat generated	$Q_g = Q_{\text{rev}} + Q_{\text{irr}} + i^2 R_c$
Convective heat	$Q_{\text{conv}} = -h_c A_{\text{surf}}(T - T_{\text{amb}})$
Radiative heat	$Q_{\text{rad}} = -\varepsilon\sigma_{SB} A_{\text{surf}}(T^4 - T_{\text{amb}}^4)$
Total heat dissipation	$Q_d = Q_{\text{conv}} + Q_{\text{rad}}$

For numerical implementation, the differential equation is discretized in time using an explicit Euler scheme. Approximating the time derivative as

$$\frac{dT}{dt} \approx \frac{T^{i+1} - T^i}{\Delta t} \tag{3.57}$$

the discrete time evolution of the internal temperature is obtained

$$T(i+1) = T(i) + \frac{\Delta t}{C_{\text{th}}}\, Q_{\text{tot}}(i) \tag{3.58}$$

where $\Delta t = t_{i+1} - t_i$ is the time and C_{th} is the thermal capacitance defined in Equation 3.51.

3.1.8 Validation

In order to validate the model, the results obtained were compared with those reported by L. H. Saw *et al.* [39]. A correction of the nominal capacity is introduced through a power-law relationship to account for the rate-dependent behavior of the battery. A coefficient $p_k = 1.1$ is assumed, representing the Peukert exponent, which quantifies the deviation from ideal capacity at different discharge rates [39]. The peukert coefficient varies with temperature and cycles [34], but for the purpose of this thesis it has been assumed constant. The reference capacity is set as $C_{\text{ref}} = Q$. For each C_{rate} considered identified as C_{case}, the effective battery capacity is obtained via equation 3.59

$$Q_{eff} = Q\left(\frac{C_{\text{ref}}}{C_{case}}\right)^{p_k - 1} \tag{3.59}$$

This formulation derives from Peukert's law, which models the reduction of available capacity as discharge current increases. Since $p_k > 1$, when C_{case} exceeds the reference value C_{ref}, the term $\left(\frac{C_{\text{ref}}}{C_{case}}\right)^{p_k - 1}$ becomes smaller than unity, leading to a reduced effective capacity Q_{eff}. Conversely, at lower discharge rates, the effective capacity approaches the nominal value Q [39]. This correction enables a more realistic estimation of battery performance under varying C-rates, particularly for high-power applications. The battery cell parameters used for this purpose are reported in Table 3.5.

Table 3.5: Reference battery cell parameters [39].

Parameter	Symbol	Value	Unit
Nominal voltage	V_{nom}	3.0	V
Capacity	Q	1.3	Ah
Cell mass	W_b	0.040	kg
Density	ρ	2700	kg m^{-3}
Cathode material	–	$LiFePO_4$	–
Anode material	–	Graphite	–
Cell length	h_s	0.065	m
Cell diameter	d_s	0.018	m
Specific heat capacity	C_p	900	$\text{J kg}^{-1}\text{ K}^{-1}$
Stefan-Boltzmann constant	σ_{SB}	5.67e-8	$\text{W m}^{-2}\text{ K}^{-4}$
Internal resistance	R	0.03	Ω
Reference temperature	$T_{ref,b}$	25	$^{\circ}C$
Emissivity	ε	0.95	–
Heat transfer coefficient	h_c	8	$\text{W m}^{-2}\text{ K}^{-1}$

The referenced study uses various constant discharge currents to evaluate the thermal response according to the applied load; in particular, currents of 1C, 2C, and 3C are applied, expressed in terms of C-rate as defined in Equation 3.2 which the study [39] refers to as ”It-rates”.

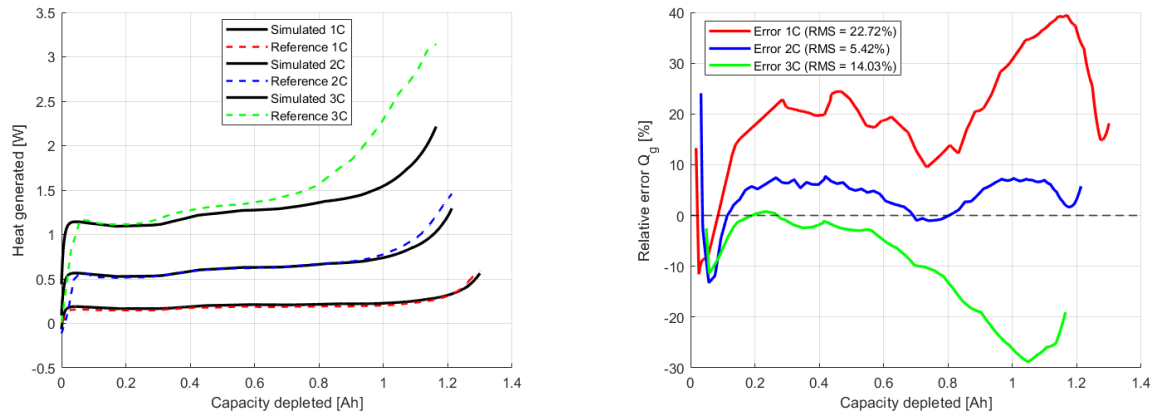

(a) **(b)**

Figure 3.22: Simulation validation.

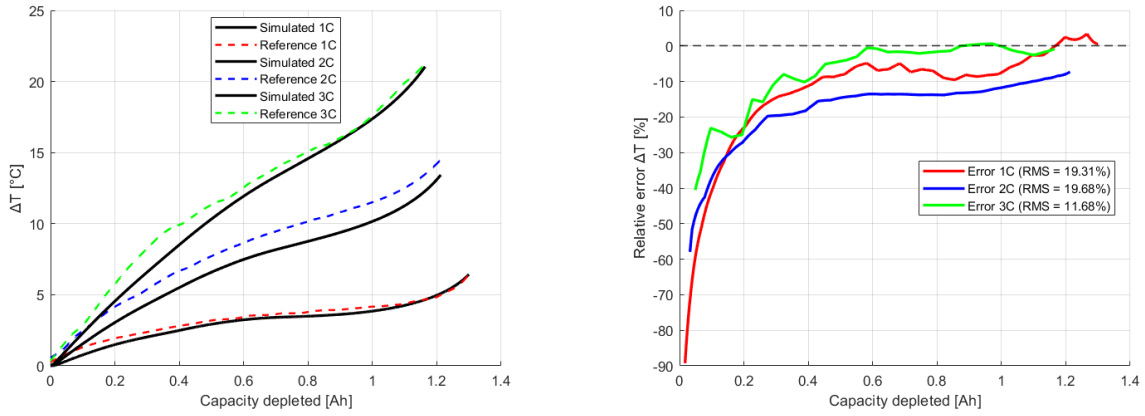

(a) **(b)**

Figure 3.23: Comparison between the temperature raise predicted by the model and the reference values.

The comparison between the present results and those reported by L. H. Saw *et al.* [39] shows an overall good agreement in terms of temperature rise, while larger discrepancies are observed for the peak heat generation, especially at low C-rates. These discrepancies can be explained by some modelling assumptions and parameter definition. In particular, the contact resistance R_c has been assumed to be equal to R, this may affect the accuracy of the heat generation prediction. For a better understanding of the model's fidelty the absolute errors are reported in Figure 3.24.

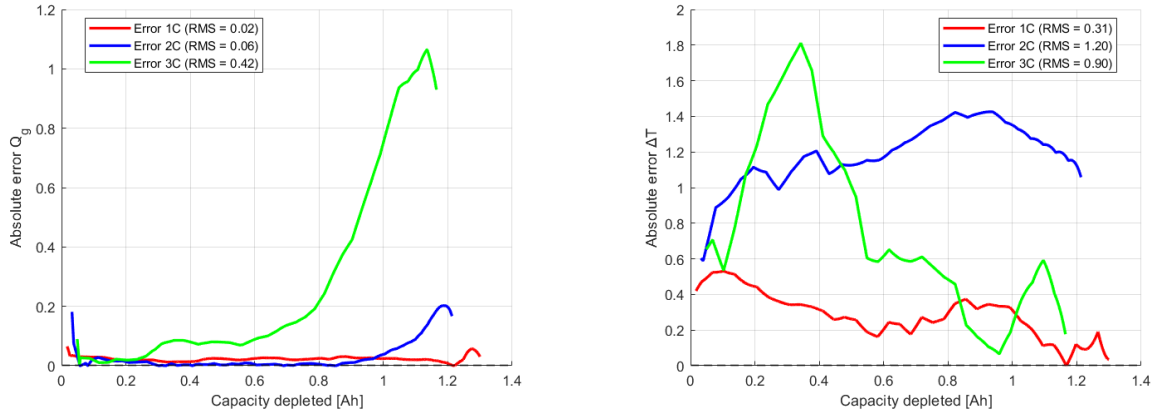

(a) **(b)**

Figure 3.24: Absolute error analysis: (a) heat generation Q_g error; (b) temperature variation ΔT error.

As shown in Figure 3.24, the largest absolute error occurs at the 3C discharge rate, whereas for lower current rates the model exhibits improved accuracy. A similar trend is observed for the temperature prediction: the discrepancy increases at higher currents (2C and 3C), while at 1C the mean error is approximately 0.33 °C. An error on the order of 1 °C can be considered acceptable for a first-order approximation.

3.1.9 Battery pack thermal model

The model developed for a single cell is not sufficient; therefore, it is necessary to extend the analysis to the entire battery pack. To this end, the already validated electrical model is employed, modifying the electrical parameters according to the required energy demand, by identifying the number of cells connected in series n_s and the number of modules connected in parallel m. The heat generated by a single cell is multiplied by n_s composing each battery module, since Q_g depends on the voltage drop across the cells while the discharge current remains the same through all series-connected elements. Since every module can be considered independent from one another, each module reach the same temperature, therefore the battery pack temperature is the battery module temperature. The dissipated heat is not scaled by n_s, since the parameter that changes from the cell level to the pack level is the total surface area $A_{surf,pack}$. The convective heat transfer term is neglected, since the modules are located in the unpressurized section of the rover and, given that the lunar environment is devoid of atmosphere, the convective heat transfer coefficient h_c is null.

This formulation inherently assumes that all cells within the battery pack are subject to the same thermal cycle, with uniform heat generation and reaching the same temperature. Such an assumption is deemed acceptable provided that an effective thermal management system ensures the same boundary conditions for every cell.

The model accounts for the temporal evolution of the temperature as well as for the thermal effects on the electrical parameters resulting from changes in the battery temperature itself as seen in paragraph 3.1.7.1. These parameters inevitably affect the battery mass and surface area and, consequently, the maximum temperature reached during operation. The analysis aims to determine the optimal voltage that minimizes mass, volume, and temperature rise, while also highlighting the effects introduced by variations in the Battery Energy Density (BED) once the optimal voltage has been defined while maintaining the same material density (kg/m^3) for the cell.

Table 3.6: Thermal model governing equations at system level.

Quantity	Equation
Reversible heat	$Q_{\text{rev}} = i\,T_{int}\,\dfrac{dU}{dT}\,n_s$
Irreversible heat	$Q_{\text{irr}} = i\,(E_0(T) - V_{\text{cell}})\,n_s$
Total heat generated	$Q_{\text{g,pack}} = Q_{\text{rev}} + Q_{\text{irr}} + i^2 R_c$
Radiative heat	$Q_{\text{rad,pack}} = \varepsilon\,\sigma_{\text{SB}}\,A_{\text{surf,pack}}\,(T^4 - T_{\text{amb}}^4)$
Net heat balance	$Q_{\text{tot}} = Q_{g,pack} - Q_{\text{rad}}$

3.1.9.1 Optimal voltage identification

To identify the optimal voltage, the characteristics of the cell used in the thermal model validation were considered, with a fixed BED value of $106.6\,Wh/kg$.

A fundamental parameter in the thermal modelling of the battery pack is the total external surface area, as it directly governs the heat rejection capability of the system. In the present configuration, natural heat dissipation is assumed to occur exclusively by thermal radiation. Consequently, a larger exposed surface area enhances radiative heat transfer, thereby limiting the net heat accumulation within the pack and reducing the temperature reached during operation.

To estimate the total surface area $A_{\text{surf,pack}}$, a first iterative layout is defined by adopting a simplified electrical arrangement: cells are connected in series along one direction to increase the overall voltage, and placed side-by-side in the orthogonal or vertical direction to increase the total capacity (i.e., parallel branches), providing an initial estimate of the pack arrangement and corresponding radiating surface area.

Once an area compatible with both thermal dissipation requirements has been identified, along with the corresponding voltage for mass optimization, the internal arrangement of the cells can be refined. Specifically, the cells will be reorganized into a more spatially optimized configuration in the three dimensions ($l \times h \times w$), while maintaining the total external surface area within the the previous defined constraints, thus preserving the desired thermal performance. This allows the total pack surface area, $A_{\text{surf,pack}}$, to be calculated accordingly. The total number of cells in the pack is fixed and denoted as tot_{cells}, while n_s and m represent respectively the number of series and parallel branches. The total cell count is therefore obtained in Equation 3.60.

$$tot_{cells} = n_s \cdot m \tag{3.60}$$

The only variation concerns the interconnection configuration among the cells, which is modified to increase or decrease the overall pack voltage and total capacity by defining the number of cells connected in series and parallel. By this initial formulation, the pack dimensions are approximated to achieve a square layout for the modules in Table 3.7.

Table 3.7: Geometrical dimensions of the battery pack.

Description	**Formula**
Battery pack length	$l = h_s \cdot n_s$
Battery pack height	$h = d_s \cdot \sqrt{m}$
Battery pack width	$w = h$

Where h_s and d_s are the cell height and depth, respectively. For a standard 18650 cylindrical cell, these parameters are approximately $h_s = 65\,\text{mm}$ and $d_s = 18\,\text{mm}$. The total surface area of the battery pack is estimated via Equation 3.61.

$$A_{\text{surf,pack}} = 4\,l\,h + 2\,h^2 \tag{3.61}$$

and the corresponding volume.

$$V_{\text{pack}} = l \cdot h \cdot w \tag{3.62}$$

Finally, the total pack weight is calculated as

$$W_{\text{pack}} = W_b \cdot tot_{cells} \cdot \text{MPF} \tag{3.63}$$

where W_b is the weight of a single cell form Table 3.5 and MPF is the mass packing factor discussed previously and set to 1.4.

For preliminary evaluation it is necessary to establish some operating conditions such as power required P_r and operative time t_r. P_r is set to $5000\,W$ and t_r is set to $12\,hours$. For the total battery system mass estimation, a total cable length of 10 meters is assumed.

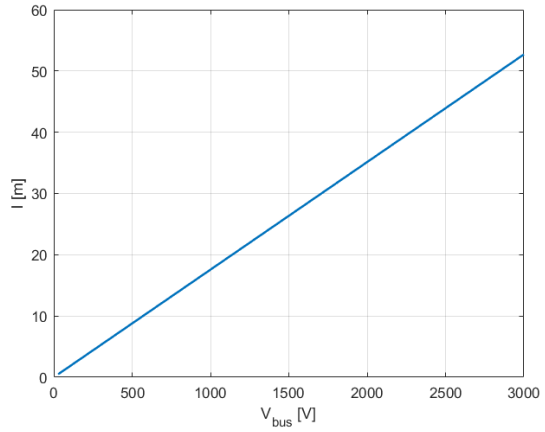

(a) l

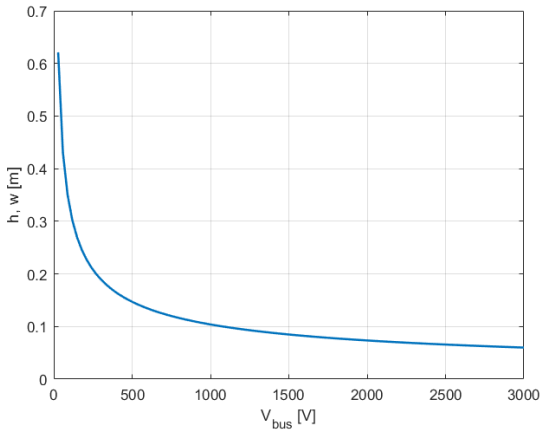

(b) h, w

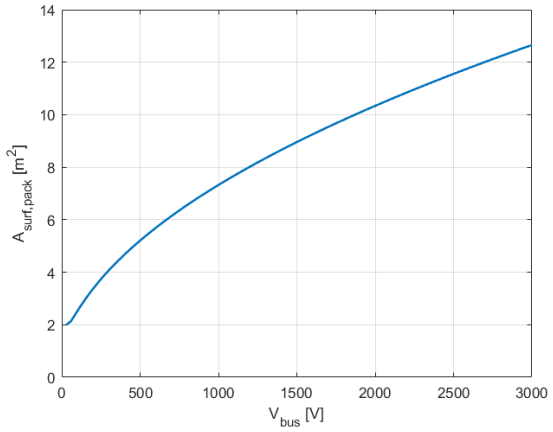

(c) $A_{surf,pack}$

Figure 3.25: Trend of the pack dimensions and external surface area as a function of V_{bus} in the initial configuration of Table 3.7.

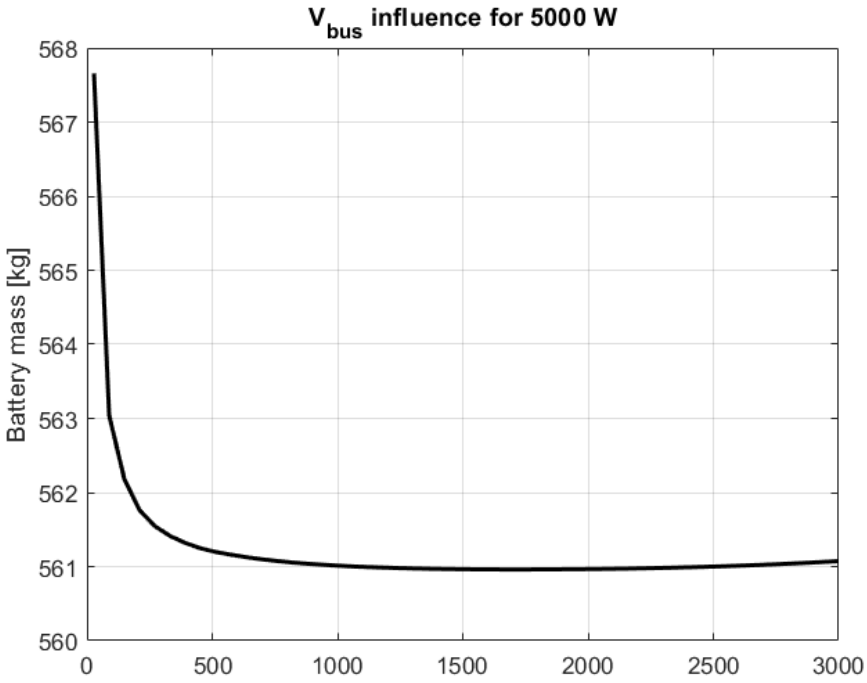

Figure 3.26: Total battery pack mass as a function of V_{bus} and power comprehensive of cable mass.

In Figure 3.26 it is possible to notice a reduction in weight for increasing voltage until 1000 V where it becomes stable, then at around 3000 V the weight start to rise; this behaviour is due to the cable mass weigth as seen in its dedicated section, because the battery pack only mass is constant for a given energy requirement. The optimal voltage value will be investigated over a range spanning from 28 V to 3000 V, and for thermal analysis different cases will be considered by varying ambient temperature T_{amb}.

Thermal analysis at different ambient temperatures

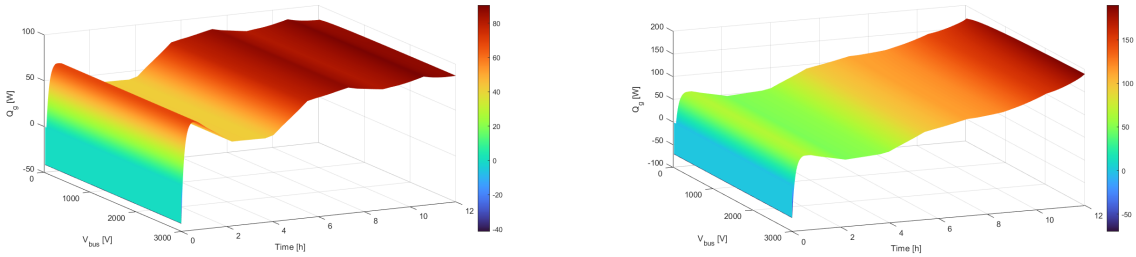

(a) $T_{amb} = +20°C$ **(b)** $T_{amb} = -20°C$

Figure 3.27: Generated heat as a function of V_{bus}, time and power for different ambient temperatures.

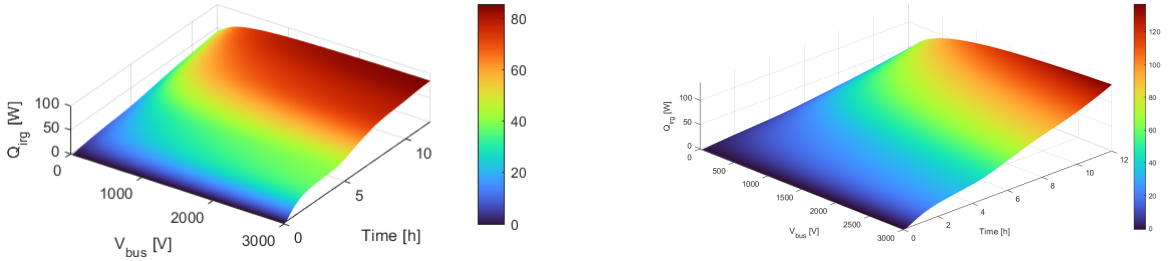

(a) $T_{amb} = +20°C$ **(b)** $T_{amb} = -20°C$

Figure 3.28: Radiated heat as a function of V_{bus}, time, surface area and power for different ambient temperatures.

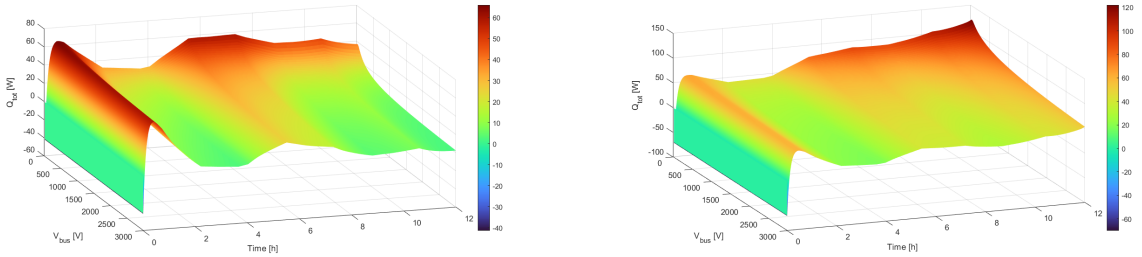

(a) $T_{amb} = +20°C$ **(b)** $T_{amb} = -20°C$

Figure 3.29: Total heat flow as a function of V_{bus}, time, surface area and power for different ambient temperatures.

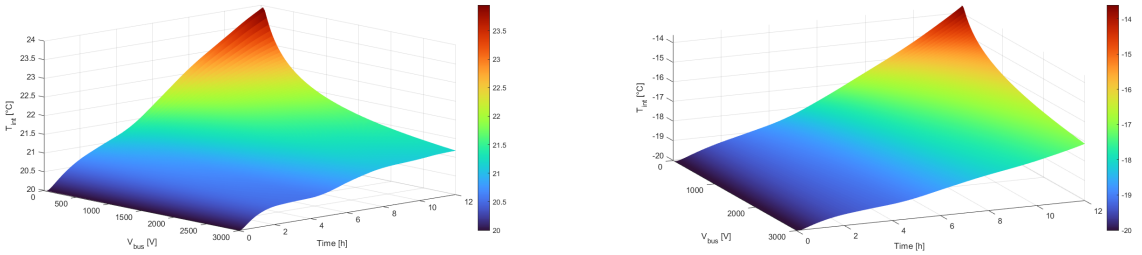

(a) $T_{amb} = +20°C$ **(b)** $T_{amb} = -20°C$

Figure 3.30: Battery pack temperature as a function of V_{bus}, time, surface area and power for different ambient temperatures.

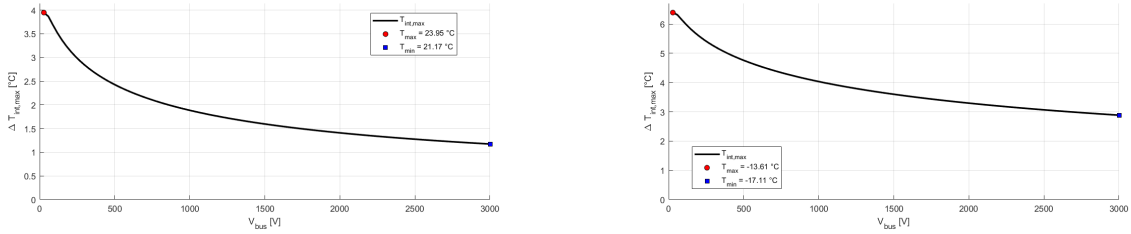

(a) $T_{amb} = +20°C$ **(b)** $T_{amb} = -20°C$

Figure 3.31: Maximum temperature increase profile as a function of V_{bus}, surface area and power for different ambient temperatures.

Figure 3.31 indicate that lower ambient temperatures are associated to higher temperature increases, from $\Delta T_{max} \approx 4\,°C$ at $20\,°C$ to $\Delta T_{max} \approx 6.5\,°C$ at $-20\,°C$.

From a purely thermal perspective, the larger the external surface area, the lower the maximum temperature rise $\Delta T_{\max}$ reached by the battery pack, as represented in Figure 3.31. However, an excessively large area can become problematic in terms of total space occupancy, particularly along at least one direction of the battery pack. Therefore, it is assumed that the pack will conform to the available volume assumed in Figure 3.32, roughly corresponding to the floor of a conceptual pressurized rover, which has a cylindrical shape with hemispherical end caps, and the battery pack lies along the plane intersecting the cylinder. Being a heavy subsystem it will be assumed to be placed in the floor, as a result, the pack can be relatively long in one direction (X), moderately wide (Y), and low in height (Z), while remaining fully enclosed within the rover envelope. Following the formulation the subsystem floor height has been fixed at $50\,cm$, obtaining the other dimensions consequently.

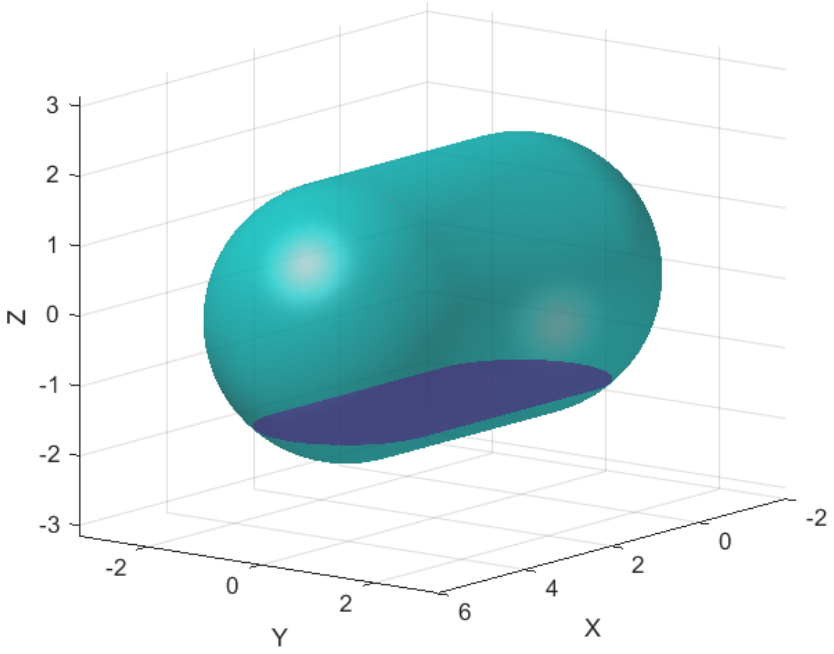

Figure 3.32: Example of a conceptual visualization of a pressurized rover, with a plane intersecting the rover habitat to highlight a subsystem volume underneath with the following dimensions: $L = 6.633$ m in the $\hat{\mathbf{x}}$ direction, $W = 2.633$ m in the $\hat{\mathbf{y}}$ direction, and $H = 0.50$ m in the $\hat{\mathbf{z}}$ direction. That for a 4 meters wide and 8 meters long rover.

The total available volume is therefore $V_{bay} = 6.6\,m^3$. A preview of the occupied volume for the battery pack can be evaluated by processing different values of volumetric density $[Wh/L]$ and energy requirements to directly visualize the effect of the volumetric density and evaluate the percentage of the occupied volume compared to V_{bay}.

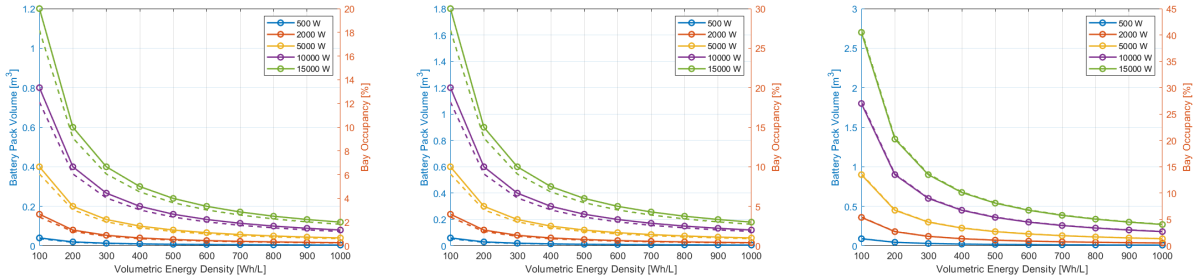

(a) 8 h **(b)** 12 h **(c)** 18 h

Figure 3.33: Battery volume (bold lines) and bay occupancy percentage (dotted lines) as a function of volumetric energy density for different operating durations and power.

In Figure 3.33 the percentage of occupied volume is represented and is clear that for today's technologies and energy requirements investigated, the battery pack can occupy up to 10% ($0.66\,m^3$) of the available space V_{bay}. Given these values, one could consider imposing a limitation on the package dimensions along the three axes. The constraints are listed in Table 3.8, introduced to maximize the total surface area and reduce ΔT_{max} while not taking too much space.

Table 3.8: Battery pack dimensional limits along each axis.

Dimension	Limit	Fraction of Nominal	Comment
Length L	1.327 m	20% of nominal	X-axis constraint
Width W	2.106 m	80% of nominal	Y-axis constraint
Height H	0.350 m	70% of nominal	Z-axis constraint

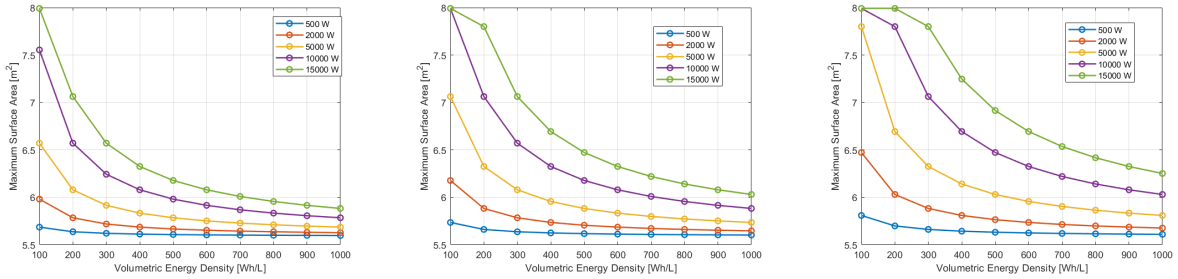

(a) 8 h **(b)** 12 h **(c)** 18 h

Figure 3.34: Battery maximum surface area as a function of volumetric energy density for different operating durations and indicated constraints.

Figure 3.34 shows the maximum area for the indicated constraints in Table 3.8, finding a value of $6\,m^2$ as a final trade-off for a required power of $5000\,W$ operating for 12 hours. By comparing Figure 3.26, Figure 3.34, and Figure 3.31, it is possible to determine the optimal design parameters: the ideal system voltage from Figure 3.26 (in the range 330-500 V), the pack area from Figure 3.34 to minimize thermal effects, and a reference value for volumetric energy density of 600 Wh/L from Figure 3.31 to minimize the system volume. Once these ranges has

been identified, the effects on mass and temperature of key parameters, such as gravimetric energy density, can be further evaluated.

BED influence at system level on mass and temperature

This analysis is crucial for future implementations, in fact, the BED values considered span from 100 to 700 Wh/kg, a very high number for the system level, but directly linked to the future and useful for wider considerations. The voltage used is set to 330 V, to minimize the risk of electrical arcing, and the surface area to radiate heat is set to 6 m^2. The battery pack density is considered constant and equal in every configuration of volumetric power density.

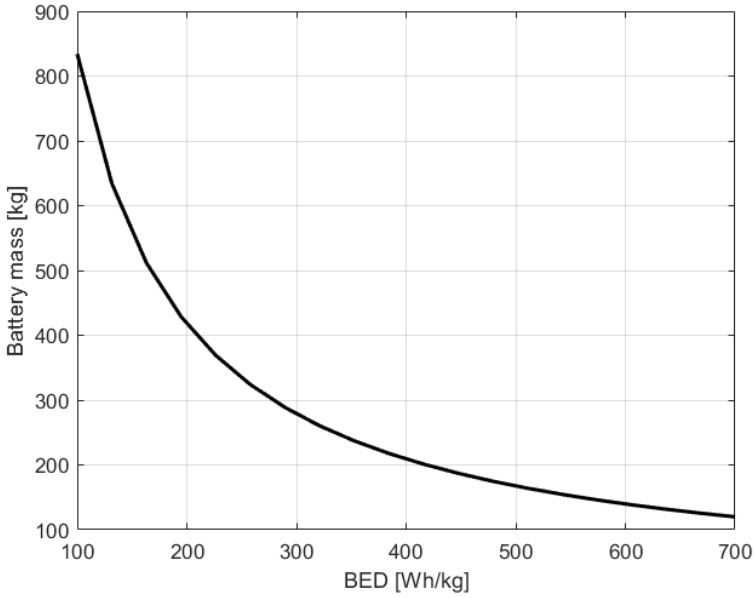

Figure 3.35: Battery pack mass variation as a function of BED for a 83.33 kWh configuration.

The obvious effect of increasing BED values is the mass reduction. Displayed in Figure 3.35, the mass follows a hyperbolic curve rapidly decreasing in value.

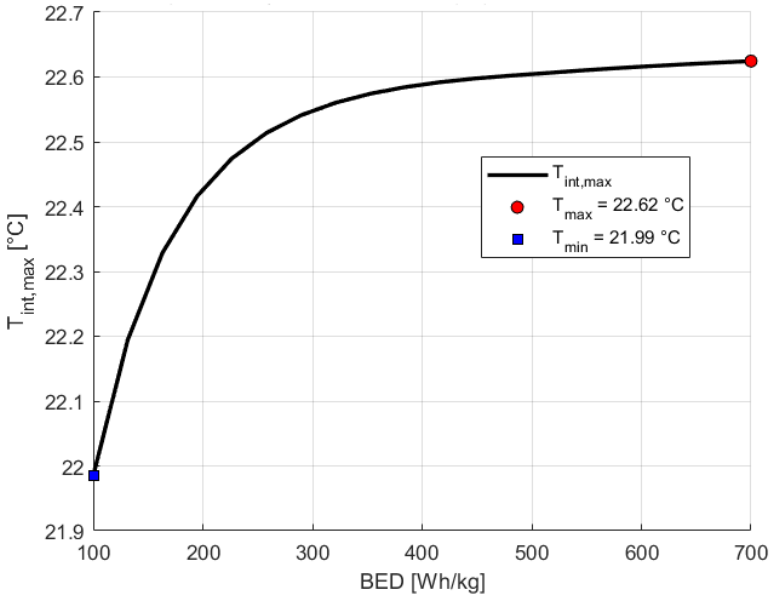

Figure 3.36: $T_{int,max}$ variation as a function of BED for a 83.33 kWh configuration.

The maximum temperature reached tends to stabilize after BED values around 350 Wh/kg, highlighting a worsening situation in terms of heat generated. This effect is due to the reduction of the thermal capacity of the battery pack by the decreasing trend of the total mass, in fact, in Figure 3.37 this phenomenon is represented.

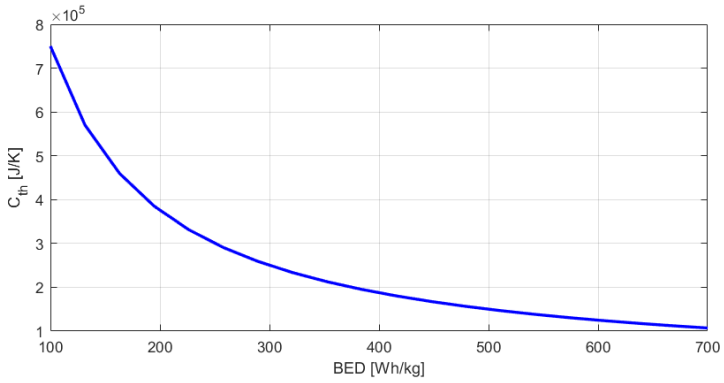

Figure 3.37: Battery pack thermal capacity C_{th} variation as a function of BED.

A BED value of 225 Wh/kg at system level results in an almost 50% reduction in the required battery pack mass compared to the initial assumptions. For further analysis, the system-level BED is conservatively set to $BED_{sys} = 225\,Wh/kg$, in line with the predictions shown in Figure 3.16, and to account for possible deviations from the expected technological progress.

Battery pack efficiency

Having obtained the parameters necessary to determine the general characteristics of the battery pack, it is possible to evaluate the pack efficiency in constant power operation.

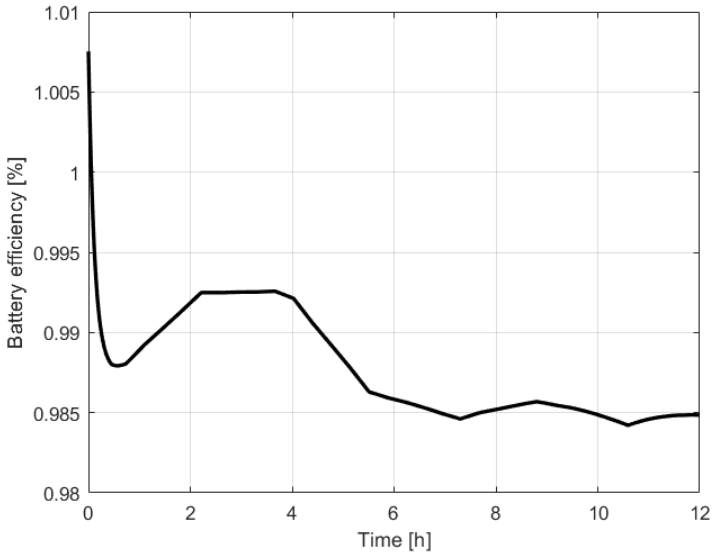

Figure 3.38: Battery efficiency for a constant power of 5000 W delivered for 12 hours.

The initial efficiency exceeding 1 is due to the initially generated heat being slightly negative, resulting in an efficiency marginally above 1. This small deviation does not significantly affect the overall evaluation of either the battery efficiency or the heat generated.

3.2 Solar arrays

Following the general introduction of solar arrays provided in the previous sections, this paragraph focuses on the development of the mathematical model adopted to describe their electrical and energetic behavior. To determine the most suitable model for the solar panel implementation, different modelling methodologies are now compared in terms of their respective advantages and limitations, and can be classified as follows:

- **Circuit-based models** [25]: These models represent the photovoltaic (PV) cell using an electrical circuit. They include:
  - Diode models (single-, double-, and triple-diode) for a single PV cell;
  - Embedded Function Blocks (EFBs), which mathematically implement the dynamic behavior of components in separate computational modules;
  - Piecewise Linear Circuit (PLC) models, where nonlinear circuit elements are approximated by linear components to simplify the analysis.
- **Equation-based methods** [25]: These methods are directly based on the mathematical equations of the PV model. They can be:
  - Analytical techniques, using optimization methods or iterative algorithms to estimate the model parameters;
  - Numerical techniques, solving the system of equations with iterative solvers such as Gauss–Seidel or Newton–Raphson methods.

While circuit-based models offer a simplified and intuitive implementation with low computational burden by using standard software libraries and linear approximations (PLC), equation-based methods demand significantly higher computational resources and implementation complexity due to the requirement of iterative numerical solvers and optimization algorithms to resolve non-linear mathematical formulations [25].

The *single-diode model* (SDM) is widely used due to its simplicity and low computational cost, as it requires only five parameters to describe the p–n junction behavior; however, it does not explicitly account for carrier recombination losses, which are better represented by the *double-diode model* [25]. The latter improves accuracy by introducing a second diode to model recombination mechanisms, although this comes with increased mathematical complexity and additional parameters [25]. For further precision, the *triple-diode model* extends the formulation by adding a third diode to capture leakage currents and grain boundary effects, making it more suitable for technologies such as multicrystalline silicon cells, but at the expense of higher computational effort and a total of nine parameters [25].

To maintain adequate physical fidelity while reducing computational cost, the single diode model represents a suitable compromise for the purposes of this thesis. For implementation the ideality factor a is assumed as a fixed parameter, while the remaining four parameters are extracted from the manufacturer's datasheet. The model is based on the equivalent electrical circuit in Figure 3.39, for the electrical modelling of the multi-junction GaAs solar cell. This model is widely used in photovoltaic analysis because it provides a good compromise between physical accuracy and computational complexity.

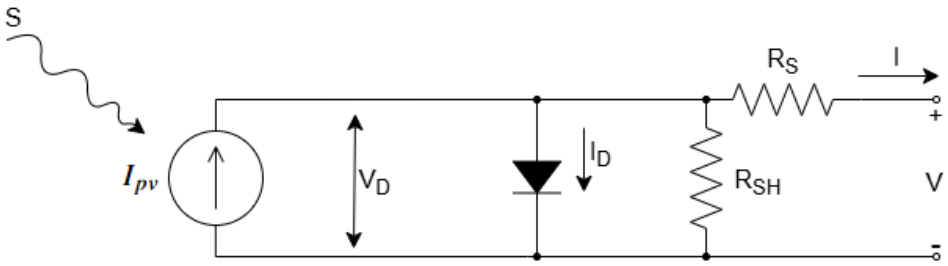

Figure 3.39: Equivalent Circuit Model (ECM) of the solar cell.

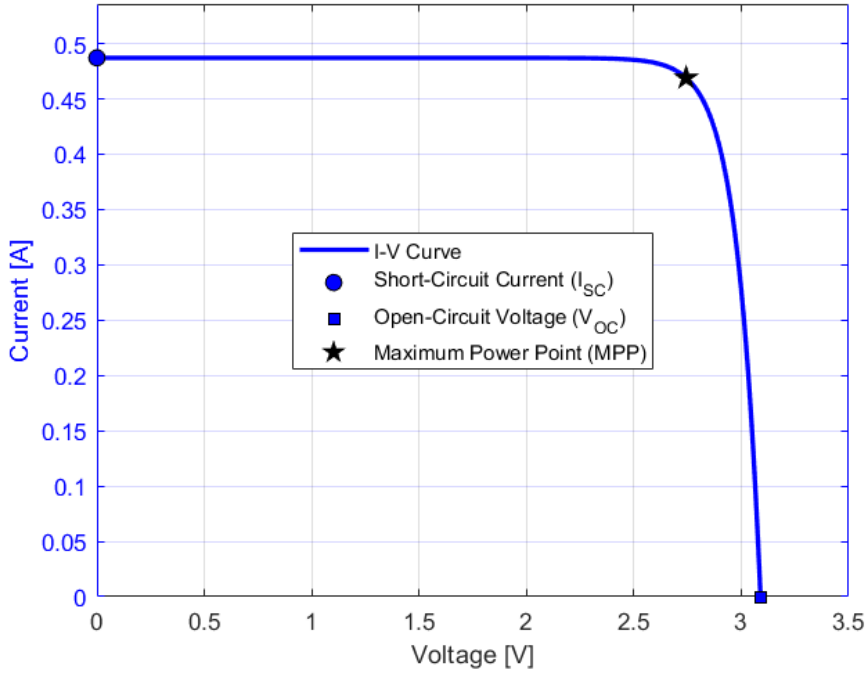

Figure 3.40: I-V curve of a solar cell. The three characteristic points (short circuit, maximum power, and open circuit points) are indicated on the curve.

The current–voltage (I-V) characteristics of the equivalent circuit consisting of one diode and two resistors (Figure 3.39) is described by Equation 3.64 [13].

$$I = I_{pv} - I_0 \cdot \left[\exp\left(\frac{V + I \cdot R_s}{aV_T}\right) - 1\right] - \frac{V + I \cdot R_s}{R_{sh}} \tag{3.64}$$

where:

- I_{pv} is the photocurrent generated by the photovoltaic effect;
- I_0 is the reverse saturation current of the diode;
- R_s is the series resistance, which accounts for losses in the cell solder bonds, interconnections, junction box, and related components;
- R_{sh} is the shunt resistance, which represents the current leakage through high-conductivity paths across the p-n junction;

- a is the ideality factor, which describes the deviation of the ideal diode from the Shockley diffusion theory;
- V_T is the thermal voltage of the diode, which depends on the electron charge q, the Boltzmann constant k and the temperature T.

The thermal voltage is defined as:

$$V_T = \frac{k \cdot T}{q} \tag{3.65}$$

where k_b is the Boltzmann constant, T_{array} is the absolute temperature of the photovoltaic cell, and q is the elementary charge (1.602×10^{-19} C).

The remaining constraints governing the modelling are R_s, R_{sh}, I_{pv}, I_D and a. As previously said, a is the only assumed parameter, whose value varies depending on the analysed cell. To simplify the analysis of multi-junction cells, the single-diode model (SDM) is adopted as an equivalent representation of the overall device behavior, with the ideality factor treated as an effective parameter that accounts for the combined effects of the multiple junctions and associated recombination mechanisms [31]. For devices with a higher number of junctions, such as four-junction architectures, the effective ideality factor is typically larger and is usually determined experimentally through fitting of the measured I-V characteristics [13]. In general, for MJSCs, its value floats around the number of junctions; for example, a 4-junction solar cell has an ideality factor around 4.

This reduces the necessary parameters to be extracted to four; using the values of the short-circuit current I_0, the open-circuit voltage V_{oc}, the current and voltage at the maximum power point, I_m and V_m, available in the cells datasheet, the parameters R_s, R_{sh}, I_{pv} and I_D can be calculated [13]. By applying the four constraints to the equivalent circuit equation (Equation 3.64), the following expressions can be obtained.

- Short circuit equation (V=0):

$$I_{sc} = I_{pv} - I_0 \cdot \left[\exp\left(\frac{I_{sc} \cdot R_s}{aV_T}\right) - 1\right] - \frac{I_{sc} \cdot R_s}{R_{sh}} \tag{3.66}$$

- Open circuit equation (I=0):

$$0 = I_{pv} - I_0 \cdot \left[\exp\left(\frac{V_{oc}}{aV_T}\right) - 1\right] - \frac{V_{oc}}{R_{sh}} \tag{3.67}$$

- Maximum power point circuit equation:

$$I_m = I_{pv} - I_0 \cdot \left[\exp\left(\frac{V_m + I_m \cdot R_s}{aV_T}\right) - 1\right] - \frac{V_m + I_m \cdot R_s}{R_{sh}} \tag{3.68}$$

Starting from the zero-derivative condition of the power at the maximum power point (MPP) calculated in Appendix C, the circuit equations can be derived and simplified [13].

Series resistor R_s:

$$\frac{aV_T V_m (2I_m - I_{sc})}{(V_m I_{sc} + V_{oc}(I_m - I_{sc}))(V_m - I_m R_s) - aV_T(V_m I_{sc} - V_{oc} I_m)} = \exp\left(\frac{V_m + I_m R_s - V_{oc}}{aV_T}\right) \tag{3.69}$$

Shunt resistor R_{sh}:

$$R_{sh} = \frac{(V_m - I_m R_s)\,(V_m - R_s(I_{sc} - I_m) - V_T)}{(V_m - I_m R_s)\,(I_{sc} - I_m) - V_T I_m} \tag{3.70}$$

Reverse saturation current I_0:

$$I_0 = \frac{(R_{sh} + R_s) I_{sc} - V_{oc}}{R_{sh} \cdot \exp\left(\frac{V_{oc}}{a V_T}\right)} \tag{3.71}$$

Photocurrent I_{pv}:

$$I_{pv} = I_{sc} \frac{R_{sh} + R_s}{R_{sh}} \tag{3.72}$$

The resulting expressions provide analytical formulas for R_s, R_{sh}, I_0, and I_{pv} [13]. Although the system is decoupled, the equation for R_s remains implicit; however, it can be solved numerically or rewritten in explicit form using the Lambert W-function [13], to solve the exponential structure of the I-V characteristic, as shown in Appendix C.

In order to determine the values to be used in the model, a comparison is carried out among the best space-grade solar cells currently available on the market. The resulting reference parameters are obtained by averaging their main parameters in Tables 3.9 and 3.10, leading to the values in Tables 3.11 and 3.12.

Table 3.9: Main electrical and geometrical parameters of the analysed cells.

Name	$\mathbf{V_m}$ [V]	$\mathbf{I_m}$ [mA/cm^2]	$\boldsymbol{\eta}$	$\mathbf{e_t}$ [1/°C]	$\mathbf{W_{cell}}$ [kg]	$\mathbf{t_{cell}}$ [μm]
4G32HP	2.97	14.17	0.31	-0.0085	0.0104	245
4G328x8	3.001	14.35	0.314	-0.0085	0.0065	190
3G308x8	2.4	16.7	0.296	-0.0064	0.0052	150
3G304x8	2.411	16.7	0.298	-0.0067	0.0026	150
XTJprime	2.406	17.5	0.307	-0.0063	0.0029	182.5
XTElilt	2.459	17.4	0.318	-0.0064	0.0023	154
XTEhf	2.49	17.4	0.321	-0.0063	0.0023	154
XTEsf	2.435	17.9	0.322	-0.0062	0.0029	182.5
Z4J+	3.31	12.8	0.313	-0.0098	0.0044	176.0
Z4J	3.54	11.5	0.3	-0.0103	0.0044	167.4

Table 3.10: Thermal coefficients of the analysed cells.

Name	$\mathbf{V_0}$ [V]	$\mathbf{I_{sc}}$ [mA/cm^2]	$\frac{dV_0}{dT}$ [V/°C]	$\frac{dI_{sc}}{dT}$ [mA/°C]	$\frac{dV_m}{dT}$ [V/°C]	$\frac{dI_m}{dT}$ [mA/°C]
4G32HP	3.405	14.9	-0.0084	0.00231	-0.0086	0.0010072
4G328x8	3.415	14.9	-0.0084	0.00232	-0.0086	0.001027
3G308x8	2.7	17.2	-0.0062	0.01193	-0.0067	0.00795
3G304x8	2.7	17.23	-0.0062	0.01193	-0.0067	0.00795
XTJprime	2.72	18	-0.0056	0.01	-0.0063	0.005
XTElilt	2.755	18.1	-0.0058	0.009	-0.0066	0.006
XTEhf	2.782	18	-0.0057	0.01	-0.0063	0.008
XTEsf	2.75	18.6	-0.0056	0.011	-0.0063	0.006
Z4J+	3.72	13.4	-0.0093	0.0079	-0.0098	0.0047
Z4J	3.95	12	-0.0096	0.0066	-0.0103	0.0048

Table 3.11: Electrical parameters of the average solar cell.

Parameter	**Value**	**Unit**
V_0	3.09	V
V_m	2.74	V
I_{sc}	16.24	A/m^2
I_m	15.64	A/m^2
η_{cell}	31	%
W_{cell}	4.37	g
t_{cell}	1.75×10^{-4}	m

Table 3.12: Thermal coefficients of the average solar cell.

Parameter	Value	Unit
e_t	-2.50×10^{-3}	$°C^{-1}$
$\frac{dV_0}{dT}$	-7.10×10^{-3}	V/°C
$\frac{dV_m}{dT}$	-7.60×10^{-3}	V/°C
$\frac{dI_{sc}}{dT}$	8.30×10^{-3}	$A/m^2/°C$
$\frac{dI_m}{dT}$	5.24×10^{-3}	$A/m^2/°C$

Since the values of I_m and I_{sc} depend on the cell active area, a reference solar cell area is considered; $A_{cell} = 30\ cm^2$.

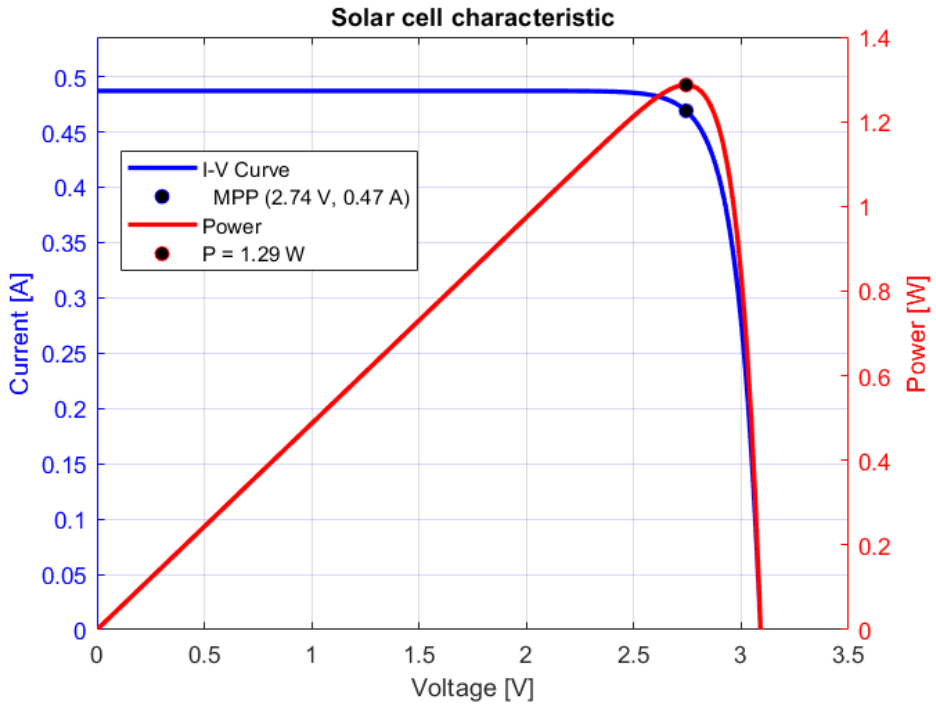

Figure 3.41: Average cell I-V and Power curve.

Solar array systems typically employ an algorithm known as Maximum Power Point Tracking (MPPT), whose role is to continuously monitor the operating point of the electrical loads in order to extract the maximum available power from the arrays. It can also be used as a moderator in power output, shifting the operating point along the I-V curve (reducing the efficiency of the solar array) to provide the necessary power and eliminating the excess, preventing further dissipation.

3.2.1 Solar cell degradating factors

The specific output power determines the efficiency and effectiveness of the solar cells in converting sunlight into electrical energy to supply the various subsystems. In order to calculate the accurate output power, several factors must be taken into account, such as incident solar radiation, eclipse periods, orientation angles, and solar cell characteristics, including active area, conversion efficiency, and temperature coefficient. These variables are then combined within mathematical formulations to determine the specific output power of each individual solar cell. The intensity of solar radiation incident perpendicularly on a surface is equal to 1361 W/m^2 identified as $AM0$. Therefore, the specific power output of the solar cell without losses can be calculated as

$$P_0 = \text{AM0} \cdot \eta_{\text{cell}} \tag{3.73}$$

where η_{cell} is the conversion efficiency of the solar cell.

Lifetime degradation factor

Degradation effects are taken into account in order to predict the overall decline in solar cell efficiency over time. The average degradation coefficient K_d is defined as the factor by which the solar cell efficiency decreases as a consequence of space radiation and other environmental effects. It is calculated using the following equation

$$K_d = [1 - degr/100]^y \tag{3.74}$$

where $degr$ is the cell degradation coefficient per year and y is the actual rover lifetime in years.

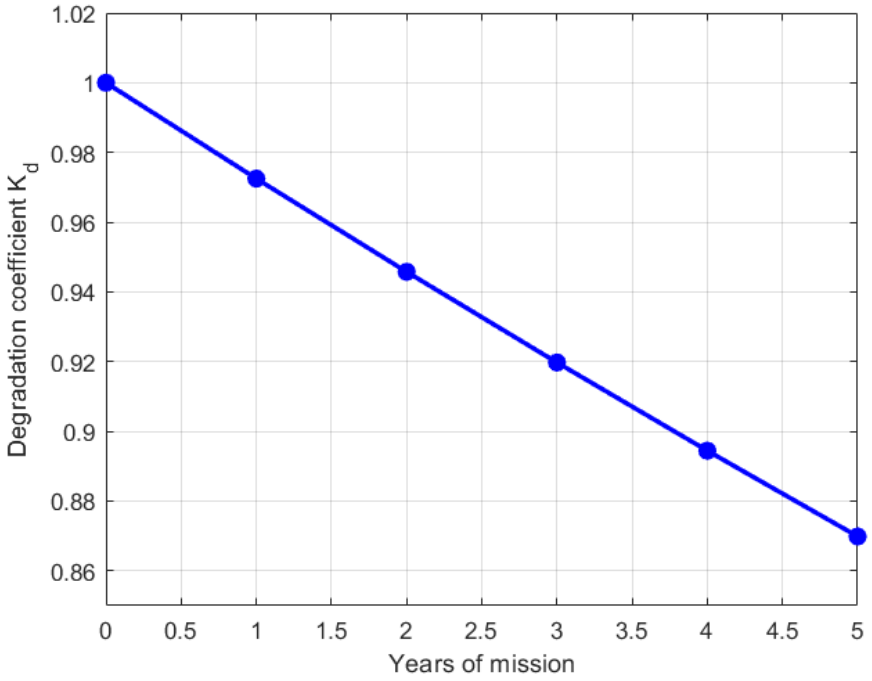

Figure 3.42: Lifetime degradation coefficient.

Illumination coefficient

The angle at which solar rays strike the array plays a key role in ensuring sufficient power generation to supply the spacecraft subsystems. The maximum power is obtained when the incidence is perpendicular to the surface, while deviations from this condition result in losses proportional to the cosine of the angle formed between the incident ray and the array surface:

$$K_{ill} = cos(\alpha) \tag{3.75}$$

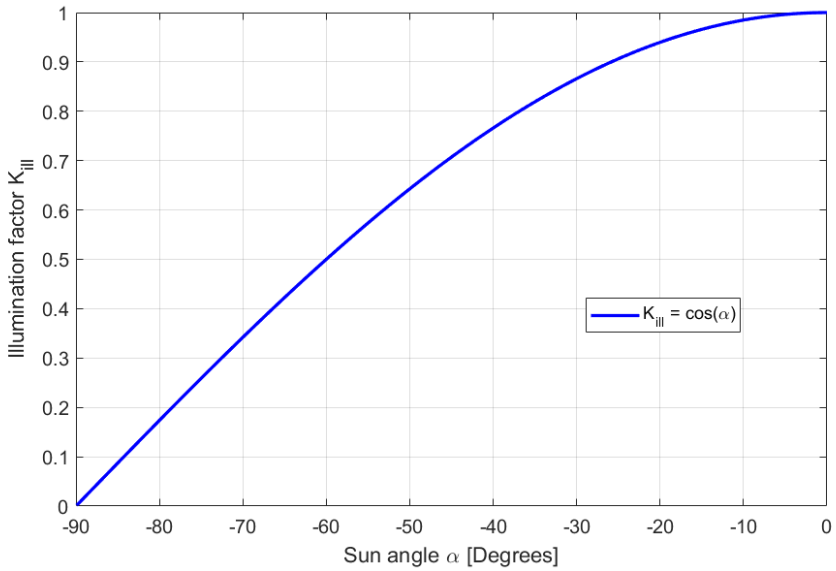

Figure 3.43: Illumination coefficient.

Temperature coefficient

The solar radiation that is absorbed but not converted into electrical power contributes to heat generation; that is, after subtracting the reflected portion and the part converted by the cell, it results in an increase in the operating temperature. This contribution is included in the equation for T_{op}, where the term $\text{AM0} \cdot (a_t - \eta_{\text{cell}})$ appears. To minimize losses due to the thermal degradation coefficient, the operating temperature must be maintained as close as possible to the reference temperature.

To analyse this effect, it is necessary to determine which surfaces of the array radiate the accumulated heat. For a fixed array configuration, two radiative cases can be distinguished: a single-sided radiative configuration, in which only one face radiates toward deep space at 0 K, and a double-sided radiative configuration, in which one face radiates toward deep space at 0 K and the other exchanges radiation with the rover structure, assumed to be in radiative thermal equilibrium at a temperature T_r ranging between 40 and 400 K.

This results in a general equation 3.76 for both cases where only ϵ and T_r differ.

$$T_{\text{op}} = \left[\left(\frac{a_t - \eta_{cell}}{\epsilon \cdot \sigma_{SB}} \right) \cdot AM0 \cdot K_{ill} + \frac{T_r^4}{2} \right]^{1/4} \tag{3.76}$$

where a_t is the absorbptance coefficient, ϵ is the array emissivity and σ_{SB} is the Stefan-Boltzmann constant.

- **Front dissipation:** $\epsilon = \epsilon_f$ and $T_r = 0$;
- **Front/back Dissipation:** $\epsilon = \epsilon_f + \epsilon_b$ and $T_r \in [40\,K, 400\,K]$

Solar cells are highly sensitive to temperature variations, which can significantly affect their power output. Accurate estimation of the temperature coefficient ensures that the cells can deliver optimal performance regardless of the harsh space environment. These temperature variations directly affect the $I-V$ characteristics of the solar array. Consequently, a temperature coefficient K_t must be considered and can be estimated as in equation 3.77.

$$K_t = (1 + e_t \cdot \Delta T) \tag{3.77}$$

where

$$\Delta T = T_{op} - T_{ref,c} \tag{3.78}$$

and $T_{ref,c}$ is the optimal temperature of the solar cell at which the electrical parameters are evaluated.

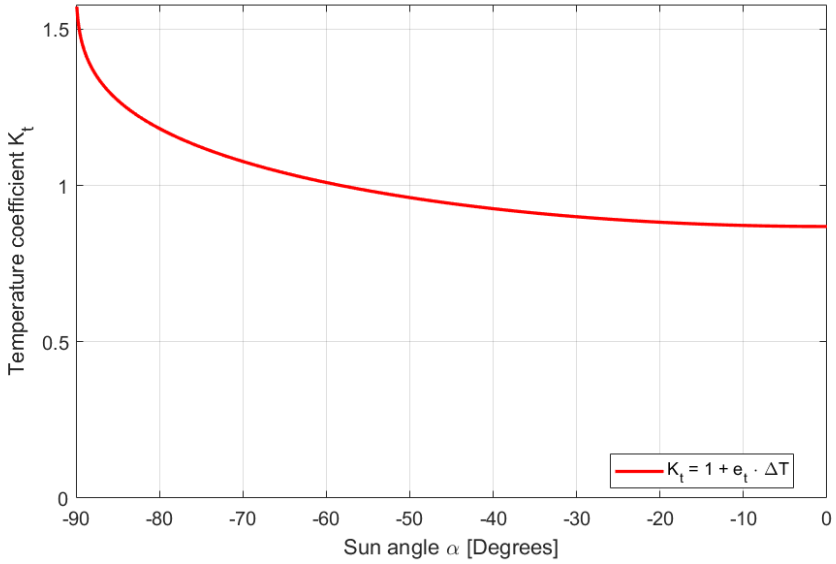

Figure 3.44: Temperature coefficient for front only radiative surface.

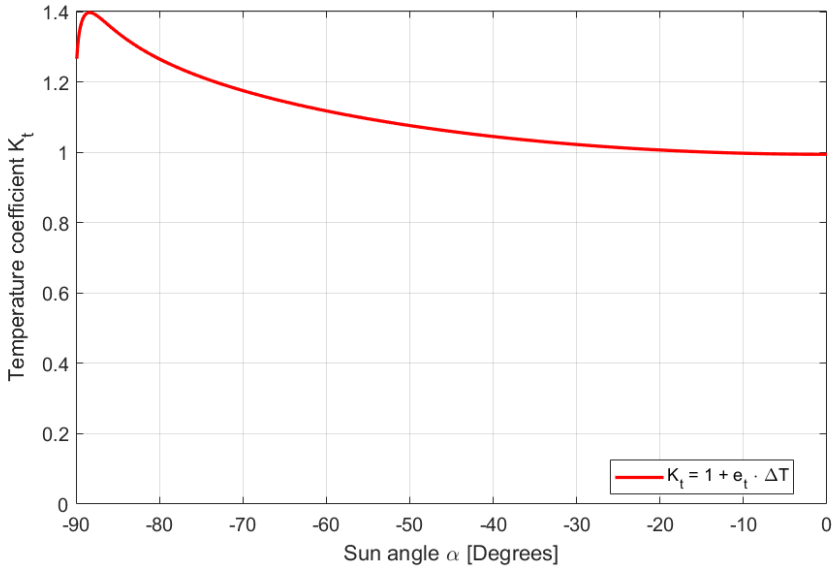

Figure 3.45: Temperature coefficient for front and back radiative surface.

Front only dissipation allows for enhanced performance at lower angles, but falls below 1 for sun angles between $-50°$ and $0\,°$; front and back dissipation has only positive consequences having $K_t \geq 1$.

System efficiency

For the calculation of the specific actual power is necessary to consider the overall system efficiency with a value assumed of $\eta_g = 0.9$ as seen previously, which includes losses due to wiring, blocking diodes, and other components.

3.2.2 Specific output power

To correctly evaluate the design point, it is necessary to define the concept of *begin of life* (BOL) and *end of life* (EOL) performance. The solar array will exhibit different output levels over its lifetime; in particular, at EOL the degradation coefficient reaches its maximum value, reducing the effective power output of the array.

The parameters governing the degrading coefficients are listed in table 3.13.

Table 3.13: Parameters governing solar cell degrading factors.

Parameter	Description	Value / Unit
$degr$	Degradation coefficient per year	2.75 %/year
y	Rover lifetime	5 years
e_t	Temperature coefficient	$-0.0025\ ^{\circ}\mathrm{C}^{-1}$
$T_{\mathrm{ref,c}}$	Reference temperature	301 [K]
σ_{SB}	Stefan-Boltzmann constant	$5.670 \times 10^{-8}\ \mathrm{W/m^2K^4}$
T_r	Temperature of radiating environment	0 K (front) / 40-400 K (back)
a_t	Absorptance of the solar cell	0.90 [-]
a_r	Absorptance of the rover external layer	0.80 [-]
ϵ_f	Front surface emissivity	0.90 [-]
ϵ_b	Back surface emissivity	0.80 [-]
ϵ_r	Rover surface emissivity	0.85 [-]
η_{g}	Overall system efficiency	0.90 [-]

The performance of a solar cell varies along its *I-V* characteristics. To maximize the output, the cell is assumed to operate at its maximum power point (MPP). This is achieved by implementing a Maximum Power Point Tracker (MPPT), which ensures that the cell always operates under optimal conditions and to deliver the maximum power output. If the power required is lower, the MPPT can shift the operating point from the MPP to a suitable combination of voltage and current along the I-V curve of Figure 3.41.

The maximum voltage V_m and current I_m depend linearly on temperature, as a first-order approximation, according to the parameters reported in Table 3.12, leading to the relationships in Equation 3.79 and 3.80.

$$V_{m_T} = V_m + \frac{dV_m}{dT} \cdot \Delta T \tag{3.79}$$

and

$$I_{m_T} = I_m + \frac{dI_m}{dT} \cdot \Delta T \tag{3.80}$$

Having defined the operating point and all the degrading coefficients, the total specific power output of the cell is defined in Equation 3.81 using the cell area A_{cell} in m^2.

$$P_{act} = \frac{V_{m_T} \cdot I_{m_T} \cdot K_{ill} \cdot K_d \cdot K_t \cdot \eta_g}{A_{cell}} \tag{3.81}$$

BOL performance

The performance is evaluated with the specific power output for different sun angles from $-90°$ to $0°$ and as stated previously, in this condition $K_d = 1$.

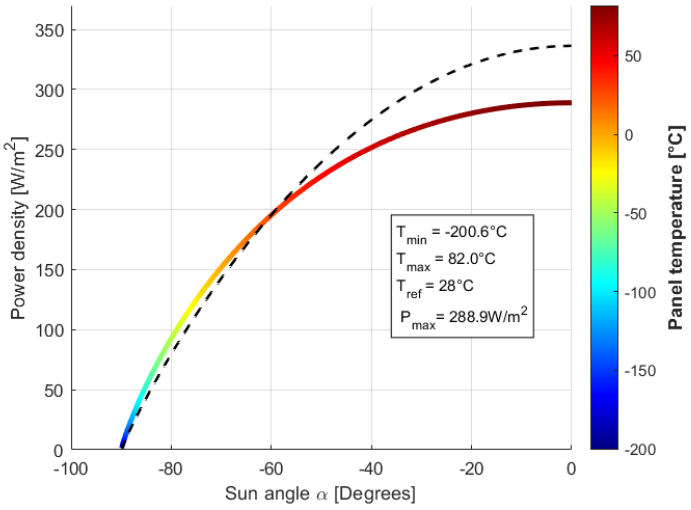

(a) Front only radiation

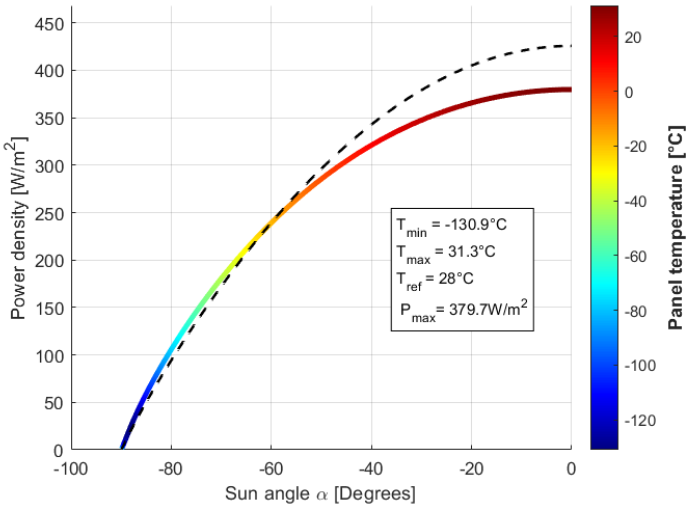

(b) Back + Front radiation

Figure 3.46: Solar power performance under different *begin of life* (BOL) operating conditions: (a) exclusive front heat dissipation, and (b) front and back radiative heat exchange configuration. In both cases, the dotted line represents the solar power performance evaluated at constant optimal temperature $T_{ref,c}$ during the entire solar exposure, whereas the solid colored line illustrates the power behavior at the operating temperature T_{op}, which varies as a function of the sun angle α.

EOL performance

The performance is evaluated with the specific power output for different sun angles from $-90°\ to\ 0°$ and as stated previously, in this condition K_d follows equation 3.74.

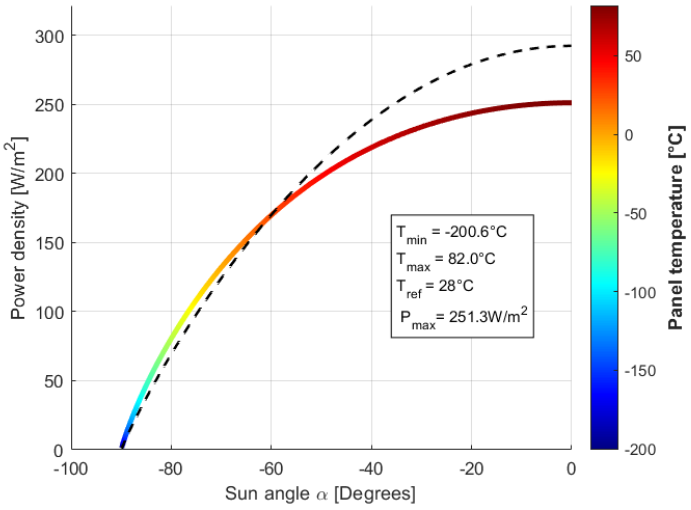

(a) Front only radiation

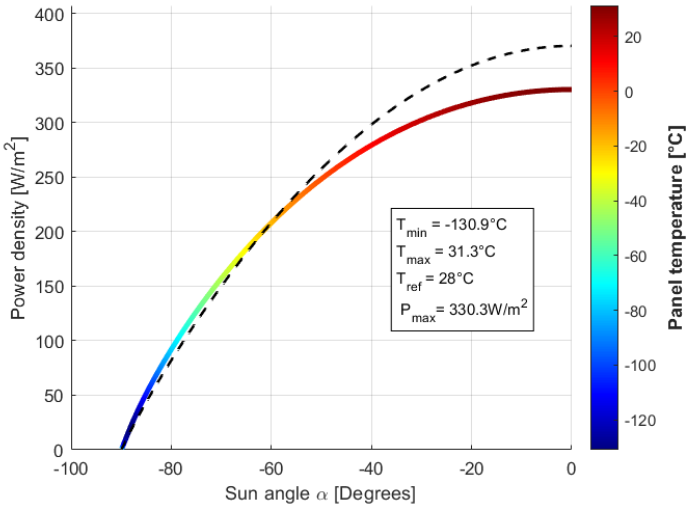

(b) Back + Front radiation

Figure 3.47: Solar power performance under different *end of life* (EOL) operating conditions: (a) exclusive front heat dissipation, and (b) front and back radiative heat exchange configuration. In both cases, the dotted line represents the solar power performance evaluated at constant optimal temperature $T_{ref,c}$ during the entire solar exposure, whereas the solid colored line illustrates the power behavior at the operating temperature T_{op}, which varies as a function of the sun angle α.

3.2.3 Solar array area

Having determined the power density for the different configurations, it is now possible to evaluate the total required area to achieve the specified power output. From this point, the sizing process will be based on the *end of life* (EOL) condition, while the two proposed radiative configurations will be systematically compared. In the array sizing procedure, a Packing Factor (PF) of 0.7 is introduced to account for inactive areas due to inter-cell spacing, structural supports, wiring, and integration constraints. The effective array area is therefore defined in Equation 3.82.

$$A_{\text{array}} = PF \cdot A_{\text{active}} \tag{3.82}$$

where A_{active} is the total active solar cell area required to meet the power demand.

Since the power output depends on the sun angle, the required array area also varies accordingly.

Front dissipation

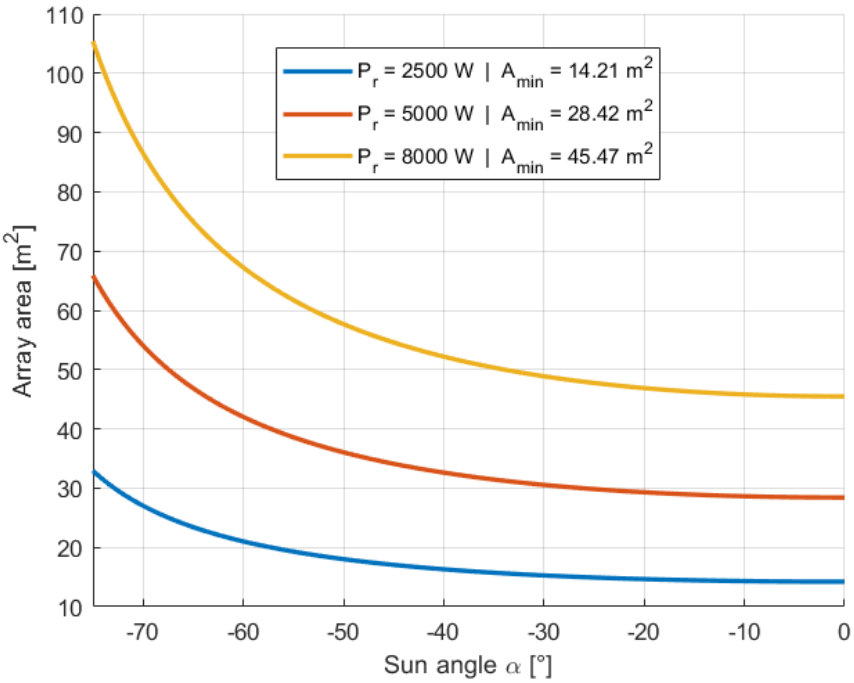

Figure 3.48: Necessary A_{array} for different power output for exclusive front radiative surface.

Front and back dissipation

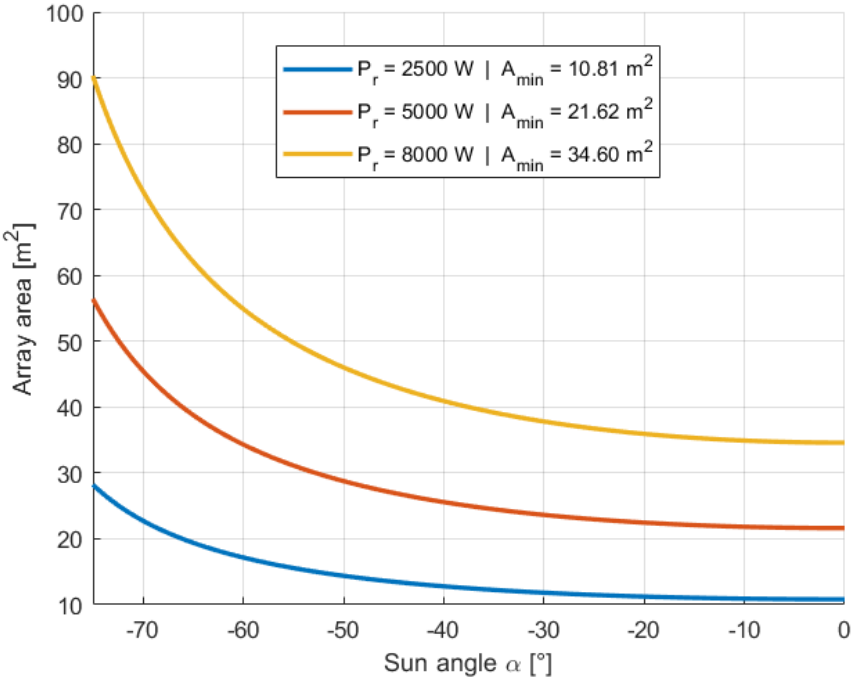

Figure 3.49: Necessary A_{array} for different power output for front and back radiative surfaces.

From Figure 3.48 and 3.49 it is possible to notice a reduction of the required area A_{array} around 24% for every power level. This reduction implies that the most convenient choice lies in the dual radiating surface configuration. Moreover, the required area remains only slightly variable over the illumination angle range α between $-40°$ and $0°$.

3.2.4 Mass estimation

As the solar array exhibits a significant necessary area, the choice must necessarily fall on a deployable solution. The parameter that defines the mass of the solar array system is expressed in kg/m^2, in order to obtain a direct mass estimate once the area is determined. To identify a realistic value and assess its impact on the rover's total mass, it is necessary to analyse the currently available options on the market and extract a representative indicative value; to do so a realistic reference, high-power applications are considered, such as those on the ISS, which feature large array areas and good structural rigidity with roll-out solar array technology (ROSA), or circular configurations, such as those provided by UltraFlex technology and used in many extraterrestrial missions.

Table 3.14: Deployable solar array technologies mass, area and density.

Technology / Mission	**Mass [kg]**	**Area [m^2]**	**Density [kg/m^2]**
DIAMOND (ROSA) [36]	36	19.95	1.81
OPAL (ROSA) [36]	42.7	33.64	1.27
SAPPHIRE (ROSA) [36]	160	71.02	2.25
TANZANITE (ROSA) [36]	180	102.92	1.75
SUNSTONE (ROSA) [36]	331	60.14	5.50
PHENACITE (ROSA) [36]	521	91.39	5.70
Cygnus Spacecraft (UltraFlex)	23.3	10.75	2.17
InSight Lander (UltraFlex) [37]	12.7	7.26	1.7
Lucy Spacecraft (UltraFlex) [12]	176	40	4.4

To account for safety margins and maintain a conservative approach while considering future technologies advancements, a reference value of $3\,\mathrm{kg/m^2}$ is taken.

3.3 Requirements

This section specifies the requirements and constraints that will characterize propulsion choices in accordance with the current standard ”ECSS-E-ST-10-06C”.

Requirements Identification

Requirement identifiers, preceded by **R-**, belong to the following categories:

- **FUN:** Functional;
- **MIS:** Mission;
- **ENV:** Environmental;
- **OPS:** Operational;
- **HMA:** Human factor;
- **DES:** Design.

Requirements will be written in the format **R-YYY-XX**, e.g., **R-MIS-01**.

Functional requirements

R-FUN-01 The propulsion subsystem shall provide mobility capability that supports 14 consecutive days of surface operations outside the lunar base under nominal power conditions.

R-FUN-02 The propulsion subsystem shall allow emergency return to the base from the farthest nominal operating point, preserving life-support integrity for the crew members.

R-FUN-03 The propulsion subsystem shall provide torque and traction performance to support rover mobility.

R-FUN-04 The propulsion subsystem shall power scientific payload operation, including sample collection, in-situ analysis, and data transmission to the lunar base.

R-FUN-05 The propulsion subsystem shall maintain operational performance within its design temperature limits when the rover internal temperature is between 18 °C and 24 °C.

R-FUN-06 The propulsion subsystem shall provide communication capability with the lunar base and/or orbital relay with continuous coverage during nominal operations.

Mission requirements

R-MIS-01 The power system shall be capable of delivering at least 5 kW during nominal operating conditions.

R-MIS-02 The power system shall be capable of delivering at least 2 kW during reduced-power operation.

R-MIS-03 The power system shall be capable of supplying at least 1 kW to maintain essential subsystems during emergency operation.

R-MIS-04 The rover shall enable acquisition, storage, and transmission of all scientific data collected during the mission.

R-MIS-05 The rover shall have a design life of 5 years under nominal operational profile.

R-MIS-06 The regenerative power sources shall sustain more than 1000 charge/discharge cycles.

Environmental requirements

R-ENV-01 The rover shall withstand lunar temperature variations between $-233\,^{\circ}C$ and $+123\,^{\circ}C$.

R-ENV-02 The rover shall protect the crew and all of the subsystem from radiation.

R-ENV-03 The rover shall prevent lunar dust intrusion into critical subsystems, including joints and seals, ensuring full functionality during and after surface operations.

R-ENV-04 The rover shall be able to climb on slope up to 30°.

Operational requirements

R-OPS-01 The rover shall have a body mounted solar array capable of area extension, while the rover is not moving, to maximize the power available and support the crew in scientific operations.

Human factor requirements

R-HFA-01 The rover shall allow intra-vehicular activity (IVA) for crew operations, including rest, food consumption, and basic hygiene.

R-HFA-02 The rover shall be equipped with at least two EVA suits.

R-HFA-03 The rover shall allow extra-vehicular activity (EVA) for crew operations outside the rover.

R-HFA-04 The rover shall store and manage consumables (oxygen, water, food) adequate for the nominal mission duration, plus 2 days for contingency operation.

Design requirements

R-DES-01 The vehicle subsystems shall be designed for modularity and ease of maintenance, allowing replacement of major components (e.g., wheel modules, power units) with standard interfaces.

R-DES-02 The electrical harness shall be designed to ensure redundancy and fault isolation, in compliance with ECSS-E-ST-50.

R-DES-04 The rover, in its entirety, shall bear the launch loads without permanent deformation and damage.

4 Results

In this section, the performance of the battery pack and the solar array will be analysed. Each subsystem will be first evaluated independently in order to clearly identify its operational limits. Subsequently, they will be coupled and simulated under different power demand scenarios.

4.1 Limitations on single system propulsion

A brief analysis of single-system propulsion, highlights the inherent limitations of relying on a single power source. Such limitations include restricted operational range and reduced flexibility under varying environmental conditions. Understanding these constraints is essential for defining feasible mission profiles and ensuring reliable rover performance throughout lunar operations.

Battery

Relying exclusively on a battery pack to power the rover during operations is primarily limited by the inability to recharge, once the stored energy is depleted, which leads to a linear increase in pack mass (Figure 4.1) with the planned mission duration. For this type of usage, primary batteries would be required, offering higher performance than secondary, but remaining highly constrained for long-duration operations.

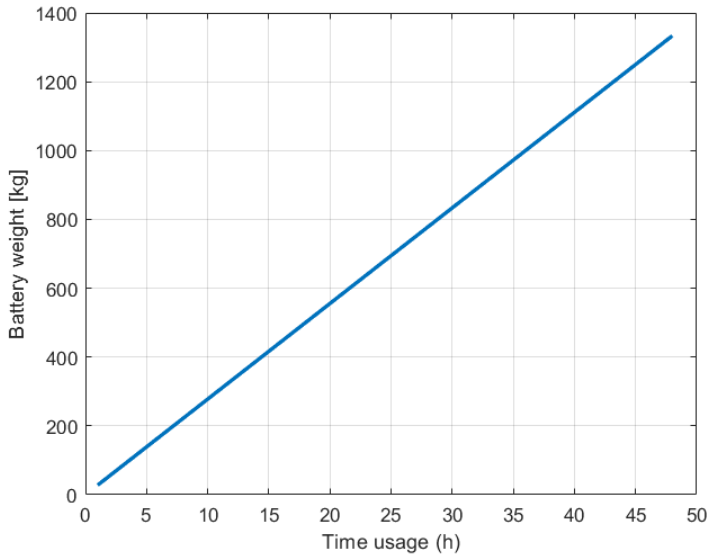

Figure 4.1: Increase in battery pack weigth due to increasing operational time t_r for $P_r = 5000\,W$.

From Figure 4.1 it is clear that for operations requiring more than 15 hours, the subsystem weight can be significantly affected.

Solar array

For this type of power source, the main limitation is its dependence on solar radiation. Without sunlight, the system can't generate power, imposing mission planning and activity scheduling

exclusively during sunlight periods. Moreover, being in direct contact with the external lunar environment, the operational flexibility and range of the rover are strongly constrained not only by the availability of solar energy but also by harsh environment conditions. For long-duration missions, the lack of a secondary power source can pose serious risks to both mission success and, more importantly, the safety of the occupants.

4.2 Mission Profile

The mission profile is a sequence of phases, which involve lunar exploration (covering long distances outside the base), extravehicular operations, scientific activities and the return to base. Intermediate mission phases can be split to allow in-situ operations at multiple locations on the lunar surface. This implies that, once a target is reached, the mission may involve multiple trips to other locations before returning to the base. The rover is assumed to operate close to the lunar equator in order to evaluate highly variable environmental conditions in terms of solar illumination and thermal environment. In this region, the large variation between daytime and nighttime conditions provides a representative case for assessing the performance of the solar array. To accomplish the mission objectives, a duration corresponding to a full lunar day-night cycle (approximately 29 Earth days) is considered. Since at the equator roughly half of this period corresponds to daylight and the other half to night, operations are preferably conducted during at least partial sunlight to ensure sufficient solar energy availability.

The battery is primarily used to supply electrical power during rover mobility operations. The solar array is assumed to remain retracted during travel phases in order to prevent potential damage caused by vibrations or sudden mechanical loads resulting from moving on an uneven terrain; therefore, it is assumed to be unable to generate power during these operations. In addition, the battery serves to absorb power peaks that exceed the output capability of the solar array. The rover will operate on a non-homogeneous surface, therefore, it will face obstacles and slopes that will increase the required power.

Two main operational modes have been identified and are summarized in Table 4.1.

Table 4.1: Operational types and modes for mission profile.

Type	Mode	Description
1	Battery-only operations	The rover operates relying solely on stored battery energy. This includes phases such as transfers and returns, where solar arrays are retracted and not available.
2	Battery operations with solar support	The rover is assisted by solar arrays during operation. This includes scientific, overpower and standby phases, where solar energy is used to recharge batteries or sustain payloads.

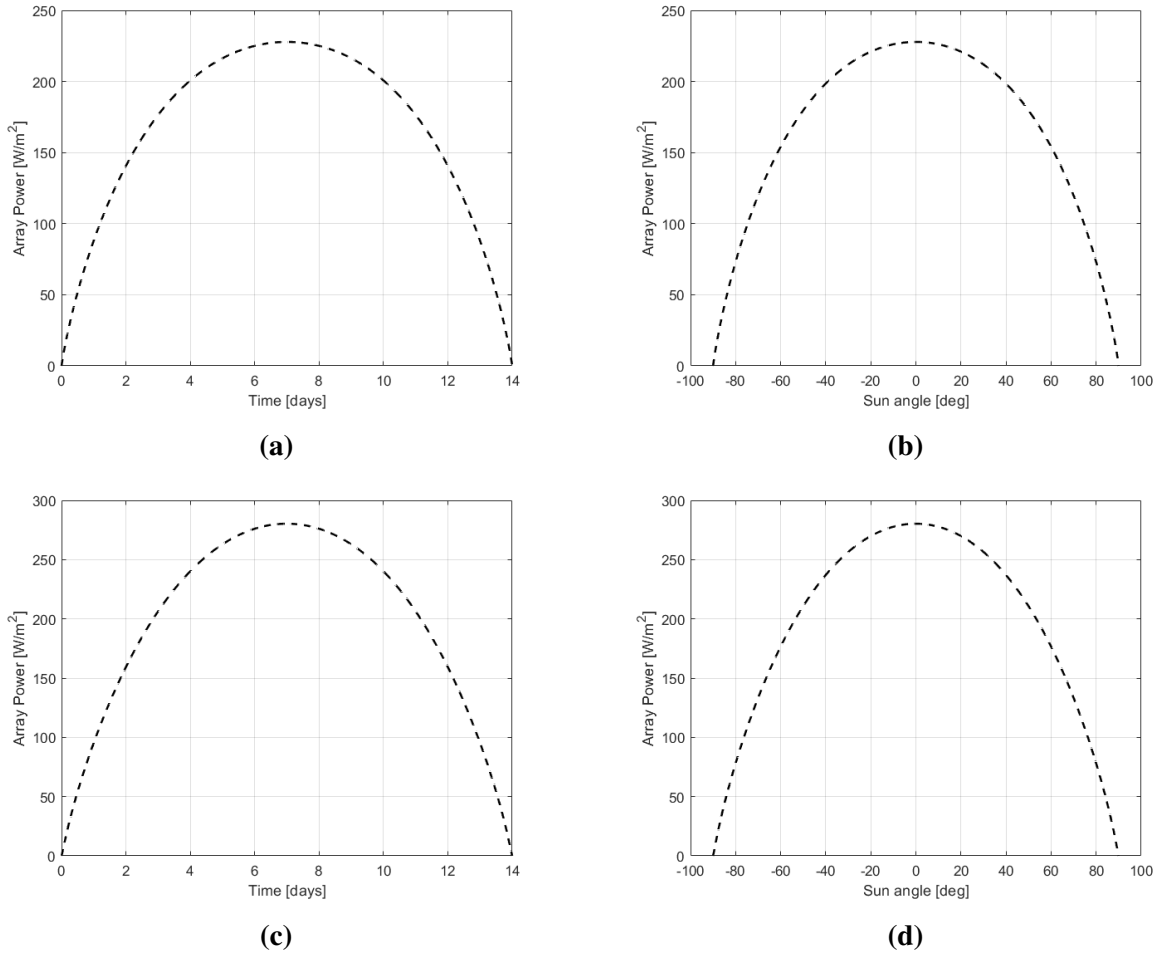

Figure 4.2: Specific power generation of the solar array under different thermal dissipation regimes: *Front-surface only dissipation* showing (a) temporal evolution during the lunar day and (b) sensitivity to the solar incidence angle; *Double-sided (front and back) dissipation* showing (c) temporal evolution during the lunar day and (d) sensitivity to the solar incidence angle.

In Figure 4.2, the specific power generation of the solar array under different thermal dissipation regimes during the equatorial lunar day is represented. The most performant configuration is the double-sided dissipation, which allow a lower maximum operating temperature and a higher power density, as discussed in Section 3.2.3, reaching a temperature of about 31° C when the sun angle α is 0° (Figure 3.47b).

Once operational modes are defined and the solar array operating condition is established, the single phases can be discussed individually.

4.2.1 Phases definition

In this section, the phases composing the sizing mission scenarios are described, with a constant power demand assigned to each phase for a predefined duration. The sequence of phases defines the operational timeline of the mission and allows for a system performance evaluation for every phase. Phases are reported in Table 4.2.

Table 4.2: Mission scenarios phases description.

Phase	Type	Description
Transfer	1	Propulsive maneuvering phase characterized by sustained high power demand. The required power may increase in the presence of a positive slope; in such cases, this phase is referred to as *Transfer +*.
Science	2	Nominal operational phase dedicated to scientific activities and onboard payload operations with moderate power consumption. The rover is not moving and the solar array is fully deployed. It can also be indicated as *S*.
Overpower	2	High power operational phase during sunlight period, equivalent to Science, but the power demand exceed the solar array power and the battery pack has to compensate absorbing the power peak. It can also be indicated as *P+*.
Standby	2	Low power operational state intended for battery recharge via solar array, and crew rest or minimal operation. The duration of this phase depends on the time to recharge the battery pack to the SOC target value SOC_t while the rover is not moving. It can also be indicated as *SBY*.
Return	1	Propulsive maneuvering phase characterized by sustained high power demand. Equal to the Transfer phase , but for base returning operations.

While discussing the individual phases, indicative values of $P_r = 5000\,\text{W}$ and $t_r = 6$ hours are adopted to size the battery at $T_{amb} = 20\,^{\circ}C$, since the goal is not the subsystem dimensioning itself, but rather to evaluate how each individual phase affects the system performance. With this premise the maximum charging current considered is equal to $-14.32\,A$, corresponding at $0.2\,C$, indicated as negative according to the adopted sign convention. For a preliminary evaluation, the solar array area is fixed at $24\,m^2$, non orientable, at which correspond a delivered power timeline illustrated in Figure 4.3. The temperature reached by the solar array during the lunar equatorial day is also reported in Figure 4.4.

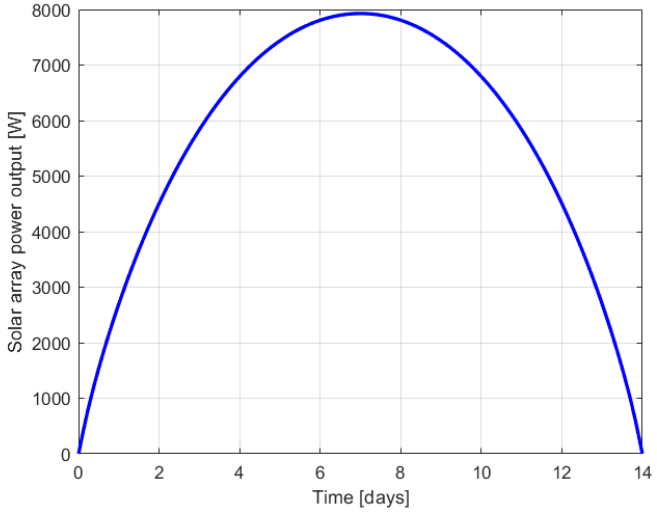

Figure 4.3: Power output of the modeled solar array at $24\,m^2$ during the lunar equatorial day expressed in Earth days.

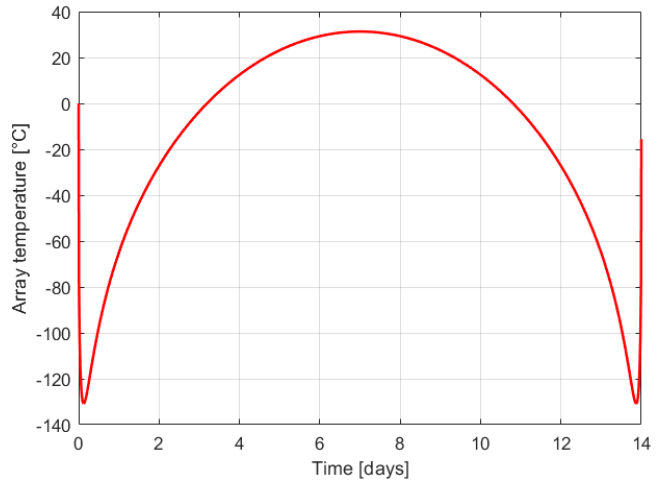

Figure 4.4: Solar array temperature reached during the lunar equatorial day, considering both back and front radiating surfaces.

Transfer and Return

In this phase, the locomotion system is supplied with a constant power of 5000 W for 6 consecutive hours. The electrical parameters and the temperature of the battery pack evolve as shown in Figure 4.5a, while the battery efficiency and the generated and dissipated heat are reported in Figure 4.5b.

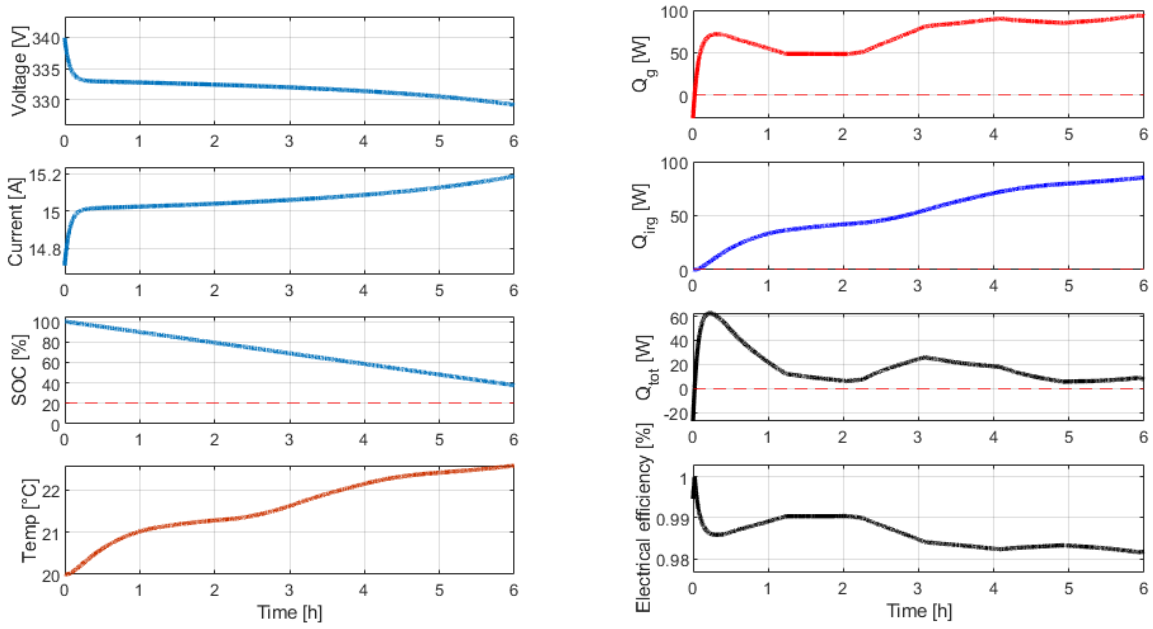

(a) **(b)**

Figure 4.5: Battery pack performance during the Transfer phase; In (a) the evolution of the electrical parameters of the battery pack is shown along with the temperature, while in (b) the generated (Q_g) and dissipated heat (Q_{irg}) contributions are reported as well as the total heat (Q_{tot}) and the battery pack electrical efficiency.

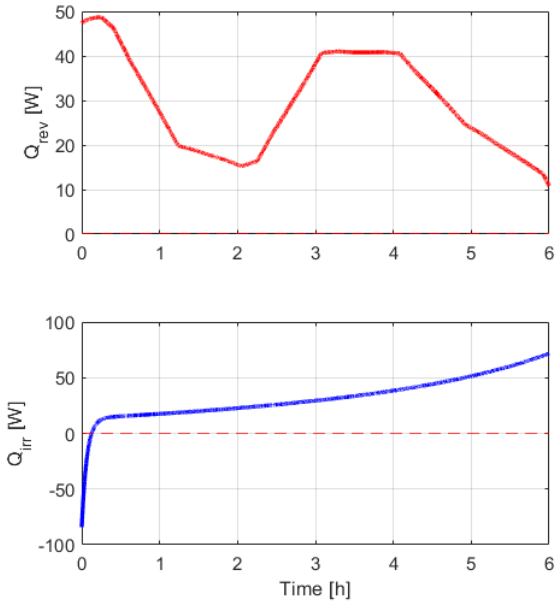

Figure 4.6: Reversible Q_{rev} and irreversible Q_{irr} terms of generated heat Q_g during Transfer phase.

The irreversible heat Q_{irr} (Figure 4.6) rises in response to the voltage, following Equation 3.53, resulting in an increasing generated heat Q_g (Figure 4.5b) and battery pack temperature

(Figure 4.5a). The delivered current adapts to the battery voltage in order to maintain a constant power output. No solar array performance are evaluated in this phase since is considered retracted during Transfer.

Science

This phase is characterized by a relatively low constant power request of 2500 W, to allow the battery to be recharged and the solar arrays alone can provide all the necessary power. This phase is assumed to begin roughly 96 hours after the start of the lunar day (day 4 in Figure 4.3), when the solar arrays are fully deployed and the power required by the subsystems is lower than the power generated by the arrays, thus delivering sufficient power to not require battery support.

The excess power is used to recharge the batteries up to the imposed limit of 0.2 C. If additional excess power is still produced by the solar arrays, they must operate at reduced efficiency (thanks to the MPPT algorithm, which allows the operating point of the solar cell to move along the I-V curve shown in Figure 3.41) in order to provide the appropriate power to the subsystems without producing surplus power that must be dissipated.

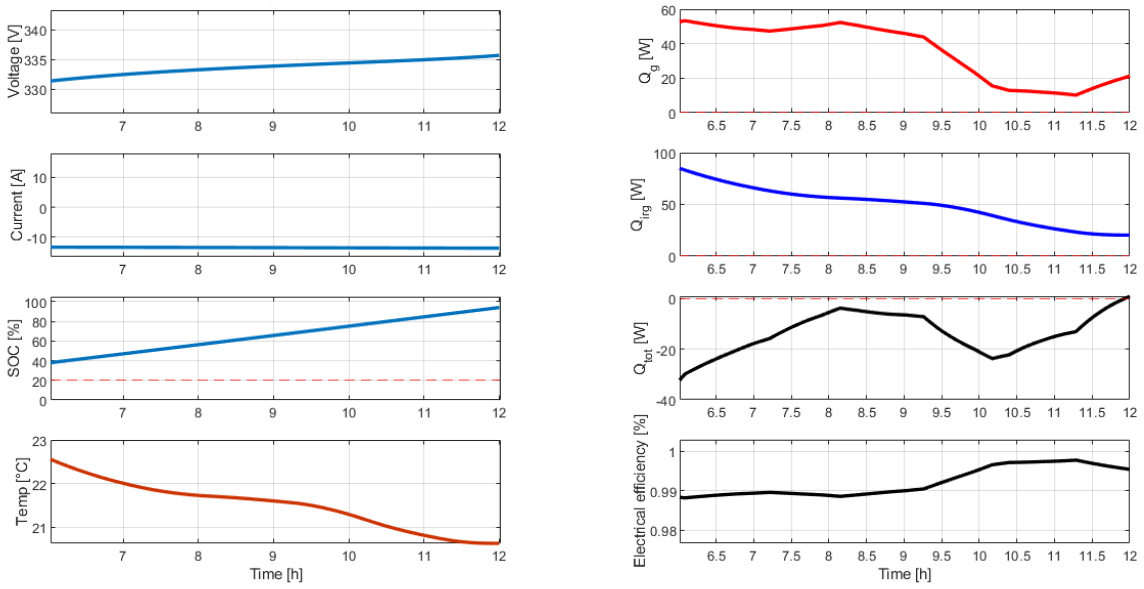

(a) **(b)**

Figure 4.7: Battery pack performance during the Science phase; In (a) the evolution of the electrical parameters of the battery pack is shown along with the temperature, while in (b) the generated (Q_g) and dissipated heat (Q_{irg}) contributions are reported as well as the total heat (Q_{tot}) and the battery pack electrical efficiency.

In Figure 4.7a, the battery is in charging mode; therefore, the voltage increases and the current is negative, while the SOC is obviously increasing, indicating that the charging process is taking place. The temperature in Figure 4.7a decreases since the generated heat Q_g in Figure 4.7b tends to decrease and the heat dissipated through radiation Q_{irg} is greater than the generated heat, resulting in a total heat Q_{tot} that is negative and tends to zero as the battery pack temperature approaches the ambient temperature T_{amb}. The decreasing heat generated is due to the irreversible term in Figure 4.8, which changes sign once the battery pack voltage is

greater than the open circuit voltage $E_{0_{pack}}$ (defined in Appendix A). This effect is observable only during the charging phase, where the applied voltage must overcome the internal resistance and exceed the battery pack open-circuit voltage $E_{0_{pack}}$. Otherwise, the current would not flow in the reverse direction and the battery could not be charged.

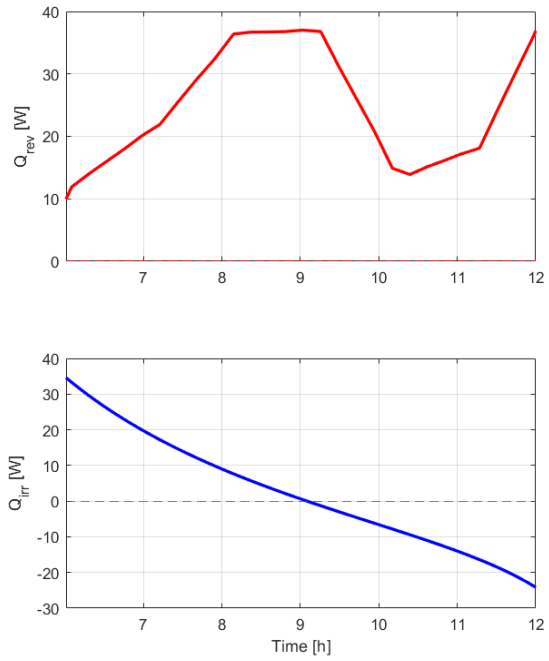

Figure 4.8: Reversible Q_{rev} and irreversible Q_{irr} terms of generated heat Q_g during Science phase.

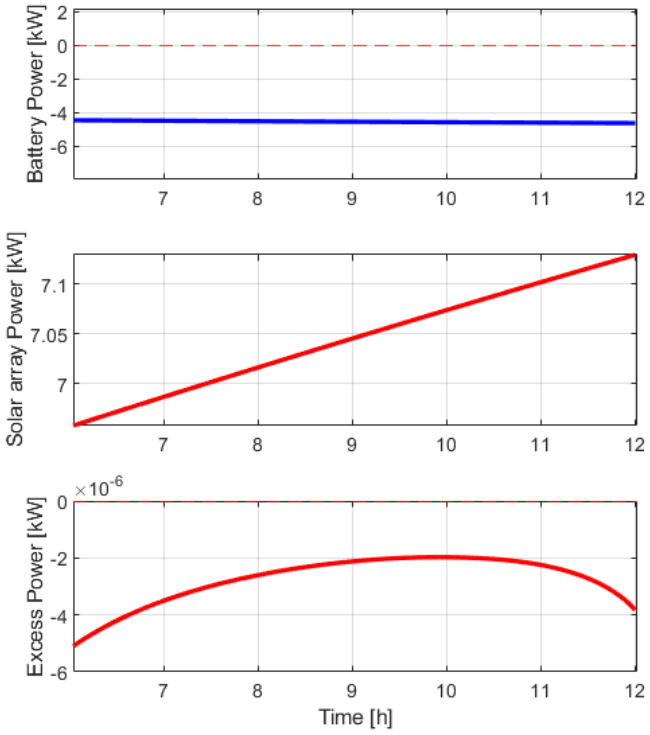

Figure 4.9: From top to bottom: power absorbed by the battery, power delivered by the array and the resulting power excess during Science phases.

In Figure 4.9 , the power absorbed by the battery (the negative sign is due to the negative current) and the power available from the solar array are represented. The solar array power output is increasing because the angle between the panel normal and the incoming solar rays is decreasing; consequently, the charging current slowly increases until it eventually reaches the imposed limit of $0.2\,C$. The excess power is essentially zero, indicating that all the array power not delivered to the load is charging the battery and the array is operating at its full efficiency.

Overpower

The Overpower phase can be seen as a Science phase where the requested power can't be delivered by the solar array alone, therefore the battery must compensate delivering a small amount of power to cover the needs. The illumination condition is considered the same as the Science phase, with solar array initial power corresponding to day 4 of Figure 4.3. In this case, the constant power request is $12000\,W$, greater than the power delivered by solar arrays in Figure 4.3.

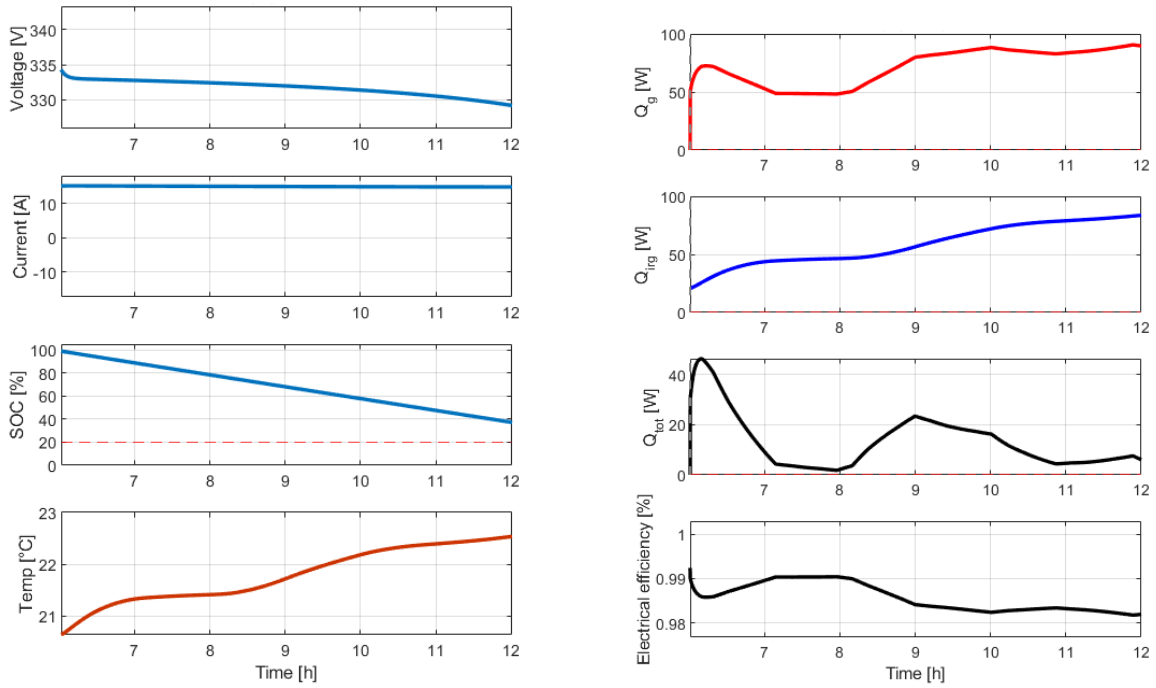

(a) **(b)**

Figure 4.10: Battery pack performance during the Overpower phase; In (a) the evolution of the electrical parameters of the battery pack is shown along with the temperature, while in (b) the generated (Q_g) and dissipated heat (Q_{irg}) contributions are reported as well as the total heat (Q_{tot}) and the battery pack electrical efficiency.

Figure 4.10 represent the same performance of Figure 4.5, indicating that the battery is delivering power and increasing its temperature. Therefore the same consideration of Transfer phase applies.

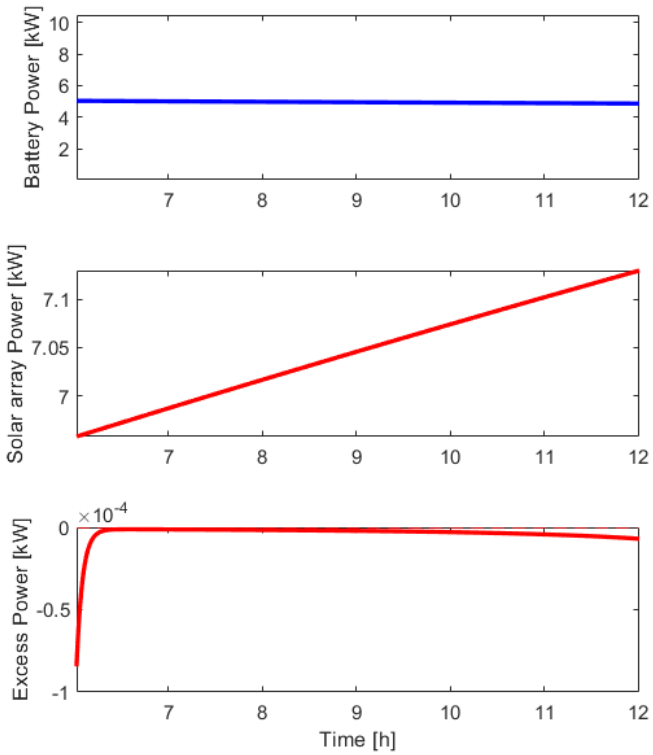

Figure 4.11: From top to bottom: power absorbed by the battery, power delivered by the array and the resulting power excess during Overpower phases.

Figure 4.11 clearly illustrates what is happening: the battery delivers around 5 kW, supporting the power supplied by the solar array to meet the requested power. The battery output power slowly decreases, in response to the increasing power output from the solar array to provide the constant power output requested. Since the battery provides the power needed to compensate for the panel deficits, no excess power is present, as can be seen in the bottom graph of Figure 4.11, which shows negligible power surplus. The solar array is working at its full efficiency.

Standby

The Standby phase is designed to prioritize battery recharging, with a limited power demand assumed of 500 W to support essential subsystems for an undefined duration. This phase remains active until $SOC = SOC_t$, as defined in Table 4.3. The Standby phase is usually performed before the Transfer phase to ensure full battery capability.

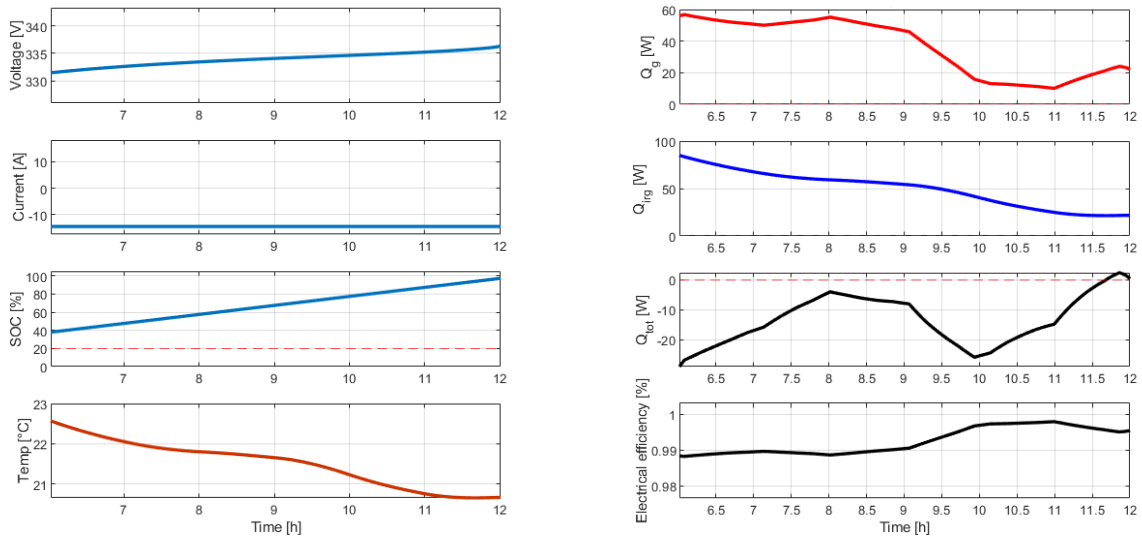

(a) **(b)**

Figure 4.12: Battery pack performance during the Standby phase; In (a) the evolution of the electrical parameters of the battery pack is shown along with the temperature, while in (b) the generated (Q_g) and dissipated heat (Q_{irg}) contributions are reported as well as the total heat (Q_{tot}) and the battery pack electrical efficiency.

The charging current in Figure 4.12a reaches the limit value of $0.2\,C$, allowing the battery to be charged in the shortest possible time. In this case, the battery is charged from an initial SOC of 40%, reaching $SOC_t = 99\,\%$ in approximately 6 hours. The battery charge is characterized by a cooling effect as discussed in the Science phase.

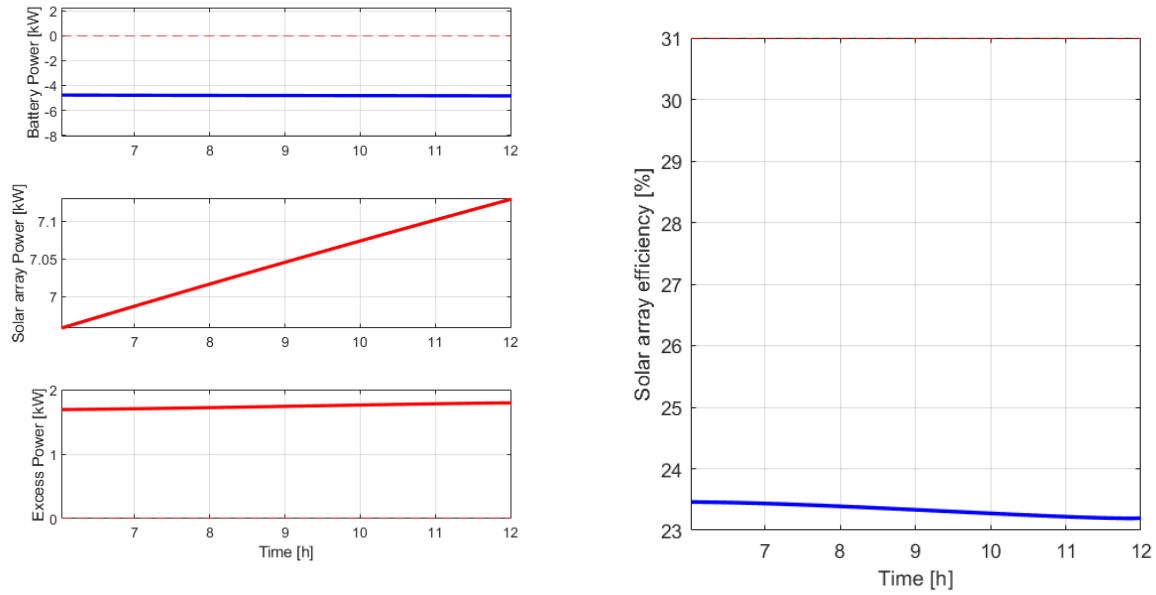

(a) **(b)**

Figure 4.13: (a) From top to bottom: power absorbed by the battery, power delivered by the array and the resulting power excess during Overpower phases; (b) Solar array efficiency shift from optimal 31%.

As a consequence of the low power demanded by the subsystems, the panel is oversized for the Standby phase, resulting in excess power (Figure 4.13a) and a reduction in panel efficiency (Figure 4.13b) from 31% to an average of 23.5%.

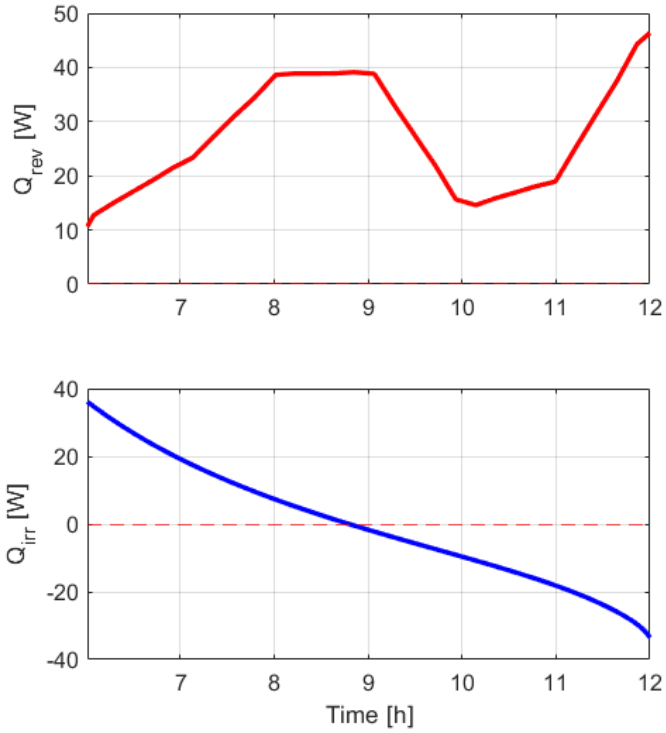

Figure 4.14: Reversible Q_{rev} and irreversible Q_{irr} terms of generated heat Q_g during Standby phase.

As previously discussed, being a charging phase, the irreversible component of the generated heat becomes negative as the battery voltage increases, producing a cooling effect with increasing electrical efficiency (Figure 4.12b).

4.3 Mission Scenarios

In this formulation, the system sizing is driven by the mission scenario. In order to develop different mission scenarios to analyse, it is necessary to identify the governing parameters, namely: the type of phase (1 or 2), the required power (assumed constant or linear), and the duration of each phase. To extend the battery lifetime, a maximum charging current expressed as a C-rate of $0.2\,C$ is assumed, together with a depth of discharge (DoD) up to 80%, both to extend the operational life of the battery and to comply with the accuracy constraints of the adopted models.

The power supplied by the solar array to meet the load demand is regulated by a maximum power point tracker (MPPT), as discussed in Section 3.2.2. Once the battery is fully recharged and the available array power exceeds the load demand, the power balance is maintained by shifting the operating point along the V-I characteristic toward lower current values while keeping a voltage suitable for distribution. This corresponds to operating on the right side of the maximum power point (MPP) in Figure 3.41, where the current is reduced while the voltage remains approximately constant, resulting in an efficiency drop as shown in Figure 4.13b.

For the proposed scenarios, the characteristics governing the simulation are specified in Table 4.3.

Table 4.3: Simulation parameters for the proposed scenarios.

Parameter	Value	Unit
V_{bus}	330	V
T_{amb}	20	$^{\circ}C$
BED_{sys}	225	Wh/kg
Volumetric density	600	Wh/L
Maximum charging current	0.2	C
Reference battery temperature	20	°C
$A_{surf,pack}$ (battery pack surface area)	6	m^2
η_g	90	%
Solar array packing factor	0.7	-
SOC_t (standby mode)	99	%
SOC_{lim}	20	%
L (total cable length)	10	m

Since the power system solutions analysed do not consent for long-range night operation, the mission scenarios will be defined with a maximum time of 10 days. For the representative mission scenarios, the solar array radiative configuration includes both front and back surfaces.

Each transfer phase is preceded by a standby phase, if $SOC < SOC_t$, in order to ensure maximum available energy prior to battery high-power demand operations. Illumination conditions are assumed to be optimal over the entire mission duration, consequently, the initial solar incidence angle is selected according to the mission length to ensure the optimal illumination condition; for instance, for a 72-hour mission, the initial Sun incidence angle is set to -26° and increases up to $+26^{\circ}$ over the considered time window. This range is selected to allow the solar array to exploit optimal illumination conditions, corresponding to the interval of lowest incidence angles and therefore the most favorable power generation regime.

To size the battery pack, it is necessary to define the values of P_r and t_r. Increasing these parameters leads to an increase in the energy capacity and, consequently, in the overall mass of the pack. Since both parameters have the same influence on the final mass of the battery pack, the sizing procedure can be carried out by varying only P_r and maintaining a constant value for t_r. Essentially, this means that the battery pack is capable of delivering a constant power P_r for a duration equal to t_r.

To ensure that the battery SOC does not fall below the minimum limit of 20%, the procedure shown in Figure 4.15 is employed.

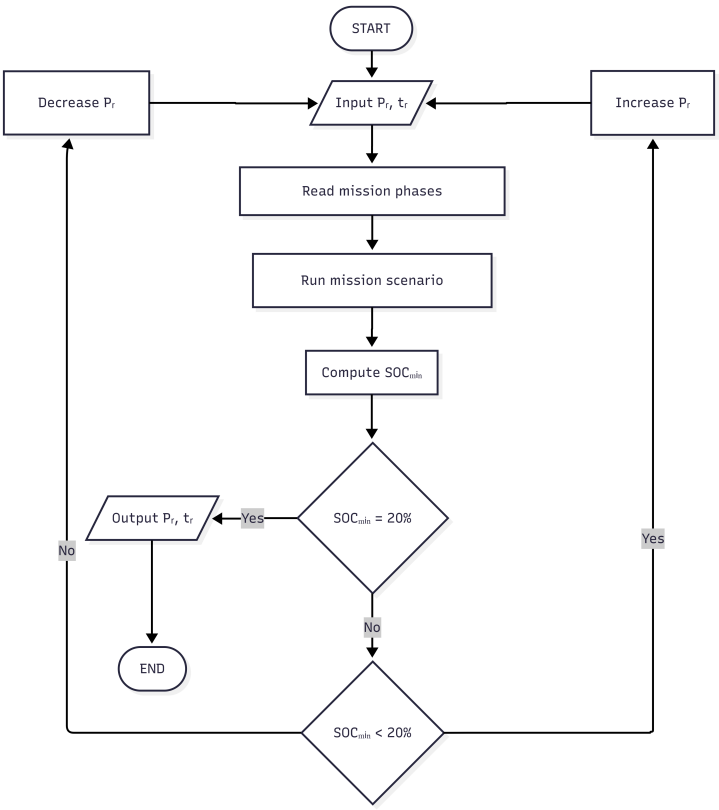

Figure 4.15: Scheme of the procedure employed to determine the optimal value of P_r for battery pack sizing.

Assuming the power requirements for each phase within the scenario, an initial value of P_r is set equal to the power during the first Transfer phase, with t_r set accordingly. The battery pack mass at system level is then calculated via Equation 4.1. The cable mass is also included in the calculation.

$$W_{\text{pack}} = \frac{P_r \cdot t_r}{(1 - SOC_{lim}) \cdot BED_{sys} \cdot \eta_g} + \bar{m}_{cable} \cdot L \tag{4.1}$$

The optimal value of P_r is then determined to minimize the mass of the battery pack.

4.3.1 Scenario 1

The first suggested scenario is a short-duration mission of around 5 days for a total of 18 hours of transfer range. The mission consists of reaching three surface targets (A, B, and C), each accessible through a dedicated 6-hour Transfer phase. At each site, operational activities are performed, characterized by different power requirements depending on the specific tasks to be executed.

The operational timeline is structured into successive transfer, science, overpower, and standby phases, as detailed in Table 4.4.

Table 4.4: Mission profile of Scenario 1, with operational phases grouped by exploration sites and return operations, each described by power and duration.

#	Phase	Power [kW]	Dur. [h]	#	Phase	Power [kW]	Dur. [h]
Transfer to site A				***Transfer to site C***			
1	Transfer	4.0	6.0	13	Transfer	4.0	6.0
Science site A				***Science site C***			
2	Science	3.0	5.0	14	Science	1.5	3.0
3	Overpower	10.0	6.0	15	Overpower	10.0	6.0
4	Science	1.5	3.0	16	Science	3.0	5.0
Transfer to site B				17	Overpower	12.0	6.5
5	Transfer	4.0	6.0	18	Science	2.0	5.0
Science site B				19	Overpower	10.0	6.0
6	Science	1.5	4.0	20	Science	3.0	4.0
7	Overpower	10.0	6.0	***Return phases***			
8	Overpower	8.0	4.0	21	Return	4.0	6.0
9	Science	2.0	5.0	22	Standby	0.5	5.01
10	Overpower	12.0	6.0	23	Return	4.0	6.0
11	Science	3.0	6.0	24	Standby	0.5	5.23
12	Science	1.5	2.0	25	Return	4.0	6.0

The scenario assumes the rover reaches Site A after an initial 6-hour transfer requiring 6000 W. At this location, scientific operations are performed at a baseline of 3000 W, with critical segments where additional battery support is necessary to sustain Overpower peaks of 10000 W. The mission continues toward Site B and subsequently Site C. During these phases, the power demand for propulsion remains stable at 6000 W, but the scientific activities become more demanding. Specifically, at Site B and Site C, the rover alternates between nominal science periods and multiple overpower cycles, reaching power demands of up to 12000 W (Phases 10 and 17 of Table 4.4). These high-load phases model specific high-energy scientific tasks performed at the target locations, which significantly impact battery depletion.

Finally, the mission enters the Return phases, dedicated to the journey back to the base. This segment is characterized by a series of Return maneuvers (6000 W) interspersed with Standby periods (500 W). These standby intervals, lasting approximately 5 hours each, are strategically placed to allow for battery recharging, ensuring sufficient energy availability to complete the final traversal and reach the base safely.

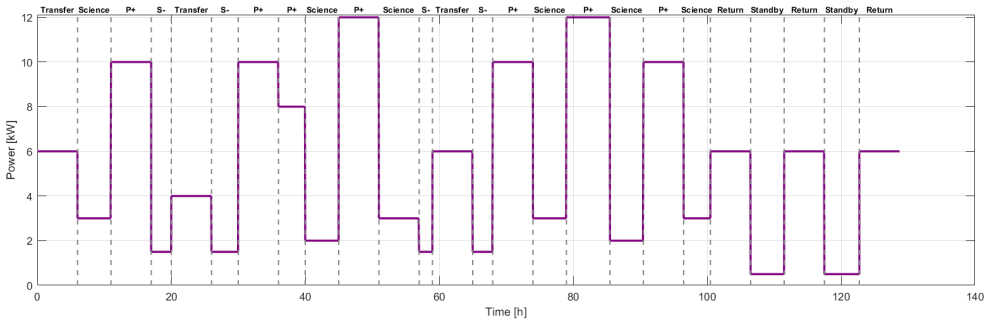

Figure 4.16: Scenario 1 requested power profile throughout the mission.

Figure 4.16 illustrates the proposed power profile for Scenario 1. Low-power phases correspond to science and $S-$ (Science phases with lower power), and power peaks ($P+$) occur during overpower phases. The Science phases are also indicated, during which power demand is moderate and the battery is recharged via the solar array.

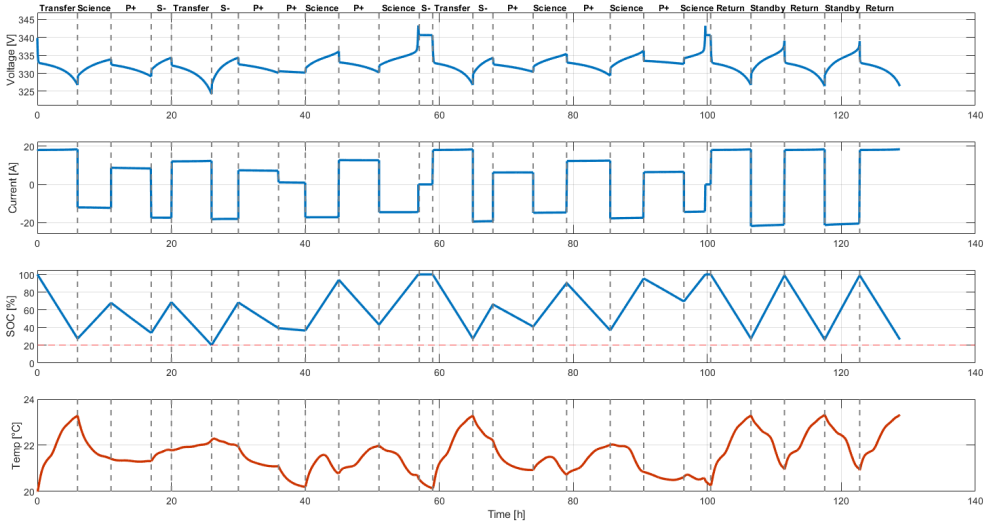

Figure 4.17: Scenario 1 battery pack parameters. From top to bottom are reported the voltage, current, SOC (with a red dotted line to indicate the SOC limit of 20%) and temperature profile throughout the mission.

Figure 4.17 illustrates the general status of the battery in terms of supplied voltage and current, with positive values corresponding to discharge and negative values to charging. The state of charge (SOC) is monitored accordingly. In the SOC plot, a red dashed line indicates an 80% DoD, beyond which the accuracy of the electrical model decreases, as discussed in Section 3.1.4.

The maximum temperature reached is 23.22°C, which is relatively low since the discharge current is small (on average approximately 0.1 C), allowing a gradual battery discharge without significant overheating. The temperature peaks are associated with the end of the Transfer phases, during which the battery has been extensively used.

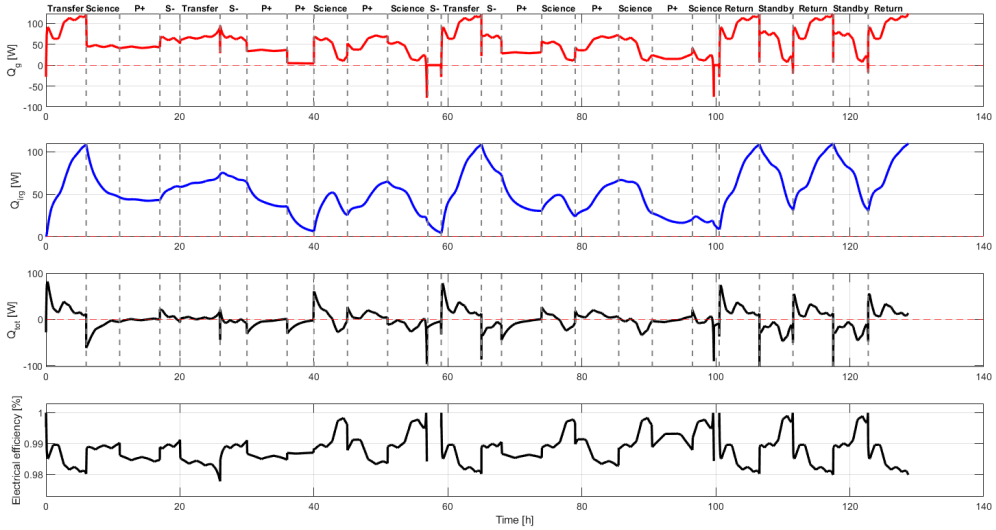

Figure 4.18: Scenario 1 thermal perspective. From top to bottom are reported the generated heat Q_g, radiative heat Q_{irg}, total heat Q_{tot} and electrical efficiency profile throughout the mission.

In the temperature graph of Figure 4.17, discharge phases are associated with temperature increases, while charging phases exhibit a temperature decrease. This behavior results from lower heat generation during charging, as shown in the second graph of Figure 4.18, particularly for $SOC > 70\%$, where the total heat is negative ($Q_{tot} < 0$) results in battery cooling. This effect is due to the reversible heat term Q_{rev} which for charging state follows backwards the dU/dT curve illustrated in Figure 3.21.

The irradiated heat follows a curve qualitatively similar to the temperature profile in Figure 4.17, since it is directly linked to the cell temperature and the corresponding radiative exchange with the environment. It is also reported the electrical efficiency of the battery pack, with an overall value always above 97%.

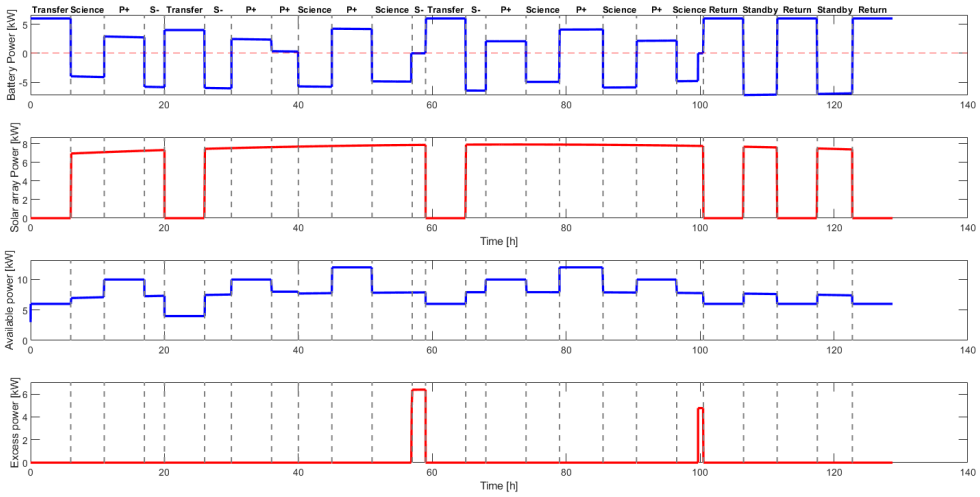

Figure 4.19: From top to bottom: Scenario 1 battery power (negative when absorbed, positive when delivered); available power from the solar array; total available power computed as the sum of battery and solar array contributions; excess power from the solar array.

Figure 4.19 illustrates the power contributions of the energy sources installed on the rover. In particular, it shows power excess during Science operations (Phases 4 and 20 of Table 4.4), when the batteries reach full charge and are temporarily disconnected to preserve their state of charge. During these power excess periods, the solar array operates at reduced efficiency, as shown in Figure 4.20.

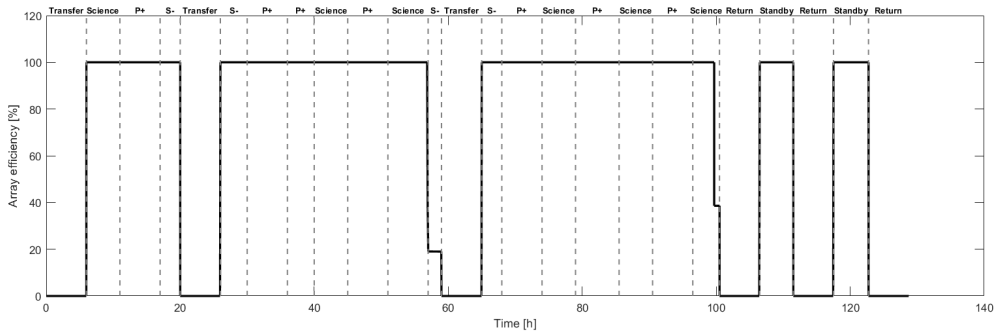

Figure 4.20: Percentage of the available solar array power that is effectively used; 100% corresponds to the utilization ratio, not to the conversion efficiency.

In this configuration, the battery and solar panel are sized to support the rover's continuous operations and power requirements, with the respective output dimensions reported in Table 4.5.

Table 4.5: Electrical and power subsystem specifications, including wiring parameters, energy storage and generation characteristics, and overall mass budget for Scenario 1.

Category	Parameter	Value
Wiring Specifications (AWG 8)		
	Max Current / Voltage	$21.89\,A$ / $343.32\,V$
	Conductor Radius	$0.1632\,cm$
	Insulation Thickness	$0.1069\,cm$
	Specific Mass	$0.131\,kg/m$
Energy Storage & Generation		
	Battery Pack Energy	$43.4\,kWh$
	Battery Pack Mass	$192.59\,kg$
	Battery Pack Volume	$0.0722\,m^3$
	Solar Array Area	$24.00\,m^2$
	Solar Array Mass	$72.00\,kg$
	Max Solar Power	$7.93\,kW$
	Max Battery Temperature	$23.32\,°C$
System Totals		
	Cable Mass (10m)	$1.314\,kg$
	Total Power System Mass	**264.72 kg**

4.3.2 Scenario 2

The second sizing scenario is a long-duration mission of around 10 days for a total of 40 hours of transfer range. The mission consists of reaching three surface targets (A, B, C and D), each accessible through a dedicated 10-hour Transfer phase. At each site, operational activities are performed, characterized by different power requirements depending on the specific tasks to be executed.

The operational timeline is structured into successive transfer, science, overpower, and standby phases, as detailed in Table 4.6.

Table 4.6: Mission profile of Scenario 2, with operational phases grouped by exploration sites and return operations, each described by power and duration; Phase 7 indicates a linear power increase from 7.5 kW to 10.5 kW.

#	Phase	Power [kW]	Dur. [h]	#	Phase	Power [kW]	Dur. [h]
Transfer to site A				***Science site C (cont.)***			
1	Transfer	7.5	10.0	21	Science	3.0	6.00
Science site A				22	Science	1.0	6.00
2	Science	1.0	2.00	23	Overpower	11.0	6.00
3	Science	3.0	6.00	24	Science	3.0	6.00
4	Science	1.0	6.00	25	Overpower	11.0	2.00
5	Science	3.0	6.00	26	Science	1.0	6.00
6	Standby	0.5	7.95	27	Science	3.0	6.00
Transfer to site B				28	Science-	1.0	6.00
7	Transfer+	7.5 → 10.5	4.00	***Transfer to site D***			
8	Transfer	7.5	6.00	29	Transfer	7.5	10.0
Science site B				***Science site D***			
9	Science	1.0	2.00	30	Science	1.0	2.00
10	Science	3.0	6.00	31	Science	3.0	6.00
11	Overpower	11.0	4.00	32	Science	1.0	6.00
12	Science	1.0	6.00	33	Science	3.0	6.00
13	Overpower	12.5	4.00	***Return phases***			
14	Standby	0.5	10.15	34	Return	7.5	5.00
15	Overpower	11.0	4.00	35	Standby	0.5	5.25
16	Science	3.0	6.00	36	Return	7.5	5.00
17	Science	1.0	2.00	37	Standby	0.5	5.59
Transfer to site C				38	Return	7.5	5.00
18	Transfer	7.5	10.0	39	Standby	0.5	5.85
Science site C				40	Return	7.5	5.00
19	Science	1.0	2.00	41	Standby	0.5	6.21
20	Overpower	11.0	6.00	42	Return	7.5	10.0

The mission profile for Scenario 2 is structured around four distinct exploration sites (A, B, C, and D). The rover reaches Site A following a 10 hour initial transfer at a constant 7.5 kW. At this location, scientific operations are conducted with a baseline demand of 1.0-3.0 kW. To ensure energy availability, the mission includes Standby periods (0.5 kW) to reach SOC_t before proceeding into more power demanding phases. The transition to Site B introduces a Transfer+

(Phase 7 in Table 4.6), which assumes the traversal of a positively sloped terrain, where the power demand increases linearly from 7.5 kW to 10.5 kW followed by a nominal transfer phase at constant power of 7.5 kW.Once at Site B and subsequently Site C, the rover performs stationary high-intensity tasks designed to exploit the high availability of solar energy (Figure 4.24). These are characterized by multiple Overpower cycles with peak demands reaching 12.5 kW (Phase 13). These segments represent energy-intensive activities with payload powered by the rover, such as ISRU or high-resolution analysis, which necessitate battery pack support. The exploration concludes at Site D, followed by the Return phases.

A specific energy management strategy is adopted for the journey back to base: instead of performing full recharges, the State of Charge (SOC) is intentionally limited to a lower safe threshold. By avoiding the slower, final stages of the battery charging cycle, the standby intervals can be kept shorter (between 4.8 and 6.2 h). The last trasnfer phase is a continuative 10 hours travel. This approach optimizes the overall mission time while still ensuring sufficient energy margins for the 7.5 kW return maneuvers. These strategically timed pauses allow the rover to complete the final traversal maintaining enough energy to reach the base without unnecessary delays.

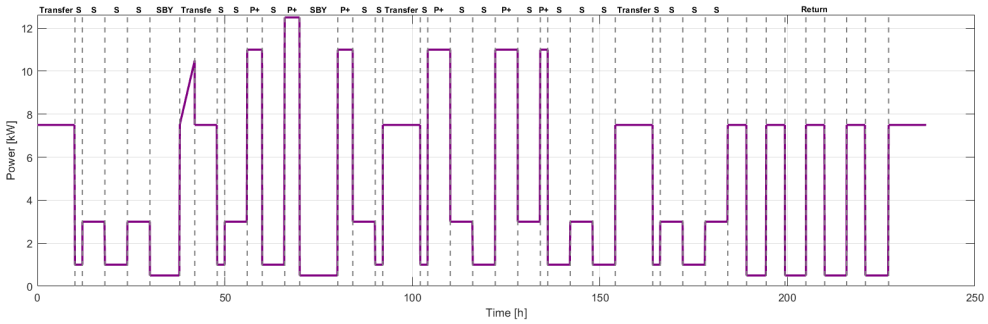

Figure 4.21: Scenario 2 requested power profile throughout the mission; The final return phases are indicated as a unique Return which include sequence of standby and mobility as indicated in Table 4.6.

Figure 4.21 illustrates the calculated power profile for Scenario 2, highlighting a more demanding profile compared to Scenario 1. The Transfer segments are characterized by a baseline demand of 7.5 kW, with a visible linear increase during the Transfer+ phase (Phase 7) to account for sloped terrain traversal. The Science phases indicated as "*S*" (1.0–3.0 kW) represent operational windows where the power demand is lower than the solar array's generation capacity, allowing for periodic energy recovery.

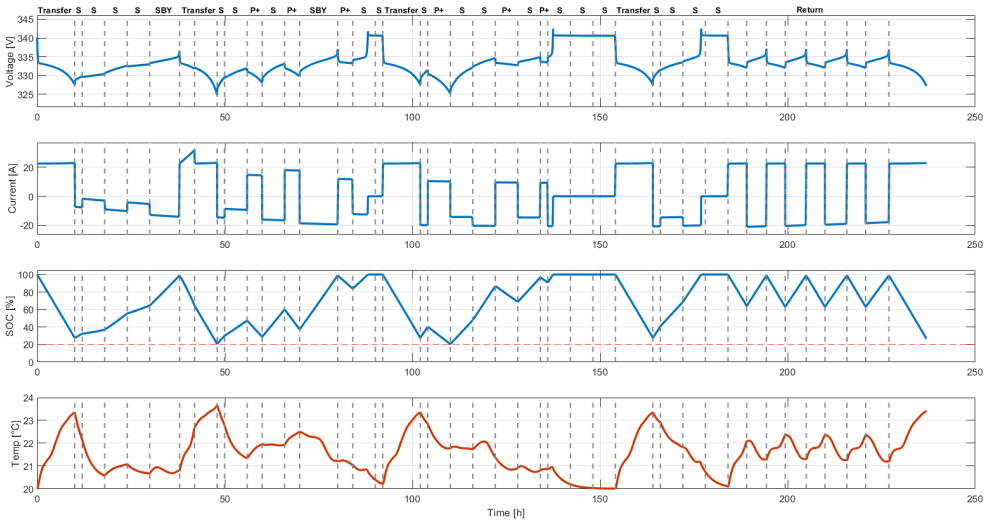

Figure 4.22: Scenario 2 battery pack parameters. From top to bottom are reported the voltage, current, SOC (with a red dotted line to indicate the SOC limit of 20%) and temperature profile throughout the mission; The final return phases are indicated as a unique Return which include sequence of standby and mobility as indicated in Table 4.6.

Figure 4.22 illustrates the battery's operational status throughout Scenario 2. The voltage and current profiles reflect the mission sequence, where positive current values indicate discharge phases and negative values signify charging periods via the solar array. The State of Charge plot (in Figure 4.22 the third from top) effectively highlights two standby phases outside of the Return section which was not present in Scenario 1; this indicates that a priority recharge is necessary before the transfer to site B (Phase 7 and 8) and between overpower phases in site B (Phases 13 and 15). It is also possible to notice a large segment of three consecutive science phases (26, 27 and 28) in site C, where the battery is fully charged and the associated null current and the voltage fixed at V_{full} indicates that it holds full capacity. The thermal behavior remains stable, with a maximum temperature of 23.61 $^{\circ}C$.

Despite the presence of high-power peaks (up to 12.5 kW), the average discharge current remains relatively low (approximately 0.05 C), preventing significant overheating. Consistent with the energy demand, the temperature peaks are primarily located at the end of the Transfer and Transfer+ phases, where the prolonged traction effort leads to sustained battery utilization, and during the dense sequences of overpower cycles at site C and site D where the battery support the solar array power output. During the Return phases, the temperature remains approximately 22 °C, as the short charge and discharge cycles, reaching a maximum depth of discharge of about 40%, do not allow sufficient time for significant thermal accumulation or dissipation within the battery; then reaches around 23 $^{\circ}C$ at the end of the last return phase.

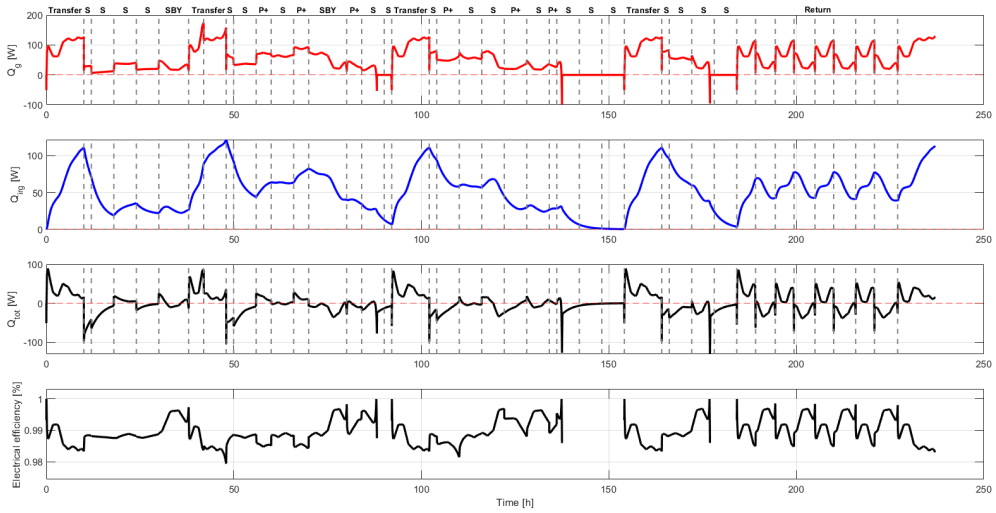

Figure 4.23: Scenario 2 thermal perspective. From top to bottom are reported the generated heat Q_g, radiative heat Q_{irg}, total heat Q_{tot} and electrical efficiency profile throughout the mission; The final return phases are indicated as a unique Return which include sequence of standby and mobility as indicated in Table 4.6.

In the temperature profile shown in Figure 4.22, discharge phases are correlated with temperature increases, whereas charging phases lead to a decrease in temperature. The same trend was observed in Scenario 1; therefore, the corresponding considerations remain valid here. The electrical efficiency of the battery pack is also reported, with an overall value consistently above 97%. Isolated gaps in the efficiency curve are visible and correspond to periods in which the battery pack is not actively operating.

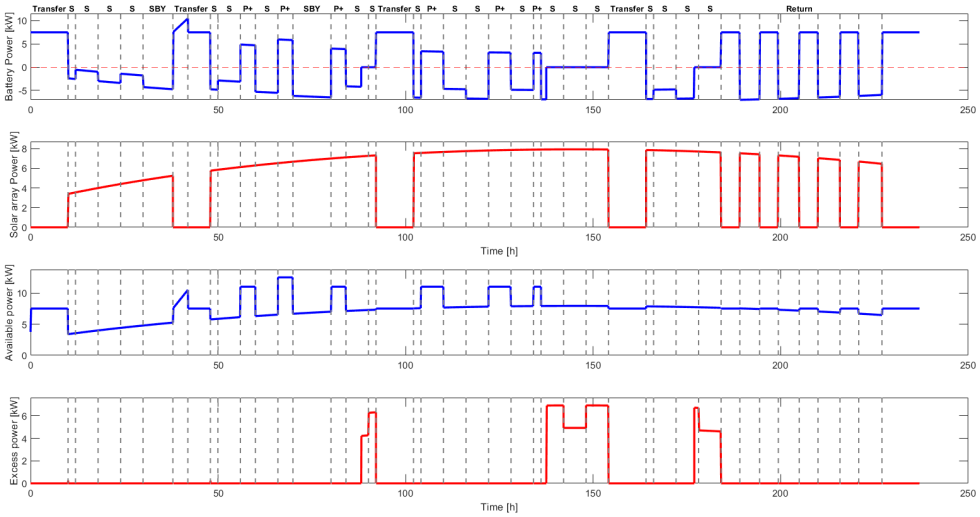

Figure 4.24: From top to bottom: Scenario 2 battery power (negative when absorbed, positive when delivered); available power from the solar array; total available power computed as the sum of battery and solar array contributions; excess power from the solar array.

Figure 4.24 illustrates the power contributions and the energy balance between the rover's

onboard power sources. The profile reveals several intervals of power surplus, the first in science phases (16 and 17), a larger section in science phases 26, 27 and 28 and a last segment in science phases 32 and 33 prior to the return. In these phases, solar generation exceeds the instantaneous rover demand while the battery pack has already reached its maximum state of charge (100% SOC).

To prevent overcharging and ensure battery longevity, the charging current is interrupted, and the battery is temporarily isolated from the power bus. Consequently, during these surplus intervals, the solar array operates in a reduced-power regime, as shown in Figure 4.25, since the excess generated power cannot be delivered to the system.

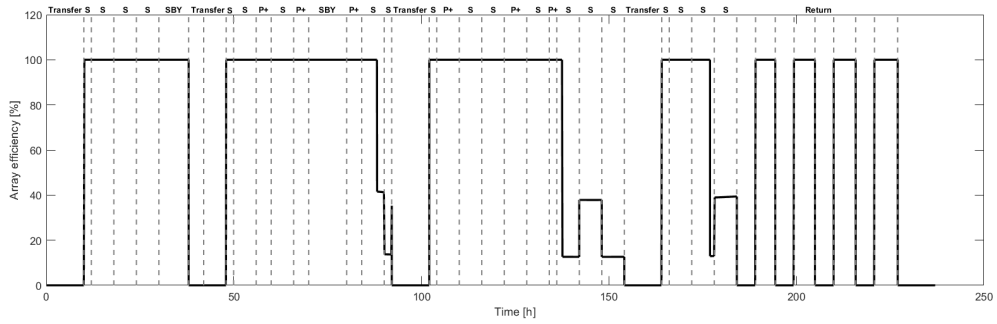

Figure 4.25: Percentage of the available solar array power that is effectively used in Scenario 2; 100% corresponds to the utilization ratio, not to the conversion efficiency.

In this configuration, the battery and solar panel are sized to support the rover's continuous operations and power requirements, with the respective output dimensions reported in Table 4.7.

Table 4.7: Electrical and power subsystem specifications, including wiring parameters, energy storage and generation characteristics, and overall mass budget for Scenario 2.

Category	Parameter	Value
Wiring Specifications (AWG 6)		
	Max Current / Voltage	$31.65\,A$ / $342.50\,V$
	Conductor Radius	$0.2057\,cm$
	Insulation Thickness	$0.1068\,cm$
	Specific Mass	$0.184\,kg/m$
Energy Storage & Generation		
	Battery Pack Energy	$90.0\,kWh$
	Battery Pack Mass	$400.00\,kg$
	Battery Pack Volume	$0.1500\,m^3$
	Solar Array Area	$24.00\,m^2$
	Solar Array Mass	$72.00\,kg$
	Max Solar Power	$7.93\,kW$
	Max Battery Temperature	$23.67\,°C$
System Totals		
	Cable Mass (10m)	$1.842\,kg$
	Total Power System Mass	**472.18 kg**

Scenarios comparison

Scenario 1 presents a lower maximum current ($21.89\,A$) compared to Scenario 2 ($31.65\,A$). Therefore, as shown in Tables 4.5 and 4.7, Scenario 1 is associated with a smaller and lighter AWG cable than Scenario 2. The insulation thickness is nearly identical in both cases due to the same operating voltage, while the main difference lies in the conductor radius, which is larger in Scenario 2.

The mass of the battery pack alone, computed through Equation 4.1, is directly proportional to the value of P_r. A different trend is observed for the total propulsion system mass, since the same solar array is adopted in both scenarios, resulting in a fixed parameter that does not depend on the selected power profile for a preliminary analysis.

Regarding thermal behavior, the heat generation is higher in Scenario 2, as it is strongly correlated with the delivered current. A similar consideration applies to the battery temperature as the current peaks in Scenario 2 occur in discharge phases and, due to their higher magnitude compared to Scenario 1, lead to a slightly higher maximum temperature. The relatively limited increase in peak temperature, despite an approximately 45% higher current, can be attributed to the larger thermal capacity C_{th} of the battery pack in Scenario 2; assuming the same BED_{sys}, a heavier battery results in a higher thermal capacity, which mitigates the temperature rise.

5 Conclusions

This work follows the development of a parametric model of the propulsion system for a pressurized lunar rover, starting from a detailed study of the state of the art that led to the definition of a solar array propulsion supported by a battery pack. This configuration represents the first iteration to assess the characteristics and performance of the propulsion system. The research therefore focused on the simulation of lithium-ion battery packs and solar panels with GaAs multijunction cells, which currently represent the most performant solution, supported by a robust historical and technological background that ensures their effectiveness.

Once the architectures to be analysed were defined, the Shepherd model was implemented to simulate the battery behavior at the cell level. This mathematical model proved to be very inexpensive in terms of computational cost while showing reliable precision for SOC levels above 20%, which is consistent with the characteristics of lithium batteries, as they maintain stable performance over time in line with the SOC limit assumed in the model. The extension of this model to a battery pack introduced the discussion of fundamental parameters such as MPF, power-train losses, and the analysis required for the selection of suitable distribution cables according to the SVD model, in order to scale the cell dimensions up to the system level. The robustness of the model was then validated against experimental data available in the literature, confirming its accuracy and enabling a detailed analysis of the electrical parameters of the battery pack.

To assess the thermal behavior of the battery, a 0D model of the single cell was implemented, allowing the evaluation of the generated, dissipated, and total heat, quantifying the temperature increase as a function of the imposed current regime, while accounting for the effects of temperature on the electrical parameters of the Shepherd model. This model demonstrated good accuracy under low current conditions (around 1C) for both temperature and heat evaluations, making it suitable for the simulated scenarios where the current rarely exceeds 0.2C. The uncertainties were more pronounced at higher C-rates (2C and 3C), which are not used in real-time operation for electrical mobility due to the high thermal stresses they impose on the battery. The transition from cell to battery pack in the thermal model proved to be more limiting in terms of accuracy, since it required the introduction of a strong assumption that considers all the cells of the battery pack to be managed by a thermal control system that homogenizes their temperature.

Having both models available, it was possible to identify an optimal voltage at $330\,V$, together with the total surface area of the battery pack ($6\,m^2$) that allows a limited temperature increase, while comfortably satisfying the space constraints assumed within the rover structure.

The solar array was modeled in the final stage of the analysis. Starting from the single cell through the Single Diode Model, it was possible to provide a first evaluation of the cell performance. However, the model is affected by some limitations, such as the assumption of the ideality factor and the use of a single diode to represent the p-n junction, which reduces the capability to accurately predict leakage currents, while remaining highly reliable for a preliminary assessment. The main losses mechanisms were also analysed in order to highlight the effects of the lunar environment, and a preliminary estimation of the array operating temperature was provided. The results show improved performance when both faces of the array are allowed to radiate heat, in both EOL and BOL cases. For the required solar array area, several power cases were analysed, showing that for power levels between 2000 and 7000 kW the required area remains relatively limited.

The entire analysis was implemented in a dedicated tool that enables a first battery pack sizing according to an input design power profile; however, it still lacks the capability to determine the

optimal solar array area in order to further reduce excess power. As outputs, it provides a global overview of both electrical and thermal aspects of the two systems, allowing the immediate identification of potential mission-critical issues. For simplicity, only constant or, at most, linearly varying power profiles were considered in order to represent a conservative envelope of more complex operating conditions. However, the tool is capable of providing accurate predictions even for highly variable power profiles.

The two analysed scenarios highlighted the clear advantages introduced by the coupling of a solar array with an energy storage system based on batteries, compared to the significant limitations that would arise when considering the two architectures separately.

5.1 Future work

Future developments will focus on extending the current framework in order to further enhance its predictive capability and system-level completeness. First, the methodology for solar array sizing should be expanded to allow a precise determination of the required array area based on the available excess power, in a manner analogous to the approach adopted for battery sizing through the definition of the reference power P_r. This would enable a fully consistent optimization of both generation and storage subsystems.

In addition, the discussion and implementation of alternative power generation technologies will be pursued. In particular, models for systems not directly addressed in this work but extensively analysed in the state of the art, such as fuel cells (both conventional and regenerative) and RTGs, will be developed. The inclusion of these non-solar power sources would significantly broaden the range of feasible rover architectures and operational strategies, enabling mission profiles characterized by extended eclipse periods in which solar arrays cannot be relied upon. This extension would therefore improve the operational flexibility of the rover and allow its deployment in more demanding environmental conditions.

Further improvements may also concern the refinement of the individual battery and photovoltaic models. On the electrical side, model accuracy could be enhanced, particularly in the low state-of-charge region below 20%, by adopting more advanced formulations. On the thermal side, the current 0D approach may be extended to higher-dimensional models (1D, 2D, or 3D), enabling cell-by-cell thermal monitoring and a more detailed evaluation of heat generation, temperature distribution, and the resulting impact on electrical efficiency. A more detailed analysis of the powertrain will also be required, explicitly modelling losses and efficiencies associated with the mechanical components responsible for power distribution. Finally, the complete models will be integrated into a more comprehensive system-level framework capable of receiving inputs from all rover subsystems, thereby accurately quantifying power demands and geometric constraints.

Bibliography

[1] 3JIndustry. *American Wire Gauge (AWG) Sizes and Properties Chart / Table*. https://www.3jindustry.com/blogs/news/98462150-american-wire-gauge-awg-sizes-and-properties-chart-table. 2016.

[2] Abdelrahman O. Ali et al. "Advancements in photovoltaic technology: A comprehensive review of recent advances and future prospects". In: *Energy Conversion and Management: X* 26 (2025), p. 100952. ISSN: 2590-1745. DOI: https://doi.org/10.1016/j.ecmx.2025.100952. URL: https://www.sciencedirect.com/science/article/pii/S2590174525000844.

[3] Richard M. Ambrosi et al. "European Radioisotope Thermoelectric Generators (RTGs) and Radioisotope Heater Units (RHUs) for Space Science and Exploration". In: *Space Science Reviews* (2019).

[4] Eliot Aretskin-Hariton et al. "Power Cable Mass Estimation for Electric Aircraft Propulsion". In: *AIAA Aviation Forum and Exposition*. NASA Technical Reports Server, 2021.

[5] S.Calabrese Barton et al. "Mixed-reactant, strip-cell direct methanol fuel cells". In: *Journal of Power Sources* 96.2 (2001), pp. 329–336. ISSN: 0378-7753. DOI: https://doi.org/10.1016/S0378-7753(00)00663-7. URL: https://www.sciencedirect.com/science/article/pii/S0378775300006637.

[6] Munkhbayar Batmunkh et al. "Nanocarbons for Mesoscopic Perovskite Solar Cells". In: *Journal of Materials Chemistry A: Materials for Energy and Sustainability* (Feb. 2015). DOI: 10.1039/C5TA00873E.

[7] Manoj Bhardwaj et al. "Design of a pressurized lunar rover". In: (May 1992).

[8] Cheng F. C. "Insulation thickness determination of polymeric power cables". In: *IEEE Transactions on Dielectrics and Electrical Insulation* 1 (1994).

[9] Nicola Campagna et al. "Battery Models for Battery Powered Applications: A Comparative Study". In: *energies* (2020). DOI: 10.3390/en13164085.

[10] P. K. Cheo, R. Luther, and J. W. Porter. "Detection of Voids and Contaminations in Polyethylene Insulated Cable Utilization a FIR Laser Beam". In: *IEEE Transactions on Power Apparatus and Systems* PAS-102.2 (1983). Cited in Cheng (1994) as the source for defining 50μm as the maximum detectable void size with contemporary inspection techniques., pp. 521–526. ISSN: 0018-9510. DOI: 10.1109/TPAS.1983.317998.

[11] Marc Cohen. "Mobile Lunar and Planetary Bases". In: ().

[12] Matthew Cox et al. "The Lucy Spacecraft". In: *Space Science Reviews* 221 (Oct. 2025). DOI: 10.1007/s11214-025-01190-6.

[13] Javier Cubas, Santiago Pindado, and Carlos Manuel. "Explicit Expressions for Solar Panel Equivalent Circuit Parameters Based on Analytical Formulation and the Lambert W-Function". In: *Energies* 7 (June 2014), pp. 4098–4115. DOI: 10.3390/en7074098.

[14] DoITPoMS, Department of Materials, University of Cambridge. *Types of Fuel Cells Diagram*. https://www.doitpoms.ac.uk/tlplib/fuel-cells/figures/fuelcell_types_sml.png. Schematic comparison of different fuel cell types from the Fuel Cells teaching and learning package. DoITPoMS Teaching and Learning Package. URL: https://www.doitpoms.ac.uk/tlplib/fuel-cells/figures/fuelcell_types_sml.png.

[15] First Solar. *Cadmium Telluride (CdTe) Photovoltaic Technology*. https://www.firstsolar.com. Series 6–7 technology overview. 2022.

[16] Christophe Forgez et al. "Thermal modeling of a cylindrical LiFePO4/graphite lithium-ion battery". In: *Journal of Power Sources* 195.9 (2010), pp. 2961–2968. ISSN: 0378-7753. DOI: https://doi.org/10.1016/j.jpowsour.2009.10.105. URL: https://www.sciencedirect.com/science/article/pii/S037877530901982X.

[17] John Geisz et al. "Six-junction III–V solar cells with 47.1% conversion efficiency under 143 Suns concentration". In: *Nature Energy* 5 (2020). DOI: 10.1038/s41560-020-0598-5.

[18] R. D. Green, S. E. Elangovan, and F. Chen. "Perspective: Solid Oxide Cell Technology for Space Exploration". In: *Journal of The Electrochemical Society* 169.5 (2022). DOI: 10.1149/1945-7111/ac6a52.

[19] Rebecca Grinham and Andrew Chew. "A Review of Outgassing and Methods for its Reduction". In: *Applied Science and Convergence Technology* 26 (Sept. 2017), pp. 95–109. DOI: 10.5757/ASCT.2017.26.5.95.

[20] Grant H. Heiken, David T. Vaniman, and Bevan M. French. *Lunar sourcebook a user's guide to the moon*. Cambridge University press, 1991.

[21] Hanane Hemi, Nacer M'Sirdi, and Naamane Aziz. "A NEW PROPOSED SHEPHERD MODEL OF A LI-ION OPEN CIRCUIT BATTERY BASED ON DATA FITTING". In: Sept. 2019.

[22] Roland Holzbauer et al. "Cold Welding under Space and Launch Conditions". In: May 2024.

[23] Khaled Itani and Alexandre De Bernardinis. "Review on New-Generation Batteries Technologies: Trends and Future Directions". In: *Energies* 16 (Nov. 2023), p. 7530. DOI: 10.3390/en16227530.

[24] Maryam Kiani, Yan-Ling Zhao, and Rui-Qin Zhang. "Proton Exchange Membrane Fuel Cells: Recent Developments and Future Perspectives". In: *Chemical Communications* 61 (June 2025). DOI: 10.1039/D5CC01478F.

[25] Sam Koohi-Kamali et al. "Photovoltaic electricity generator dynamic modeling methods for smart grid applications: A review". In: *Renewable and Sustainable Energy Reviews* 57 (2016), pp. 131–172. ISSN: 1364-0321. DOI: https://doi.org/10.1016/j.rser.2015.12.137. URL: https://www.sciencedirect.com/science/article/pii/S1364032115015208.

[26] Jung-Hwan Lee, Sang-Kil Lim, and Kihan Kwon. "Optimization of multi-motor and multi-speed powertrain system for electric vehicles based on efficiency characteristics between motor and inverter". In: *Energy* 337 (2025), p. 138616. ISSN: 0360-5442. DOI: https://doi.org/10.1016/j.energy.2025.138616. URL: https://www.sciencedirect.com/science/article/pii/S0360544225042586.

[27] Yaqi Li et al. "Evolution of aging mechanisms and performance degradation of lithium-ion battery from moderate to severe capacity loss scenarios". In: *Chemical Engineering Journal* 498 (2024), p. 155588. ISSN: 1385-8947. DOI: https://doi.org/10.1016/j.cej.2024.155588. URL: https://www.sciencedirect.com/science/article/pii/S1385894724070797.

[28] David Linden, Thomas B. Reddy, and Kirby W. Beard. *Linden's Hanbook of Batteries, fifth edition*. McGraw-Hill Education, 2019.

[29] Hendrik Löbberding et al. "From Cell to Battery System in BEVs: Analysis of System Packing E ciency and Cell Types". In: *World Electric Vehicle Journal* (2020).

[30] LONGi Green Energy Technology. *Heterojunction Solar Cell Efficiency Breakthrough*. https://www.longi.com. Official company technical release. 2023.

[31] Antonio Luque and Steven Hegedus. *Hegedus, S.: Handbook of Photovoltaic Science and Engineering. Wiley, New York*. John Wiley and Sons, May 2003. ISBN: 9780471491965. DOI: 10.1002/0470014008.

[32] Vansh Malik et al. "Comparative study and analysis between Solid Oxide Fuel Cells (SOFC) and Proton Exchange Membrane (PEM) fuel cell – A review". In: *Materials Today: Proceedings* 47 (May 2021). DOI: 10.1016/j.matpr.2021.04.203.

[33] Luigi Mattia et al. "Lithium-ion battery thermal modelling and characterisation: A comprehensive review". In: *Journal of Energy Storage* 129 (2025), p. 117114. ISSN: 2352-152X. DOI: https://doi.org/10.1016/j.est.2025.117114. URL: https://www.sciencedirect.com/science/article/pii/S2352152X25018274.

[34] Noshin Omar et al. "Peukert Revisited—Critical Appraisal and Need for Modification for Lithium-Ion Batteries". In: *Energies* 6 (Oct. 2013), pp. 5625–5641. DOI: 10.3390/en6115625.

[35] Perovskite-Info.com. *An Introduction to Perovskites*. 2025. URL: https://www.perovskite-info.com/introduction.

[36] Redwire Space. *Roll-Out Solar Array (ROSA): Scalable. Powerful. State-of-the-art.* v1 10-2-2025. Redwire Space. Goleta, California, USA, Oct. 2025. URL: https://redwirespace.com.

[37] Catalina Romero-Guzmán, Isabel Pérez-Grande, and José A. Rodríguez-Manfredi. "Thermal model of InSight solar panels in Martian conditions". In: *Acta Astronautica* 202 (2023), pp. 476–484. ISSN: 0094-5765. DOI: https://doi.org/10.1016/j.actaastro.2022.10.045. URL: https://www.sciencedirect.com/science/article/pii/S0094576522005951.

[38] Asadullah Muhammad Hossain Saad. "Next-Generation Solar Cells: Advancements in Materials, Architectures, and System Integration for A Sustainable Energy Future." In: *American Journal of Innovation in Science and Engineering* 4 (May 2025), pp. 23–30. DOI: 10.54536/ajise.v4i2.3832.

[39] L.H. Saw et al. "Electro-thermal analysis of Lithium Iron Phosphate battery for electric vehicles". In: *Journal of Power Sources* 249 (2014), pp. 231–238. ISSN: 0378-7753. DOI: https://doi.org/10.1016/j.jpowsour.2013.10.052. URL: https://www.sciencedirect.com/science/article/pii/S0378775313017059.

[40] S. M. Shamim et al. "DESIGN, PERFORMANCE ANALYSIS AND EFFICIENCY OPTIMIZATION OF COPPER INDIUM GALLIUM SELENIDE (CIGS) SOLAR CELL". In: *European Scientific Journal* 11 (Feb. 2015).

[41] Solar Frontier. *High-Efficiency CIS Thin-Film Solar Cells*. https://www.solar-frontier.com. Corporate technology white paper. 2019.

[42] Daruich de Souza C. et all. "How does radioisotope thermoelectric generator (RTG) work". In: *Brazilian Journal of Radiation Sciences* (2022).

[43] SpectroLab, Boeing. *XTJ Standard Fluence Triple-Junction Space Solar Cell*. https://www.spectrolab.com/photovoltaics/XTE-SF_Data_Sheet.pdf. Space-grade solar cell product datasheet. 2021.

[44] Olivier Tremblay and Louis-A. Dessaint. "Experimental Validation of a Battery Dynamic Model for EV Applications". In: *World Electric Vehicle Journal* 3 (2009). DOI: 10.3390/wevj3020289.

[45] Ronald E. Turner. *Radiation Shielding (NASA Johnson Space Center, THREE article)*. 2009.

[46] Natascha von Aspern et al. "Phosphorus additives for improving high voltage stability and safety of lithium ion batteries". In: *Journal of Fluorine Chemistry* 198 (2017). Organofluorine Chemistry: Novel Developments – Bremen Fluorine Days, pp. 24–33. ISSN: 0022-1139. DOI: https://doi.org/10.1016/j.jfluchem.2017.02.005. URL: https://www.sciencedirect.com/science/article/pii/S0022113916303451.

[47] Nikolaos Voudoukis. "Photovoltaic Technology and Innovative Solar Cells". In: *European Journal of Electrical Engineering and Computer Science* 2 (Jan. 2018). DOI: 10.24018/ejece.2018.2.1.13.

[48] Patrick C. Vratny et al. "Battery Pack Modeling Methods for Universally-Electric Aircraft". In: *fourth CEAS Air and Space Conference* (2013).

[49] Cenqi Yan et al. "Non-fullerene acceptors for organic solar cells". In: *Nature Reviews Materials* 3 (Feb. 2018), p. 18003. DOI: 10.1038/natrevmats.2018.3.

[50] Shaik Zaidaan et al. "Advances in satellite thermal management systems: Challenges, innovations, and future directions". In: *Acta Astronautica* 244 (2026), pp. 82–121. ISSN: 0094-5765. DOI: https://doi.org/10.1016/j.actaastro.2026.02.002. URL: https://www.sciencedirect.com/science/article/pii/S0094576526000883.

[51] James Zakrajsek et al. "Exploration Rover Concepts and Development Challenges". In: 1 (Apr. 2005). DOI: 10.2514/6.2005-2525.

[52] Philipp Zanon, Michelle Dunn, and Geoffrey Brooks. "Current Lunar Dust Mitigation Techniques and Future Directions". In: *Acta Astronautica* 213 (2023), pp. 627–644. DOI: 10.1016/j.actaastro.2023.09.031.

[53] Robert Zarzycki, Andrzej Kacprzak, and Zbigniew Bis. "The Use of Direct Carbon Fuel Cells in Compact Energy Systems for the Generation of Electricity, Heat and Cold". In: *Energies* 11 (Nov. 2018), p. 3061. DOI: 10.3390/en11113061.

A Battery pack parameters extraction

This appendix describes how the main parameters of the battery pack model are derived from the corresponding cell-level quantities. The pack is assumed to be composed of n cells connected in series forming a module and m parallel modules.

The open-circuit voltage of the pack, $E_{0_{\text{pack}}}$, is obtained by summing the open-circuit voltages of the individual cells connected in series. Since each cell contributes equally to the total voltage, the pack open-circuit voltage scales linearly with the number of series-connected cells:

$$E_{0_{\text{pack}}} = E_{0_{\text{cell}}} \cdot n_s \tag{A.1}$$

The internal resistance of the pack, R_{pack}, depends on both series and parallel connections. Series-connected cells contribute additively to the total resistance, while parallel branches reduce the equivalent resistance. As a result, the pack resistance is obtained by scaling the cell resistance by the ratio between the number of series cells and the number of parallel branches:

$$R_{\text{pack}} = R_{\text{cell}} \cdot \frac{n_s}{m} \tag{A.2}$$

The polarization constant K, which accounts for voltage losses related to electrochemical polarization effects, follows the same scaling law as the internal resistance. This is due to the fact that polarization phenomena accumulate along series connections and are distributed across parallel paths:

$$K_{\text{pack}} = K \cdot \frac{n_s}{m} \tag{A.3}$$

The parameter A, associated with the exponential zone of the discharge curve, scales proportionally with the number of series-connected cells, as it contributes directly to the pack voltage behavior:

$$A_{\text{pack}} = A \cdot n_s \tag{A.4}$$

Finally, the parameter B, which characterizes the slope of the exponential voltage decay, is inversely proportional to the number of parallel branches. This reflects the fact that increasing the number of parallel cells effectively increases the available capacity and reduces the current load per cell:

$$B_{\text{pack}} = \frac{B}{m} \tag{A.5}$$

These scaling relationships allow the extension of a cell-level electrical model to a battery pack configuration while preserving the physical meaning of each parameter.

B AWG Table

Table B.1: American Wire Gauge (AWG) Cable / Conductor Sizes and Properties [1].

AWG	Diameter [mm]	Area [mm^2]	R [Ω/km]	Max I [A]	Max Freq
0000 (4/0)	11.684	107	0.16072	302	125 Hz
000 (3/0)	10.40384	85	0.202704	239	160 Hz
00 (2/0)	9.26592	67.4	0.255512	190	200 Hz
0 (1/0)	8.25246	53.5	0.322424	150	250 Hz
1	7.34822	42.4	0.406392	119	325 Hz
2	6.54304	33.6	0.512664	94	410 Hz
3	5.82676	26.7	0.64616	75	500 Hz
4	5.18922	21.2	0.81508	60	650 Hz
5	4.62026	16.8	1.027624	47	810 Hz
6	4.1148	13.3	1.295928	37	1100 Hz
7	3.66522	10.5	1.634096	30	1300 Hz
8	3.2639	8.37	2.060496	24	1650 Hz
9	2.90576	6.63	2.598088	19	2050 Hz
10	2.58826	5.26	3.276392	15	2600 Hz
11	2.30378	4.17	4.1328	12	3200 Hz
12	2.05232	3.31	5.20864	9.3	4150 Hz
13	1.8288	2.62	6.56984	7.4	5300 Hz
14	1.62814	2.08	8.282	5.9	6700 Hz
15	1.45034	1.65	10.44352	4.7	8250 Hz
16	1.29032	1.31	13.17248	3.7	11 kHz
17	1.15062	1.04	16.60992	2.9	13 kHz
18	1.02362	0.823	20.9428	2.3	17 kHz
19	0.91186	0.653	26.40728	1.8	21 kHz
20	0.8128	0.518	33.292	1.5	27 kHz
21	0.7239	0.41	41.984	1.2	33 kHz
22	0.64516	0.326	52.9392	0.92	42 kHz
23	0.57404	0.258	66.7808	0.729	53 kHz
24	0.51054	0.205	84.1976	0.577	68 kHz
25	0.45466	0.162	106.1736	0.457	85 kHz
26	0.40386	0.129	133.8568	0.361	107 kHz
27	0.36068	0.102	168.8216	0.288	130 kHz
28	0.32004	0.081	212.872	0.226	170 kHz
29	0.28702	0.0642	268.4024	0.182	210 kHz

AWG	Diameter [mm]	Area [mm^2]	R [Ω/km]	Max I [A]	Max Freq
30	0.254	0.0509	338.496	0.142	270 kHz
31	0.22606	0.0404	426.728	0.113	340 kHz
32	0.2032	0.032	538.248	0.091	430 kHz
33	0.18034	0.0254	678.632	0.072	540 kHz
34	0.16002	0.0201	855.752	0.056	690 kHz
35	0.14224	0.016	1079.12	0.044	870 kHz
36	0.127	0.0127	1360	0.035	1100 kHz
37	0.1143	0.01	1715	0.0289	1350 kHz
38	0.1016	0.00797	2163	0.0228	1750 kHz
39	0.0889	0.00632	2728	0.0175	2250 kHz
40	0.07874	0.00501	3440	0.0137	2900 kHz

C Single Diode Model parameter extraction

Zero derivative power at MPP

The output power is defined as $P = V \cdot I$. Differentiating with respect to V and applying the product rule yields:

$$\frac{dP}{dV} = \frac{d(VI)}{dV} = I + V\frac{dI}{dV} \tag{C.1}$$

At the maximum power point (MPP), the condition $\frac{dP}{dV} = 0$ must be satisfied, leading to:

$$I_m + V_m \left(\frac{dI}{dV}\right)_m = 0 \tag{C.2}$$

from which:

$$\left(\frac{dI}{dV}\right)_m = -\frac{I_m}{V_m} \tag{C.3}$$

Differentiating the single-diode model (Equation 3.64) with respect to V, and using implicit differentiation (since I appears on both sides), gives:

$$\frac{dI}{dV} = -\frac{I_0}{aV_T} \cdot \exp\left(\frac{V + I \cdot R_s}{aV_T}\right) \cdot \left(1 + R_s\frac{dI}{dV}\right) - \frac{1}{R_{sh}}\left(1 + R_s\frac{dI}{dV}\right) \tag{C.4}$$

Grouping the terms containing $\frac{dI}{dV}$:

$$\frac{dI}{dV}\left[1 + \frac{I_0 \cdot R_s}{aV_T}\exp\left(\frac{V + I \cdot R_s}{aV_T}\right) + \frac{R_s}{R_{sh}}\right] = -\frac{I_0}{aV_T}\exp\left(\frac{V + I \cdot R_s}{aV_T}\right) - \frac{1}{R_{sh}} \tag{C.5}$$

Solving explicitly for $\frac{dI}{dV}$:

$$\frac{dI}{dV} = \frac{-\frac{I_0}{aV_T}\exp\left(\frac{V+I\cdot R_s}{aV_T}\right) - \frac{1}{R_{sh}}}{1 + \frac{I_0 \cdot R_s}{aV_T}\exp\left(\frac{V+I\cdot R_s}{aV_T}\right) + \frac{R_s}{R_{sh}}} \tag{C.6}$$

Substituting the previous result into the MPP condition $\left(\frac{dI}{dV}\right)_m = -\frac{I_m}{V_m}$ yields:

$$-\frac{I_m}{V_m} = \frac{-\frac{I_0}{aV_T}\exp\left(\frac{V_m+I_m R_s}{aV_T}\right) - \frac{1}{R_{sh}}}{1 + \frac{I_0 R_s}{aV_T}\exp\left(\frac{V_m+I_m R_s}{aV_T}\right) + \frac{R_s}{R_{sh}}} \tag{C.7}$$

After algebraic rearrangement, this expression leads to the compact form reported as Equation C.8.

$$-\frac{I_m}{V_m} = -\frac{I_0}{aV_T}\left(1 - \frac{I_m \cdot R_s}{V_m}\right)\exp\left(\frac{V_m + I_m \cdot R_s}{aV_T}\right) - \frac{1}{R_{sh}}\left(1 - \frac{I_m}{V_m} \cdot R_s\right) \tag{C.8}$$

Solving R_s with Lambert function W [13]

The function $W(z)$, known as the *Lambert W-function*, is defined as the inverse of the relation

$$f(w) = we^w \tag{C.9}$$

In other words, if an equation can be written in the form

$$z = we^w \tag{C.10}$$

then the solution is given by

$$w = W(z) \tag{C.11}$$

Since the function we^w is not injective (i.e., it is not one-to-one over its entire domain), its inverse $W(z)$ is multivalued.

Restricting the analysis to real numbers, $W(x)$ is defined only for

$$x \geq -\frac{1}{e} \tag{C.12}$$

Within the interval $[-1/e,\ 0]$, the function admits two real branches:

- $W_0(x)$: the principal branch, satisfying $W(x) \geq -1$.
- $W_{-1}(x)$: the lower branch, satisfying $W(x) \leq -1$.

To solve exponential equations involving unknowns in both algebraic and exponential terms, the goal is to rearrange them into the standard form

$$Ye^Y = X \tag{C.13}$$

Once the equation is expressed in this form, the solution follows directly from the definition of the Lambert W-function:

$$Ye^Y = X \quad \Longleftrightarrow \quad Y = W(X) \tag{C.14}$$

The Equation to solve is

$$\frac{aV_TV_m(2I_m - I_{sc})}{(V_mI_{sc} + V_{oc}(I_m - I_{sc}))(V_m - I_mR_s) - aV_T(V_mI_{sc} - V_{oc}I_m)} = \exp\left(\frac{V_m + I_mR_s - V_{oc}}{aV_T}\right) \tag{C.15}$$

To simplify the expression, the following constants are introduced by grouping known terms:

$$K = aV_TV_m(2I_m - I_{sc}) \tag{C.16}$$
$$\alpha = V_mI_{sc} + V_{oc}(I_m - I_{sc}) \tag{C.17}$$
$$\beta = aV_T(V_mI_{sc} - V_{oc}I_m) \tag{C.18}$$
$$\gamma = \frac{V_m - V_{oc}}{aV_T} \tag{C.19}$$
$$\delta = \frac{I_m}{aV_T} \tag{C.20}$$

With these definitions, the equation can be rewritten as:

$$\frac{K}{\alpha(V_m - I_mR_s) - \beta} = \exp(\gamma + \delta R_s) \tag{C.21}$$

Rearranging the equation to isolate the exponential term:

$$\alpha V_m - \alpha I_mR_s - \beta = Ke^{-\gamma}e^{-\delta R_s} \tag{C.22}$$

Grouping the linear terms:

$$(\alpha V_m - \beta) - \alpha I_m R_s = K e^{-\gamma} e^{-\delta R_s} \tag{C.23}$$

Multiplying both sides by $e^{\delta R_s}$:

$$[(\alpha V_m - \beta) - \alpha I_m R_s]\, e^{\delta R_s} = K e^{-\gamma} \tag{C.24}$$

After algebraic manipulation, the equation is rewritten in the standard Lambert form:

$$Y e^{Y} = X \tag{C.25}$$

where

$$Y = \delta R_s - \frac{\delta(\alpha V_m - \beta)}{\alpha I_m}, \tag{C.26}$$

$$X = -\frac{\delta K}{\alpha I_m} \exp\left(-\gamma - \frac{\delta(\alpha V_m - \beta)}{\alpha I_m}\right) \tag{C.27}$$

Using the definition of the Lambert W function, and considering that $X < 0$:

$$Y = W_{-1}(X) \tag{C.28}$$

the series resistance is finally obtained as:

$$R_s = \frac{\alpha V_m - \beta}{\alpha I_m} + \frac{1}{\delta} W_{-1}\left(-\frac{\delta K}{\alpha I_m} \exp\left(-\gamma - \frac{\delta(\alpha V_m - \beta)}{\alpha I_m}\right)\right) \tag{C.29}$$

In MATLAB, this equation can be solved using the command $lambertw(k, x)$:

```
Rs = (alpha * Vm - beta) / (alpha * Im) + (1/delta) * lambertw(-1, X);
```

This syntax returns real values only if $k = 0$ or $k = -1$.

Shunt resistor R_{sh}

In contrast to R_s, no additional simplifications can be applied to derive R_{sh}. The complete Equation C.8 is first considered.

The exponential term is obtained from the current equation at the MPP (Equation 3.68).

$$I_0 \exp\left(\frac{V_m + I_m R_s}{a V_T}\right) = I_{pv} + I_0 - I_m - \frac{V_m + I_m R_s}{R_{sh}} \tag{C.30}$$

Substituting Equation C.30 into Equation C.8

$$-\frac{I_m}{V_m} = -\frac{1}{a V_T}\left(1 - \frac{I_m R_s}{V_m}\right)\left[I_{pv} + I_0 - I_m - \frac{V_m + I_m R_s}{R_{sh}}\right] - \frac{1}{R_{sh}}\left(1 - \frac{I_m R_s}{V_m}\right) \tag{C.31}$$

Separating the terms containing R_{sh}, factoring $\frac{1}{R_{sh}}$ and isolating $\frac{1}{R_{sh}}$:

$$\frac{1}{R_{sh}} = \frac{-\frac{I_m}{V_m} + \frac{1}{a V_T}\left(1 - \frac{I_m R_s}{V_m}\right)\left(I_{pv} + I_0 - I_m\right)}{\Phi} \tag{C.32}$$

where

$$\Phi = \left(1 - \frac{I_m R_s}{V_m}\right)\left[\frac{V_m + I_m R_s}{a V_T} - 1\right] \tag{C.33}$$

it is possible to invert the previous equation R_{sh} is obtained.

$$R_{sh} = \frac{\Phi}{-\frac{I_m}{V_m} + \frac{1}{a V_T}\left(1 - \frac{I_m R_s}{V_m}\right)\left(I_{pv} + I_0 - I_m\right)} \tag{C.34}$$

After substituting I_{pv} and I_0 with their expressions derived from the short-circuit and open-circuit conditions, and performing algebraic simplifications, the expression reduces to the compact form reported in Equation 3.70.

Reverse saturation current I_0

The saturation current I_0 can be derived by analysing the open-circuit condition ($V = V_{oc}$ and $I = 0$). Starting from Equation 3.66 the term -1 inside the exponential can be neglected since $\frac{V_{oc}}{aV_T}$ is typically large and therefore

$$\exp\left(\frac{V_{oc}}{aV_T}\right) - 1 \approx \exp\left(\frac{V_{oc}}{aV_T}\right).$$

The photocurrent I_{pv} can be expressed as a function of the short-circuit current using the relation

$$I_{pv} \approx I_{sc}\frac{R_{sh} + R_s}{R_{sh}},$$

Substituting these expressions into the previous equation yields

$$0 = \frac{R_{sh} + R_s}{R_{sh}} I_{sc} - I_0 \exp\left(\frac{V_{oc}}{aV_T}\right) - \frac{V_{oc}}{R_{sh}} \tag{C.35}$$

Rearranging the equation to isolate I_0 and multiplying both sides by R_{sh} gives

$$I_0 R_{sh} \exp\left(\frac{V_{oc}}{aV_T}\right) = (R_{sh} + R_s)I_{sc} - V_{oc} \tag{C.36}$$

Finally, dividing by the exponential term leads to the expression reported in Equation 3.71.

Photogenerated current I_{pv}

The photogenerated current represents the current produced by the photovoltaic effect. It can be obtained by analysing the short-circuit condition ($V = 0$ and $I = I_{sc}$). Substituting these conditions into the single-diode Equation 3.64 gives

$$I_{sc} = I_{pv} - I_0\left[\exp\left(\frac{I_{sc}R_s}{aV_T}\right) - 1\right] - \frac{I_{sc}R_s}{R_{sh}} \tag{C.37}$$

Under short-circuit conditions, the voltage across the diode ($I_{sc}R_s$) is very small. Therefore, the exponential term can be approximated as

$$\exp\left(\frac{I_{sc}R_s}{aV_T}\right) \approx 1$$

Consequently, the diode term becomes negligible since

$$I_0(1 - 1) \approx 0$$

The equation simplifies to

$$I_{sc} \approx I_{pv} - \frac{I_{sc}R_s}{R_{sh}} \tag{C.38}$$

Solving for I_{pv} yields

$$I_{pv} = I_{sc} + \frac{I_{sc}R_s}{R_{sh}} = I_{sc}\left(1 + \frac{R_s}{R_{sh}}\right) \tag{C.39}$$

Rearranging the expression leads to Equation 3.72.